ISSN en trámite

Geofísica Internacional

Revista Trimestral Publicada por el Instituto de Geofísica de la
Universidad Nacional Autónoma de México

México
Volume 55 Number 3
July - September
2016

— Geofísica Internacional —

Dr. Arturo Iglesias Mendoza
Director of Instituto de Geofísica

Dra. Xyoli Pérez Campos
President of Unión Geofísica Mexicana

Editor Chief
Dr. Servando De la Cruz-Reyna
Instituto de Geofísica, UNAM
sdelacrr@geofisica.unam.mx

Technical Editor
Mtra. Andrea Rostan Robledo
Instituto de Geofísica, UNAM
arostan@igeofisica.unam.mx

Editorial Board
Donald Bruce Dingwell
Earth and Environment
Ludwig Maximilian University of Munich, Germany

Eric Desmond Barton
Departamento de Oceanografía
Instituto de Investigaciones Marinas, Spain

Jorge Clavero
Amawta Consultores, Chile

Gerhardt Jentzsch
Institut für Geowissenschaften
Friedrich-Schiller-Universität Jena, Germany

Peter Malischewsky
Institut für Geowissenschaften
Friedrich-Schiller-Universität Jena, Germany

François Michaud
Géosciences Azur
Université Pierre et Marie Curie, France

Olga Borisovna Popovicheva
Scobeltzine Institute of Nuclear Physics
Moscow State University, Rusia

Jaime Pous
Facultad de Geología
Universidad de Barcelona, Spain

Joaquín Rui
UA Science
University of Arizona, United States

Angelos Vourlidas
Solar Physics Branch
NASA Goddard Space Flight Center, United States

Théophile Ndougsa Mbarga
Department of Physics
University of Yaounde I, Cameroon

Associate Editors
José Agustín García Reynoso
Atmospheric Science Centro de Ciencias de la Atmósfera UNAM, Mexico

Tereza Cavazos
Atmospheric Science
Departamento de Oceanografía Física CICESE, Mexico

Dante Jaime Morán-Zenteno
Geochemistry
Instituto de Geología, UNAM, Mexico

Margarita López
Geochemistry
Instituto de Geología UNAM, Mexico

Avto Gogichaisvilii
Geomagnetism And Paleomagnetism
Instituto de Geofísica UNAM, Mexico

Jaime Urrutia-Fucugauchi
Geomagnetism And Paleomagnetism
Instituto de Geofísica, UNAM, Mexico

Felipe I. Arreguín Cortés
Hydrology
Instituto Mexicano de Tecnología del Agua IMTA, Mexico

William Lee Bandy
Marine Geology And Geophysics
Instituto de Geofísica UNAM, Mexico

Fabian García-Nocetti
Mathematical And Computational Modeling
Instituto de Investigaciones en Matemáticas Aplicadas y en Sistemas UNAM, Mexico

Graciela Herrera-Zamarrón
Mathematical Modeling
Instituto de Geofísica, UNAM, Mexico

Ismael Herrera Revilla
Mathematical And Computational Modeling
Instituto de Geofísica UNAM, Mexico

Rene Chávez Segura
Near-Surface Geophysics
Instituto de Geofísica UNAM, Mexico

Juan García-Abdeslem
Near-Surface Geophysics
División de Ciencias de la Tierra CICESE, Mexico

Alec Torres-Freyermuth
Oceanography
Instituto de Ingeniería, UNAM, Mexico

Jorge Zavala Hidalgo
Oceanography
Centro de Ciencias de la Atmósfera UNAM, Mexico

Shri Krishna Singh
Seismology
Instituto de Geofísica, UNAM, Mexico

Xyoli Pérez-Campos
Seismology
Servicio Sismológico Nacional, UNAM, Mexico

Blanca Mendoza Ortega
Space Physics
Centro de Ciencias de la Atmósfera, UNAM, Mexico

Inez Staciarini Batista
Space Physics
Pesquisador Senior Instituto Nacional de Pesquisas Espaciais, Brazil

Roberto Carniel
Volcanology
Laboratorio di misure e trattamento dei segnali DPIA - Università di Udine, Italy

Miguel Moctezuma-Flores
Satellite Geophysics
Facultad de Ingeniería, UNAM, Mexico

Assistance
Elizabeth Morales Hernández,
Management
eliedit@igeofisica.unam.mx

GEOFÍSICA INTERNACIONAL, Año 55, Vol. 55, Núm. 3, julio - septiembre de 2016 es una publicación trimestral, editada por la Universidad Nacional Autónoma de México, Ciudad Universitaria, Alcaldía Coyoacán, C.P. 04150, Ciudad de México, a través del Instituto de Geofísica, Circuito de la Investigación Científica s/n, Ciudad Universitaria, Alcaldía Coyoacán, C.P. 04150, Ciudad de México, Tel. (55)56 22 41 15. URL: http://revistagi.geofisica.unam.mx, correo electrónico: revistagi@igeofisica.unam.mx. Editora responsable: Andrea Rostan Robledo. Certificado de Reserva de Derechos al uso Exclusivo del Título: 04-2022-081610251200-102, ISSN: en trámite, otorgados por el Instituto Nacional del Derecho de Autor (INDAUTOR). Responsable de la última actualización Saúl Armendáriz Sánchez, Editor Técnico. Fecha de la última modificación: 30 de junio 2016, Circuito de la Investigación Científica s/n, Ciudad Universitaria, Alcaldía Coyoacán, C.P. 04150, Ciudad de México.

El contenido de los artículos es responsabilidad de los autores y no refleja el punto de vista de los árbitros, del Editor o de la UNAM. Se autoriza la reproducción total o parcial de los textos siempre y cuando se cite la fuente completa y la dirección electrónica de la publicación.

Esta obra está bajo una Licencia Creative Commons Atribución-NoComercial-SinDerivadas 4.0 Internacional.

Geofísica
Internacional

Vol. 55, Núm. 3, julio-septiembre de 2016

Contents

Geofísica Internacional (2016) 55-3: 165-174

Original paper

Geoelectrical prospecting for a copper-sulfide mineralization in the Camaquã sedimentary basin, Southern Brazil

Ariane R. P. Côrtes*, César A. Moreira, Dimitri I. K. Veloso, Leandro B. Vieira and Flavio Anauate Bergonzoni

Received: March 20, 2015; accepted: May 09, 2015; published on line: July 01, 2016

DOI: 10.19155/rgi20165531608

Resumen

Este trabajo presenta los resultados de la aplicación del método de electroresistividad integrado con mapeo geológico de la superficie en un área potencialmente mineralizada con sulfuros de cobre, ubicada en el extremo norte de la cuenca sedimentaria del Camaquã, sudeste de Brasil. Esta mineralización se encuentra alojada en arenisca metamorfoseada, silicificada e intensamente fracturada, con abundante presencia de malaquita y azurita en los planos de fractura de la roca. El estudio geofísico consistió en 6 líneas de proyección de calicatas eléctricas en dispositivo Wenner-Schlumberger, con 520 m de largo y separación de 10 m entre electrodos dispuestos en una cuadrícula regular según criterio estructural previamente establecido. Los modelos de inversión muestran una región de baja resistividad en 60 m de profundad, que puede estar relacionada con una zona de sulfuros. Esta zona tiene forma aproximadamente circular, alargada en la dirección NW-SE y con 100 m de longitud. La zona de sulfuros se encuentra rodeada por zonas de alta resistividad relacionadas a zonas silicificadas. La evidencia de una zona arcillosa periférica al depósito es expresa por la abundante aparición de carbonato de cobre en la superficie, en conformidad con los minerales de arcilla y carbonatos que se originan a bajas temperaturas en etapas finales de cristalización en depósitos magmático-hidrotermales.

Palabras clave: cobre, sulfuros, mineralización, hidrotermal, resistividad eléctrica.

A. R. P. Côrtes*
D. I. K. Veloso
L. B. Vieira
F. Anauate Bergonzoni
Geosciences and Exact Sciences Institute
Univ. Estadual Paulista
Rio Claro, São Paulo State, Brazil.
**Corresponding author: ariane.rpc@gmail.com*

C. A. Moreira
Department of Applied Geology
Geosciences and Exact Sciences Institute
Univ. Estadual Paulista
Rio Claro, São Paulo State, Brazil

Abstract

In this paper are presented the results of the combination between a resistivity method and geological surface mapping, applied to the study of an area with potential mineralization of copper sulfides sited on the northern edge of the Camaquã sedimentary basin, Brazilian southern. The copper mineralization is housted in a metamorphosed, silicified and fractured sandstone with abundant presence of malachite and azurite in the fractured planes of the rock. The geophysical survey in this work consisted of 6 lines of electric resistivity tomography in Wenner-Schlumberger array, of 520 m long and 10 m of space between the electrodes, arranged in a regular grid according to structural criteria previously established. The inversion models show a low resistivity area in a depth of 60 m that can be related to a sulphidation zone. This zone with a somewhat circular shape is aligned in the NW-SE direction and is approximately 100 meters long. High resistivity areas around it indicate that it is surrounded by a silicification zones. The evidence for an argillic zone peripheral to the deposit is expressed by the occurrence of abundant copper carbonate in surface, since clay and carbonates are formed from low temperature and final stages of hydrothermal crystallization of the deposit.

Key words: copper, sulfide, mineralization, hydrothermal, electrical resistivity.

Introduction

The great abundance and diversity of mineral resources in Brazil has given the country an economic history linked to the mining activity. The increasing demand for commodities, present in both national and international markets, gives the country the role of major exporter of minerals on the world scenario. In this context, the recognition and incorporation of new reserves contribute in a great way to the growth of the economy of the country, since the export of minerals has high relevance to the maintenance of the positive trade balance (MME, 2011).

The great importance of copper in the world's economy has been maintained for decades due to physical and chemical properties, which gives it a wide range of uses in industrial technological development (Chatterjee, 2007). Since the discovery of large deposits is rare, the advances in research technology have led to a revaluation of areas previously declared to be of low economic potential.

Mineral prospecting studies are important for the discovery, qualification and quantification of new deposits not only at the beginning, but also during the ore exploration in order to expand reserves and increase the life span of the project. Mineral deposits are non-continuous and rare in the geological record, and their discovery requires long term research and large investments.

The traditional procedures used in the discovery and characterization of new mineral deposits comprise rock and soil sampling, chemical analysis and direct tools such as drilling, besides indirect tools such as geophysical methods (Moon *et al*., 2006).

Most of the known deposits in Brazil were discovered by geochemical prospecting and geological surface mapping, as the action of weathering agents in tropical environments enables the release and dispersal of most of the chemical elements associated with economic mineral accumulations (Licht, 1998).

However, the discovery of high tonnage and low volume deposits is becoming increasingly scarce through these series of procedures, besides of the grown of more distant discoveries from urban centers, which increases costs or even impairs the mining of eventually discovered deposits. Current and future prospects in mineral research should consider deeper deposits, so not susceptible to weathering action processes where conventional geochemical prospecting is ineffective (Moon *et al*., 2006; Marjoribanks, 2010).

This scenario favors the increasing use of geophysical methods as a fundamental tool in any project of prospecting and mineral exploration acting as a guide to sampling and analytical quantification by geochemistry in soil, rock and water samples. The geophysics also gains emphasis for being a non-invasive method, applicable to a wide variety of scales showing the possibility of obtain geological information at great depths, regardless of rock exposures and description of drill cores (Lowrie, 2007; Dentith & Mudge, 2014).

The prospect of sulfides by electrical geophysical methods – such as electrical resistivity and induced polarization (IP) – are highly promising due to the electrical resistivity and chargeability contrasts where deposits with disseminated or filonian sulfides and oxides are characterized by low resistivity and high polarizability (Irvine & Smith, 1990; Allis, 1990; Bakkali, 2006; Locke *et al*., 1999; Moreira *et al*., 2012; Vieira *et al*., 2016).

The various mineral occurrences located in Camaquã Basin, southern Brazil, have great potential for mining purposes for prospection of basic metals, besides a metallogenic and structural context favorable in face of various copper and gold mines described at a regional level. In this context, this work has the aim to develop the geophysical study in detail of a copper occurrence on the northern edge of Camaquã Basin, where the Electrical Resistivity Tomography (ERT) technique was applied.

Area location and history

The area of study is located northwest of Caçapava do Sul city in Rio Grande do Sul (RS), 240 kilometers from Porto Alegre, the state capital. It can be reached through the BR-290 highway, and 1.5 kilometers after the intersection with BR-392 highway, through a dirt road which can be accessed from the Cerrito do Ouro village (Figure 1).

The region has a long history related to mining activity of copper and gold. The interest in the region was sparkled in the late nineteenth century, and it has been occupied ever since through the drive of mining. The presence of copper associated with gold and silver attracted several companies which built facilities aiming to explore these minerals at a viable cost over the last century (Ronchi & Lobato, 2000).

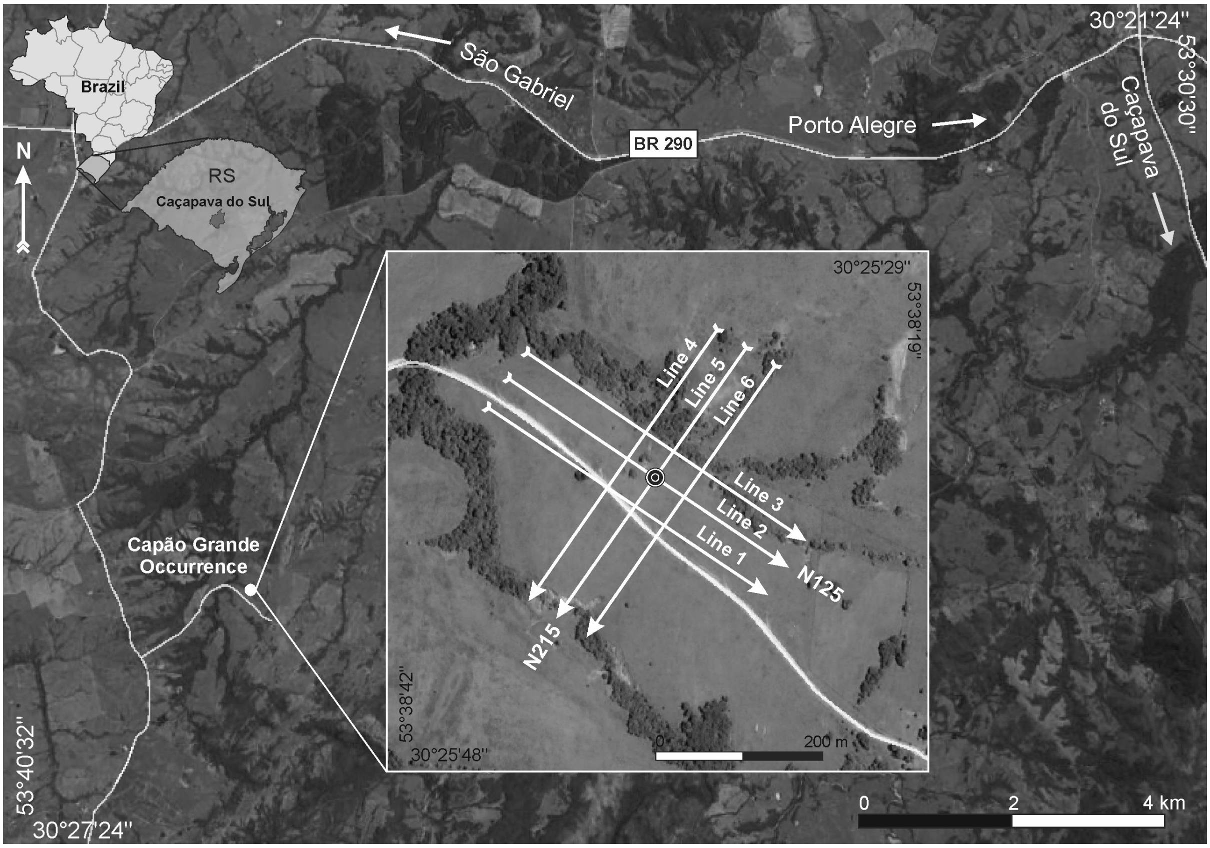

Figure 1. Location of the study area, with detail to the arrangement of lines of purchase.

After more than 100 years, mining activities were interrupted due to the low prices of metal commodities in the international market. The long term exploration also led to the exhaustion of the reserves around the year 1992. Currently, the mining activity in the city is restricted to limestone mining.

The study area consists in a cupriferous occurrence named Capão Grande, recognized by geochemical studies in stream sediments in research campaigns carried out by the National Department of Mineral Production (DNPM) in 1965. At first, the occurrence was considered by Bocchi (1970) as of no economic interest for mining due to small volume and ore content. However, the author highlighted the importance of conducting a detailed research in the region thanks to the favorable geological conditioning, porosity and fracturing.

Geology

The study area on the northern edge of the Camaquã Basin is seated on igneous and metamorphic terrains inside the Sul Riograndense Shield. The Camaquã Basin is a tectonic depression generated and developed during the final stages of evolution of the Dom Feliciano Belt, associated to a system of tardi- to post-orogenic basins related to the end spasms of Brasiliana/Pan-Africana Orogeny (Neto *et al*., 2004).

The Camaquã Basin has an elongated shape of N30E general direction, about 100 km long and up to 100 km wide (Neto *et al*., 2004) that can be understood as the record of the superposition of different types of basins, tectonically, geochronologically and thermodynamically individualized, with its own geological characteristics and distinct mechanisms of subsidence (Holz & De Ros, 2000). The Basin has been treated in terms of subsidence and filling pulses interrupted by deformation events, uplift and erosion, what generates a complex pattern of filling (Kazmierczak, 2006).

The type of filling of the Camaquã Basin was alternated between volcanic activity - represented by lavas and pyroclastic and epiclastic deposits - and siliciclastic deposition, which together with the tectonic, generated a filling where more deformed units are superimposed by less and less deformed units (Holz & De Ros, 2000). The record of sedimentary and igneous rocks present in the Basin comprise a time interval of 450-620 Ma and are devoid of significant features of regional metamorphism (Borba, 2006).

The study area is located near the contact with metamorphic basement, represented by volcanoclastic, epiclastic, and chemical rocks of the Campestre Sequence of the Vacacaí Metamorphic Complex. In the region there are also outcrops of rocks which belong to Maricá Group and the Acampamento Velho Formation, held in Cerro do Bugio Group (Figure 2).

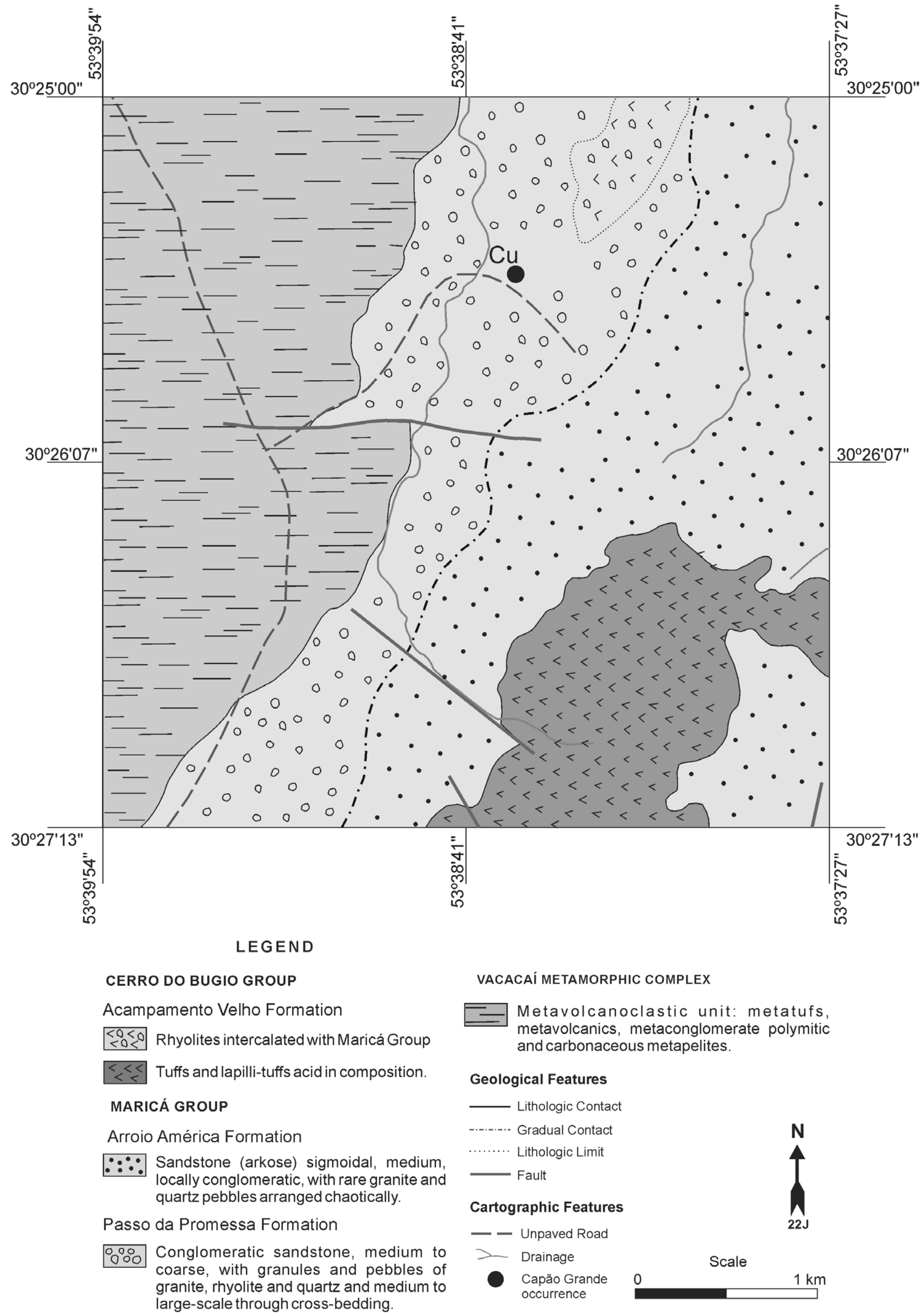

Figure 2. Geological map of the study area (Adapted from Porcher, 1995).

The Capão Grande copper occurrence is hosted in a lithotype included in the Passo da Promessa Formation, basal unit of Maricá Group. It occurs in a single outcrop in northeast direction in an extensive area of field, approximately 10 meters long by one to two thick.

The host rock is represented by intensely silicified metarenites, medium-grained, reddish-brown, apparently without preserved sedimentary structures and highly fractured. The indications of mineralization are expressed by the abundant presence of malachite and azurite, both supergene copper minerals that occurs in the interstices of the rock weakness planes (layering or fractures) or as disseminations in the pores of the rock.

Materials and methods

In this work, the DC resistivity method was employed by electrical resistivity tomography technique (ERT) in Wenner-Schlumberger array. The geophysical data was acquired through six lines with 520 m long and 10 m spacing between non-polarizable porous-pot electrodes that allow the percolation of $CuSO_4$ supersaturated solution in the ground. This configuration aims to reduce the contact resistance and nullify the parasitic currents generated by the use of metallic electrodes.

The Wenner-Schlumberger array is a hybrid arrangement that combines the Wenner and Schlumberger arrangements. It considers a set of electrodes with the same constant spacing, in contrast with the classical Schlumberger array used for vertical electrical soundings (Loke, 2000; Milson & Erikssen, 2011).

The lines were arranged in a regular grid, according to the structural criteria established in previous works which consider the crossing of major regional structures (Ilha, 2010; Silva, 2010). In this way, lines 1, 2 and 3 were distributed in the direction N125 and lines 4, 5 and 6 were arranged in the direction N215, all spaced 40 m from each other. The topographical data was acquired with a Differential Global Positioning System (DGPS) with Trimble software that allows the use of the Geographic Information System (SIG) existent.

The equipment used for the acquisition of resistivity measurements was the Terrameter LS, manufactured by ABEM Instrument (Sweden). This equipment consists of a single module for transmitting and receiving of automated signals from previous programming, with 250W, resolution of 1 μV and maximum current of 2.5 A (ABEM, 2012).

The field measurements were initially processed by the software Res2Dinv, where bidimensional resistivity models for the subsurface were generated from the smoothness-constraint least squares inversion considering the topography adjustment (Geotomo Software, 2003).

The implementation of the smoothness-constraint least squares inversion in the Res2Dinv software is based on the division of the subsurface into rectangular blocks, with the resistivity values adjusted to fit the field measurements (Degroot-Hedlin & Constable, 1990; Loke & Baker, 1996). This optimization focus on reducing the difference among the apparent resistivity values calculated and the ones measured in field, by the resistivity adjustment of the block models, which difference is expressed by the RMS (Root Mean Square) error and, simultaneously, aims to minimize the model roughness (smoothness constraint) (Loke & Baker, 1996). In this work, the robust constraint algorithm was used in the data processing.

The numeric product of bidimensional inversion of the data from each section was used to generate 3D visualization models in the Oasis Montaj platform, where the 2D data obtained in Res2Dinv program were modeled from the minimum curvature algorithm for smoothing the core values in relation with the limits of the investigated area. The range of 8 Ω.m and 300 Ω.m values were modeled as a 3D surface in an attempt to evaluate the shapes of the low and high resistivity zones, respectively.

This process is part of a routine of basic steps adopted in mineral research. In this case, the sampling plan is frequently defined from statistical, structural, spatial placement criteria, among others (Moon *et al*., 2006). A simple procedure is sampling by a set of holes perpendicular to the main axis of the structure, followed by a parallel set of hollowing lines.

The resolution of the sampling net is conditioned to the space between holes, their lines and among quantities of samples collected by holes. Nevertheless, the analytical result of the samples is sampled and modeled in bidimensional terms and later interpolated in tri-dimensional terms. Each point of the final 3D model is transformed in a block with dimensions conditioned to statistical criteria and sampling net, to which content based in chemical analysis and a mean value of density related to the rock that hosts the mineral is attributed. The relationship between content and volume enables the calculation of reserves and the economic feasibility of the enterprise (Moon *et al*., 2006).

Geophysical 3D visualization models derived from 2D sections provide a very wide comprehension on the complexity of geological structures and models of mineral deposits (Kemp, 2000; Zanchi *et al*., 2009; Aizebeokhai *et al*., 2011; Akiska *et al*., 2012).

Results and discussion

The sections are presented in terms of distance *versus* depth, with a logarithmic color scale. The processed resistivity data show a range of variation with values between 6 Ω.m and 590 Ω.m, where warm colors represent high resistivity values and cold colors represent low resistivity values. In general, the sections exhibit a predominance of high values in the shallow and intermediate portions, and low values at higher depths (Figure 3).

Over-all, all resistivity inversion models present, with high or low presence, a high-resistivity zone in the center of the section between 170 m to 380 m along the line. This range of high values outlines most of the horizontally elongated elliptical zones sections with values above 305 Ω.m. Another feature well seen in all sections is the change from high to low resistivity values around 30 m depth. The lower values culminate in a significant area with values below 20 Ω.m located in the center of the sections and below 50 m depth. The maximum depth of the inverted models was 80 m, but apparently the low resistivity zone exceeds it.

Besides the central zone with high resistivity values, there are others with minor proportion which are present in all sections reaching values greater than 590 Ω.m. Around 160 m along the line, it is observed a small resistive zone at about 70 m deep, which culminates with a significant vertical zone with resistivity values above 305 Ω.m in section 5. Another highly resistive zone represented in all sections is located between the distances 430 m to 490 m with resistivity values greater than 590 Ω.m. These zones are distributed in the vicinity of the low resistivity zone located 60 m deep.

Next to the surface and center sections (more precisely where the outcropping mineral occurrence is located), there is a predominance of intervals with average resistivity ranges that reach values up to 305 Ω.m. It is important to note that the mineral occurrence is described in highly silicified meta-sandstones, different from the other outcrops described in the region where the rock presents certain crispness and preserved primary structures, as such as cross-bedding.

Therefore, the analysis of the resistivity inversion models enables the recognition of two main zones: resistive zones, characterized by values greater than 300 Ω.m and a conductive zone (or low resistivity), characterized by values below 20 Ω.m located in depth in the center of the sections.

The cementation of the host rock by quartz and carbonates observed in the surface results in a decrease of porosity which leads to higher resistivity values. Therefore, areas with moderate to high resistivity are probably an indicative of silicification to be found on the top and side portions of the low resistivity region (Figure 4).

The top resistive zone - or area above the sulfide zone - is represented by intense silicified rock outcrop, cut by subvertical veins of copper carbonate. Although absent in surface, it is likely to find sulphidation in disseminated or venular forms in higher abundance as the depth increases.

The area with low resistivity values on the other hand points to the occurrence of highly conductive materials. Electronic conduction in metallic minerals (free movement of electrons) reduces the resistivity of metal-bearing rocks. Particularly at high ore concentrations the bulk resistivity decreases significantly. This feature confirms the existence of a zone enriched in metal ore minerals, probably represented by copper sulfide minerals, as such as chalcopyrite, calcosite and bornite (Figure 4).

Accordingly, the conductive area present at 60 meters deep represents a possible area of sulphidation with elongated form in the NW-SE direction, surrounded by the silicification zones.

The copper carbonates observed on mineral outcrop are indicative of an occurrence related to final stages of crystallization generally present in the peripheral portions of the mineral deposit. For this reason, their content gradually decreases at greater depths. Metal sulfides, in turn, tend to have higher levels towards the sulphidation zone.

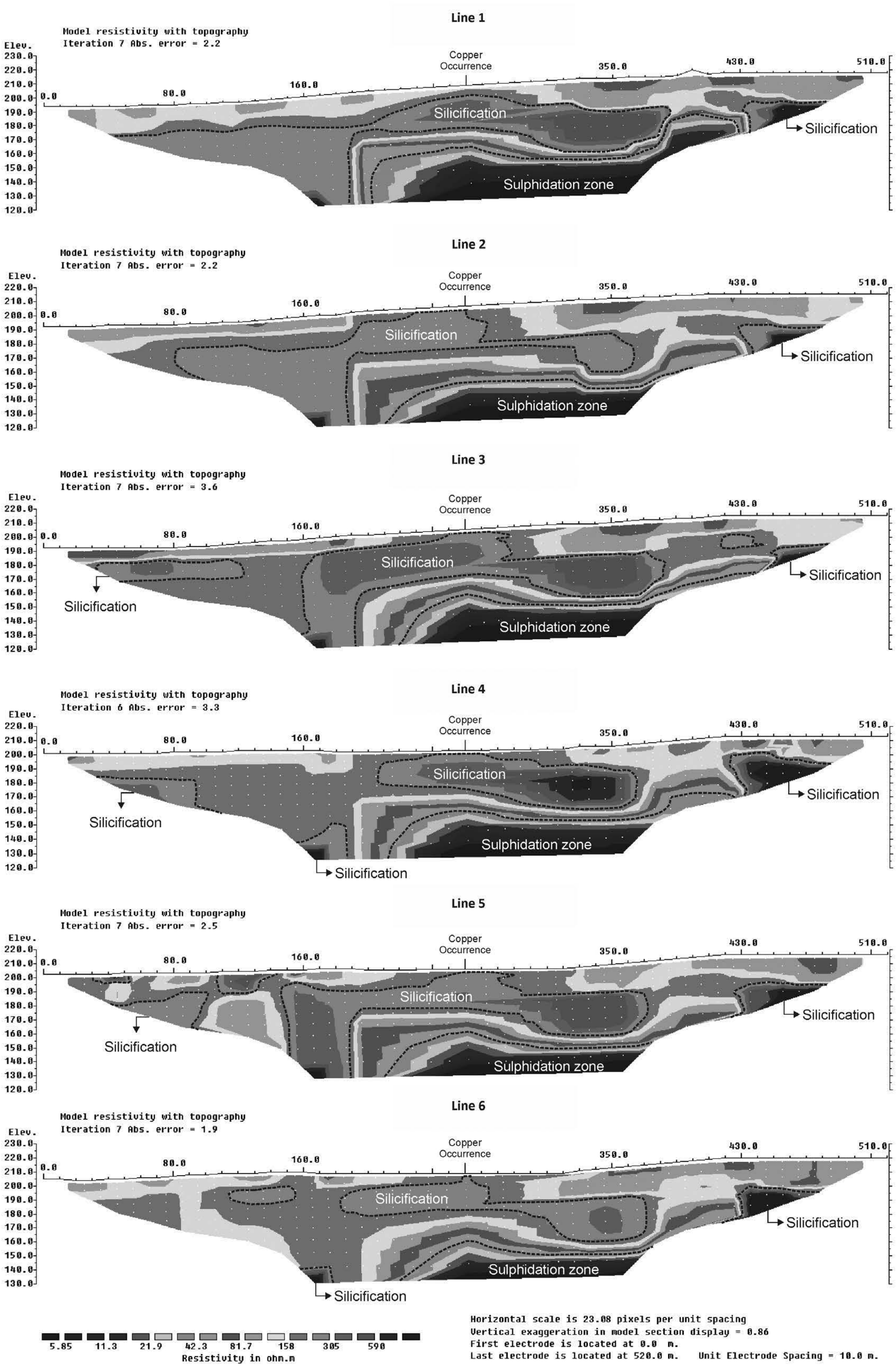

Figure 3. Inversion models for resistivity.

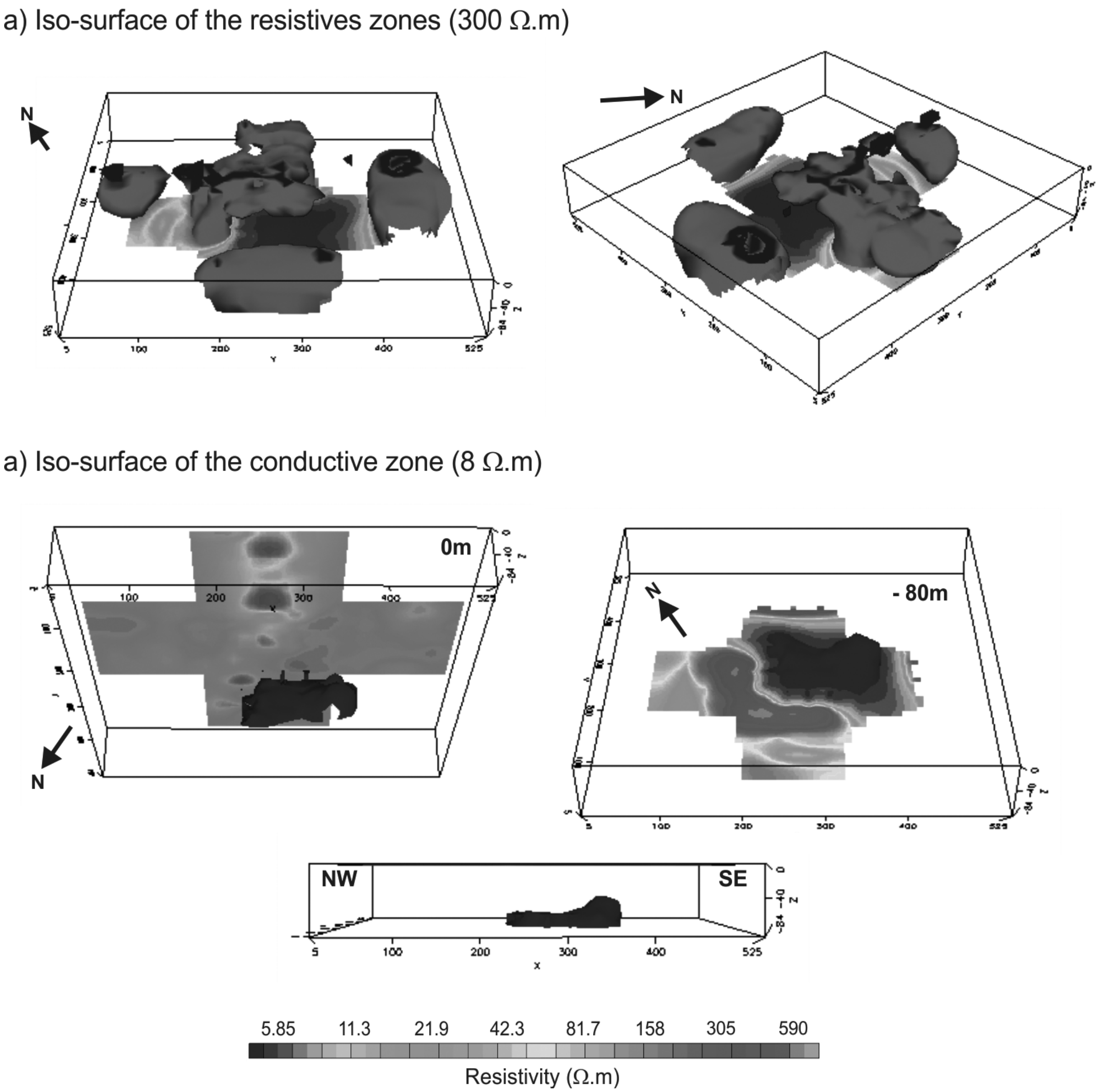

Figure 4. a) 3D visualization models with design of high resistivity zones (silicification, in red) and b) low resistivity zones (probable mineralization, in blue).

Conclusions

The results obtained by the resistivity method, combined with geological data and field recognition, were satisfactory to characterize the cupriferous occurrence and in delineation of a promising target for direct prospecting campaigns through drilling surveys.

Based on the field recognition, it was possible to identify evidences of mineralization represented by copper carbonates (malachite and azurite), which occurs in form of silicified and impregnations in fractured metarenite. Such elements are associated with peripheral portions of hydrothermal sulfide deposits and therefore indicators of possible presence of sulfides in depth.

The combined analysis between 2D and 3D resistivity models allowed the recognition of a possible mineralized body in depth and zones of marginal silicification, characterized by low and high resistivity values, respectively.

The sulphidation zone, possibly with the highest levels of ore in the area, is characterized by an elongate body of approximately 100 m in the NW-SE direction. It was not possible to establish the maximum depth of the mineralized body, as apparently there is continuity below 80 m (maximum depth of the inverted models). Therefore, the limited investigation depth only allowed the detection of the upper limit of the sulphidation zone. Besides that, the limits of this zone to the south were not mapped due to the limited coverage of the survey.

The silicification zones are surrounding the main ore body and are characterized by the predominance of silica, which occurs as cement of pores of the adjacent rock. Present from shallower portions to greater depths, this area may be subdivided into two major zones: top silicification zone (or above sulfide zone) described in mineral outcropping occurrence, and lateral silicification zones.

Evidence of an argillic peripheral zone of the deposit are expressed by abundant occurrence of copper carbonates on the surface. Clay and carbonates are formed in low temperatures in the final stages of crystallization from hydrothermal deposits. The absence of a significant argillic zone may be an indicative of the low content of clay minerals in the metarenite.

A second phase of the geoelectrical study could focus on the acquisition of longer lines for increased depth investigation and greater coverage of the southern part, as means to improve the estimation of the total ore body volume.

The features recognized in the field, along with the identified architectural elements of the deposit with the aid of geophysics, corroborate with the hydrothermal-magmatic model, especially for types such as copper-porphyry and low-sulphidation epithermal, previously described in other mineralization of Cu (Au) distributed throughout Camaquã Basin. However, for better interpretations regarding the storage model, further studies are required on surface geochemistry and also direct analysis by means of drilling and sampling.

Acknowledgments

The authors are thankful to National Council for Scientific and Technological Development - CNPq, for the financial support whereby process number 470821/2013 (Edital Universal – 2013).

References

ABEM, 2012, Terrameter LS - Instruction Manual, 122pp.

Allis R.G., 1990, Geophysical anomalies over epithermal systems. *Journal of Geochemical Exploration*, 36, 339-374.

Aizebeokhai A.P., Olayinka A.I., Singh V.S., Uhuegbu C.C., 2011, Effectiveness of 3D geoelectrical resistivity imaging using parallel 2D profiles. *International Journal of the Physical Sciences*, 6, 5623-5647.

Akiska S., Sayili I.S., Demirela G., 2013, Three-dimensional subsurface modeling of mineralization: a case study from the Handeresi (Çanakkale, NW Turkey) Pb-Zn-Cu deposit. *Turkish Journal of Earth Sciences*, 22, 574-587.

Bakkali S., 2006, A resistivity survey of phosphate deposits containing hardpan pockets in Oulad Abdoun, Morocco. *Geofísica Internacional*, 45, 1, 73-82.

Bocchi P.R., 1970, Geologia da Folha de Caçapava do Sul, Rio Grande do Sul. Boletim 245, DNPM, Rio de Janeiro, 96pp.

Borba A.W., 2006, Evolução geológica da "Bacia do Camaquã" (Neoproterozóico e Paleozóico Inferior do Escudo Sul-rio-grandense, RS, Brasil): uma visão com base na integração de ferramentas de estratigrafia, petrografia e geologia isotópica. Doctoral Thesis, Universidade Federal do Rio Grande do Sul, Porto Alegre.

Chatterjee K.K., 2007, Uses of Metals and Metallic Minerals. *New Age International Publishers*, New Delhi, 333pp.

Degroot-Hedlin C., Constable S., 1990, Occam's inversion to generate smooth, two-dimensional models from magnetotelluric data. *Geophysics*, 55, 1613- 1624.

Dentith M., Mudge S.T., 2014, Geophysics for the mineral exploration geoscientist. Cambridge University Press, Cambridge, 516pp.

Geotomo Software, 2003, RES2DINV, version 3.53, Rapid 2D resistivity & IP inversion using the least-square method - Geoelectrical Imaging 2-D & 3D, Geotomo Software, Penang, Malaysia, 129pp.

Holz M., De Ros L.F., 2000, Geologia do Rio Grande do Sul. Edição CIGO/UFRGS, Porto Alegre, 444pp.

IBGE - Instituto Brasileiro de Geografia e Estatística, 2014. Cidades – Caçapava do Sul. Avaliable in: <http://cidades.ibge.gov.br/xtras/perfil.php?lang=&codmun=430280>. Access in: 10/12/2014.

Ilha M.L., 2010, Caracterização geofísica e estrutural da ocorrência cuprífera Capão Grande. Graduation work, Universidade Federal do Pampa, Caçapava do Sul.

Irvine R.J., Smith M.J., 1990, Geophysical exploration for epithermal gold deposits. *Journal of Geochemical Exploration*, 36, 375-412.

Kazmierczak T.S., 2006, Mapeamento da bacia do Camaquã com a utilização de dados geofísicos, geologia e sensoriamento remoto. Master of Science Dissertation, Universidade Federal do Rio Grande do Sul, Porto Alegre.

Kemp E.A., 2000, 3-D visualization of structural field data: examples from the Archean Caopatina Formation, Abitibi greenstone belt, Quénec, Canadá. *Computers & Geosciences*, 26, 5, 509-530.

Licht O.A.B., 1998, Prospecção Geoquímica: Princípios, Técnicas e Métodos. Serviço Geológico do Brasil, Rio de Janeiro, 148pp.

Locke C.A., Johnson S.A., Cassidy J., Mauk J.L., 1999, Geophysical exploration of the Puhipuhi epithermal area, Northland, New Zealand. *Journal of Geochemical Exploration*, 65, 91-109.

Loke M.H., 2000, Electrical imaging surveys for environmental and engineering studies: a practical guide to 2-D and 3-D surveys. Report Geotomo LLC, Penang, Malaysia. 67pp.

Loke M.H., Baker R.D., 1996, Rapid least-squares inversion of apparent resistivity pseudosections by quasi-Newton method. *Geophysical Prospecting*, 44, 131-152.

Lowrie W., 2007, Fundamentals of Geophysics. Cambridge University Press, New York, 393pp.

Marjoribanks R., 2010, Geological methods in mineral exploration and mining. 2°ed., Springer, Heidelberger, 248pp.

Milson J., Erikssen A., 2011, Field Geophysics. John Wiley and Sons, Chichester, 297pp.

MME - Ministério das Minas e Energia, 2011, Plano Nacional de Mineração 2030-Geologia, Mineração e Transformação Mineral. Brasília: MME, 180pp.

Moreira C.A., Borges M.R., Vieira G.M.L., 2012, Malagutti Filho W., Montanheiro M.A.F., Geological and geophysical data integration for delimitation of mineralized areas in a supergene manganese deposits. *Geofísica Internacional*, 53, 2, 201-212.

Moon C.J., Whateley M.E.G., Evans A.M., 2006, Introduction to Mineral Exploration**.** Backwell Publishing, Oxford, 499pp.

Neto V.M., Bartorelli A., Carneiro C.D., Brito-Neves B.B., 2004, Geologia do Continente Sul-Americano: Evolução da Obra de Fernando Flávio Marques de Almeida. Editora Beca, São Paulo, 673pp.

Porcher C.A., 1995, Folha Passo do Salsinho Folha SH. 22-Y-A-I-4 Estado do Rio Grande do Sul (1:50.000) - Programa Levantamentos Geológicos Básicos do Brasil, CPRM, Brasília, 358pp.

Ronchi L.H., Lobato A.O.C., 2000, Minas do Camaquã: um estudo multidisciplinar. Editora Unisinos, *São Leopoldo*, 366pp.

Silva F.G., 2010, Aquisição magnetométrica na caracterização de feições geológicas e estruturais da ocorrência de cobre de Capão Grande, município de Caçapava do Sul, RS. Graduation work, Universidade Federal do Pampa, Caçapava do Sul.

Vieira L.B., Moreira C.A., Côrtes, A.R.P., Luvizotto, G.L., 2016, Geophysical modeling of the manganese deposit for Induced Polarization method in Itapira (Brazil). *Geofísica Internacional*, 55, 2, 107-117.

Zanchi A., Salvi F., Zanchetta S., Sterlacchini S., Guerra, G., 2009, 3D reconstruction of complex geological bodies: Examples from the Alps. Computers & Geosciences, 35, 1, 49-69.

Original paper

The level variability, thermal structure and currents in Lake Chapala, Mexico

David Ávalos-Cueva, Anatoliy Filonov*, Iryna Tereshchenko, César Monzón, Diego Pantoja-González and Federico Velázquez-Muñoz

Received: June 06, 2015; accepted: March 07, 2016; published on line: July 01, 2016

DOI: 10.19155/rgi20165531610

Resumen

En este estudio se analizan y discuten mediciones instrumentales de temperatura, corrientes y nivel del lago realizadas en 2005-2014. Mediciones continuas de las fluctuaciones de temperatura y nivel en la parte norte del lago mostraron la presencia de oscilaciones tipo seiches de primer y segundo modo, con períodos de 5.7 y 2.8 horas, y amplitudes de 15.4 y 2.1 mm. En 2006 se realizaron cuatro muestreos de temperatura. Las mediciones mostraron una diferencia de temperatura entre la costa norte y sur de 2-3 °C, en las cuatro estaciones del año. Realizamos modelación de las corrientes en el lago con la ayuda del modelo hidrodinámico bidimensional HAMSOM para las estaciones húmeda y de estiaje. Los resultados de las simulaciones se ajustan con las mediciones de ADCP. Se encontró que en ambas épocas, en la parte central del lago está presente un giro anticiclónico con diámetro de 10 a 12 km. Las mediciones realizadas en el verano de 2014 confirmaron la presencia de este giro, y mostraron una fuerte influencia en la distribución espacial de la temperatura en el lago.

Palabras clave: Lago de Chapala, variabilidad de nivel, estratificación, corrientes.

Abstract

Measurements of temperature, currents and lake level taken in 2005-2014 are analyzed and discussed. Moored measurements of temperature and level in the northern part of the lake reveal the presence of seiches oscillations of the first and second modes, with periods of 5.7 and 2.8 hours, and amplitudes of 15.4 and 2.1 mm. In 2006 four temperature cross-sections were carried out in the study area. The obtained data reveal that in all four seasons of the year the temperatures averaged over the north and south coastal areas differ by 2-3°C. The lake currents were simulated using the HAMSOM 2-D hydrodynamic model both for wet and dry seasons. The model results are in good agreement with the ADCP data. The presence of an anticyclonic gyre, 10-12 km in diameter, in the central part of the lake in both seasons is revealed. In particular, the summer 2014 data provide evidence of the gyre and its impact on the spatial distribution of temperature in the lake.

Key words: Lake Chapala, level variability, stratification, current measurements, modeling

A. Filonov*
I. Tereshchenko
C. Monzón
D. Pantoja-González
F. Velázquez-Muñoz
Departamento de Física
Universidad de Guadalajara
Blvd. Marcelino García Barragán 1421
C.P. 44430, Guadalajara, Jalisco
**Corresponding author: afilonov@prodigy.net.mx*

D. Ávalos-Cueva
Posgrado de Ciencias del Mar y Limnología
Universidad Nacional Autónoma de México
Ciudad Universitaria,
Delegación Coyoacán, 04510
México D.F., México.

Instituto Tecnológico Superior de Arandas
Apdo. Postal 4-7180
Arandas, Jal., México

Introduction

Lake Chapala is the Mexico largest lake and the third largest in Latin America. It is located at approximately 20ºN; 103°W, 1542 m above sea level. It measures 75 x 25 km, and has an average depth of 6 m and a maximum depth close to 11 m (Figure 1). The lake's tributaries and effluent systems are the Lerma and Santiago rivers. There is a mountain ridge along its southern and northern shores. The Lerma-Chapala watershed system has a surface area of approximately 47000 km^2 (Sandoval, 1994; Aparicio, 2001). The average precipitation in this area is about 750 mm per year, which drops to 300 mm in drought years and reaches 1200 mm in wet years. The annual surface evaporation is about 1400-1600 mm, which exceeds the average precipitation by a factor of 2 (Jaurégui*,* 1995; Filonov *et al.,* 1998).

The deficit is balanced by the influx of water from the Lerma River and runoff from its basin (Mosino and Garcia, 1974; Jáuregui, 1995; Filonov and Tereshchenko, 1997). In the years of drought the annual precipitation decreases to 500 mm and there is no outflow from the lake into the Santiago river (Riehl, 1979). However, in wet years when the annual precipitation reaches 1000 mm, the river has outflow.

Local winds and breezes play a crucial role in the lake's dynamics. They develop daily, as a result of the large temperature difference between the lake's surface and the surrounding land covered with scarce vegetation. Consequently, the land becomes quickly heated and cooled during the day and night. Daytime breeze is stronger than the night time breeze and heading towards the land. During the daytime, the lake breeze speed reaches 8-10 m/s, whereby the evaporation from the lake's surface is of greater intensity than at night time (Filonov, 1998; Filonov *et al.,* 2001).

The lake plays an essential role in the economy of Mexico. During the past decades, the lake became polluted with anthropogenic agents, which enter into the lake from the Lerma River and adjacent areas (Hansen, 1994; Hansen and Manfred van Afferden, 2001; Jay and Ford, 2001). The pollution results in the rapid growth of water lilies and Typha latifolia. Furthermore, the lake level has dropped because of the irrigation and domestic needs of cities. All this reduces its attractiveness as a recreational and tourist area, therefore, the Mexican government has taken measures to protect the dam and the lake from the negative consequences of anthropogenic actions (Filonov *et al.,* 1998).

In the last two decades, researchers from the Department of Physics of the University of Guadalajara began to study the thermodynamic processes in the Lake Chapala using hydrodynamic modeling and the analysis of data collected with the use of

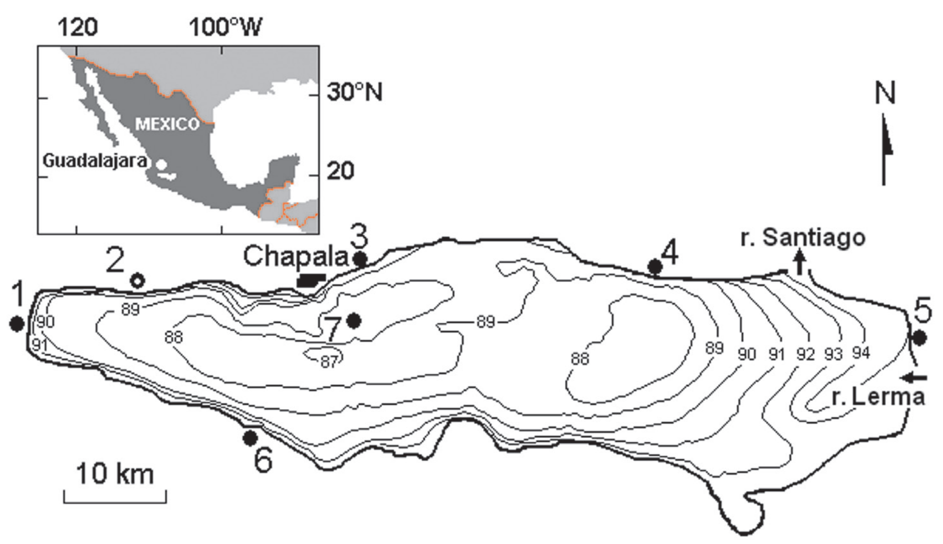

Figure 1. Bathymetric map of Lake Chapala. Depth is given in meters in relation to the 87 m isobaths. Arabic numerals sites meteorological stations are shown: 1- Jocotepec, 2 - Atequiza, 3 - Chapala, 4 - Poncitlán, 5 - Jamay, 6 - Tizapán and 7- Isla de Alacranes.

up-to-date oceanographic and meteorological measurement devices. In this paper, we discuss the analysis of wind data collected over the lake, as well as the fluctuations in water temperature, currents and lake level. The main purpose of this study is to gain more understanding of the thermal and dynamic patterns of the Lake Chapala during the dry and wet seasons.

Materials and methods

One major impediment in the data collection across the study area is a great number of fishing nets deployed in the Lake Chapala. Hundreds of people are engaged in the fishing industry, which is a major source of income for them. Therefore, working there, we always rely on good luck, but do not always succeed. On some occasions, partial losses of the instruments and equipment were inevitable.

This study is based on the analysis of the temperature, currents and lake level data collected in 2005-2014 using the following oceanographic instruments: CTD SBE19-plus, SBE-39, SBE-26, HOBO V2 and a 600 kHz RDI ADCP. During that time period the measurements were not taken regularly as they pursued different goals. The sampling strategies varied with the experiment (we used different sets of instruments) and will be described in the corresponding sections.

Most measurements were taken in the deeper northern part of the lake. The meteorological data were collected from the network of seven automatic meteorological stations deployed around the lake and in its centre. The spatial structure of the temperature field and currents for the dry and wet seasons was sampled by towed temperature recorders arranged in the antenna pattern and ADCP.

Computational model

To calculate horizontal currents from wind circulation over the lake, we used the Hamburg Shelf Ocean Model (HAMSOM); a two-dimensional, non-linear, semi-implicit numerical shelf model (Backhaus, 1983). The model employs the following equations of motion:

$$\frac{\partial U}{\partial t}+\frac{U}{(H+\zeta)}\frac{\partial U}{\partial x}+\frac{V}{(H+\zeta)}\frac{\partial U}{\partial y}-fV$$

$$=-g(H+\zeta)\frac{\partial \zeta}{\partial x}+A_H\nabla_h^2 U+\tau_{(s)}^{(x)}-\tau_{(b)}^{(x)}, \tag{1}$$

$$\frac{\partial V}{\partial t}+\frac{U}{(H+\zeta)}\frac{\partial V}{\partial x}+\frac{V}{(H+\zeta)}\frac{\partial V}{\partial y}+fU$$

$$=-g(H+\zeta)\frac{\partial \zeta}{\partial y}+A_H\nabla_h^2 V+\tau_{(s)}^{(y)}-\tau_{(b)}^{(y)}, \tag{2}$$

$$\frac{\partial \zeta}{\partial t}+\frac{\partial U}{\partial x}+\frac{\partial V}{\partial y}=0 \tag{3}$$

Here *U* and *V* are zonal and southerly transports, respectively; $f = 2\Omega\sin\varphi$ is the Coriolis parameter $\Omega = 0.04178$; cycles/h is the angular velocity of the Earth; φ is latitude; ζ is the lake level elevation; *t* is time; *H* is water depth; A_H is the horizontal eddy viscosity coefficient; ∇_h^2 is the horizontal Laplace operator; *g* is acceleration due to gravity; τ_S is wind stress; and τ_b is bottom friction stress. The model was previously applied to the Gulf of California, Carbajal, 1993; Marinone, 2003; the Santa María del Oro Volcanic Lake, Serrano *et al.,* 2002 and Lake Alchichica, Filonov *et al.,* 2006).

Results

Lake level and temperature variations at a single point

Previous studies have shown that the main processes that exert primary control over climatic conditions and water circulation in the Lake Chapala are the local winds and lake breezes (Filonov *et al*., 1998). The main power source of the lake breeze circulation is the diurnal temperature cycle caused by the daily variations of (a) incoming solar radiation and (b) heating of the underlying surface and to atmosphere. The interaction between the land, lake and atmosphere is a very complex system with many feedbacks. The area around the Lake Chapala is mountainous, with valleys of various spatial orientations. The thermal energy pulsates with daily periodicity but does not remain at a fixed frequency. It is redistributed at different frequencies in a complex way in the form of fluctuations (Scorer, 1978).

The lake level and temperature data in our experiment were sampled every 5 minutes by a SBE-26 temperature-depth recorder (the accuracy is 0.002 °C for temperature and 1 mm for depth), which was deployed on the mooring in the northern part of the lake, at the water depth of 2 m. The measurements were taken from 20 April to 12 September 2005

(153 days). Figure 2a shows that the seasonal level fluctuations in 2005 strongly depend on the evaporation and precipitation over the lake and its watershed. In April and May, the level dropped at a rate of about 30 cm / month, and then, until the middle of September it raised more rapidly, about 50 cm / month. In July, the level remained almost unchanged because of the reduced rainfall during this time of the year, which usually occurs over the territory of Central Mexico and is called "canicula".

The SBE-26 time series also shows that the daily fluctuations of lake level are determined by diurnal and semidiurnal harmonics. At a single point, the level fluctuations occur at times of the amplification and easing of the breeze whose speed was measured at the weather station Chapala (Filonov, 2002). The breeze forcing is the main source of energy for all kinds of motion in the lake. With a well-defined diurnal cycle, this breeze varies from virtually a calm at night and morning to steady northerly winds up to 6 m/s (gusting up to 10-12 m/s) in the afternoon. Since breeze circulation occurs over the entire lake throughout the year, it is expected to play an important role in the mechanisms of vertical and horizontal mixing within the lake.

The analysis shows that the start of wind intensification lags the time of the downturn of the lake level by less than two hours. The rise and drop of the level are asymmetrical. The trough lasts longer than the peak which is apparently caused by the asymmetric impact of the wind on the water surface.

As seen from the data (Figure 2b), the amplitude of the daily temperature fluctuations at the mooring site are 2-3 °C at the 2-m level and decrease to 1-1.5 °C as the instrument depth increases due to the higher lake level during the summer months.

Figure 2c shows the average spectra computed from the time series of lake level and temperature variations. The level spectrum reveals the presence of free seiche waves with 5.7 and 2.8-hour periods in the lake. Their mean square amplitudes are 15.4 and 8.1 mm, respectively. The lake is shaped like an ellipse whose axes vary in size, therefore the oscillations with a period of 5.7 hours likely correspond to the seiches propagating along the greater axis of the ellipse (west-east). The other oscillation mode is related to the seiches propagating along its smaller axis (north-south).

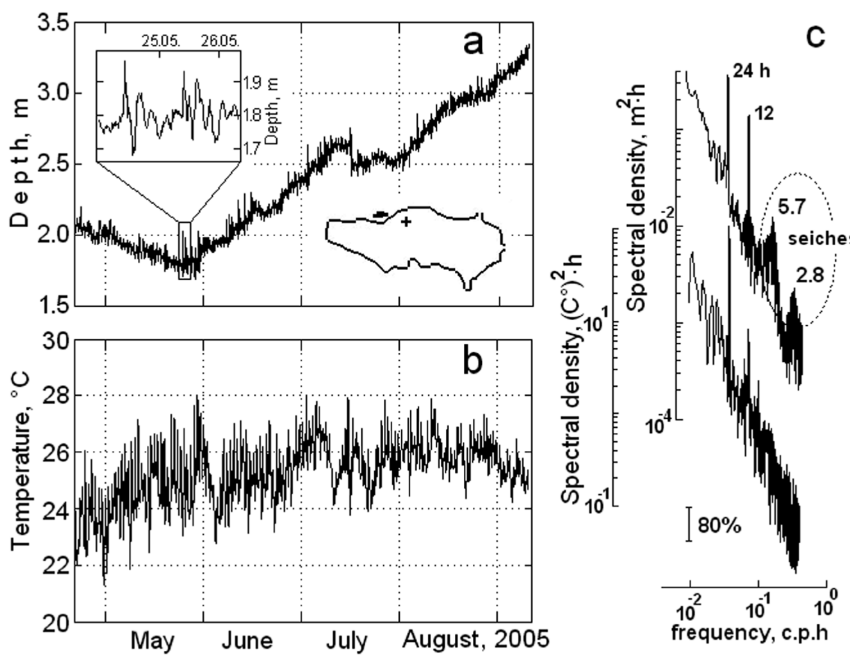

Figure 2. (a) Hourly fluctuations of lake level and (b) temperature fluctuations at a mooring during the experiment in the summer 2005. (c) Frequency spectra of a level and temperature fluctuations. Arabic numerals showing the period of the main peaks in the spectrum. The vertical line shows the 80% confidence interval.

We used the Merian equation (Le Blond and Mysak, 1978) to evaluate the theoretical periods of the two principal waves. The period of lake-level oscillations of the first mode is given by $\pi = 2L/\left(n \cdot \sqrt{g \cdot H}\right)$, where *H* is the average depth; *L* is the length of the lake, *n* is the horizontal mode number and *g* is acceleration of gravity. It is known that the maximum length of the lake is 75 km and the average depth is 6 m (Filonov, 2002). Thus the periods of the first and second modes of horizontal oscillation are 5.5 and 2.7 hours, respectively. These results closely match those obtained from our measurements. The seiche oscillation periods in Lake Chapala depend mainly on the mean depth of the lake as the length along the major axis of the lake is almost unchanged. Interannual fluctuations of the Lake Chapala can reach 6 m, for example, in 1955-1960 (Tereshchenko *et al.,* 2002), therefore in extreme years the seiche periods may vary (increase or decrease) from 4 to 7 hours.

The principal dynamic process that occurs in the lake is the lake breeze circulation. Daytime breeze speed does not usually exceed 4 m/s. Beyond any doubt the lake breeze causes the increase in the evaporation from the lake's surface. Lake breeze, together with atmospheric pressure variations, generate free seiche waves.

North-south temperature cross-section of the lake

The spatial distribution of surface temperature across the Lake Chapala was previously discussed in the work of Tereshchenko, *et al.,* 2002, based on extensive satellite data sets with high spatial resolution. In that study, it was shown that the northern part of the lake is warmer than its central and southern parts, which is caused by the specific features of its circulation.

To confirm this finding and shed light on other processes that occur in the lake, north-south temperature cross-sections were carried out in February, April, July and October 2006. Each survey included 60 equidistant bottom casts, 250 m apart. The SBE19-plus CTD profiler with 0.17-second sampling rate was manually dropped from the boat with a speed of about 0.1 m/s. The coordinates of the casts were fixed by the Global Position System (GPS).

The measurements were taken in the morning (from 7:00 to 9:00 am), so that the temperature along the cross-section was not biased. The cross-section extends from the northern coast (near the town of Chapala) to the south side of the lake. The spatial distribution of temperature at the cross-section is shown in Figure 3.

It is seen from the Figure that the *in situ* measurements confirm the previous finding, namely that in all seasons the temperature in the central and northern parts of the lake is higher than in the southern part. This holds true not only for the surface but also for the bottom layer. In all four seasons, vertically-averaged temperatures at the north and south ends of the cross-section differ by 2-3 °C. The vertical distributions of temperature on the sections are uneven.

The northern part of the section shows the penetration of warm water from the anticyclonic gyre which is stationary in the study area at morning time. In April, July and October, the water columns in the central and southern parts of the lake were poorly stratified, which was probably caused by vertical mixing at night time. These results shed new light on the thermal structure of the lake obtained and discussed in previously studies (Filonov and Tereshchenko, 1999a; Filonov, 2002; Tereshchenko *et al.,* 2002; De-Anda, 2004). They should be taken into account in the design of future experiments in the study area and 3D model simulations.

Current simulations in the lake

In this study the current simulation was carried out using the HAMSOM 2-D hydrodynamic model (see appendix A) for a 30-day period during the dry and wet seasons. The model was initialized with wind fields from the network of weather stations in the Lake Chapala area collected in 2006-2007 (Figure 4). The river runoff data were obtained from CONAGUA (Mexico's National Water Council). The wet-season average of the inflow from the Lerma river was set to 600 cubic meters per second, the outflow through the Santiago river - 120 cubic meters per second.

We have performed 2D model simulations for the two seasons, for which we had acquired the current data using a towed ADCP. The simulations were performed on a bathymetry grid with a 300 x 300 m spatial resolution (97 rows and 270 columns) and 3-second time step.

The model results are shown in Figure 5 as vector plots of current fields at 4-hour intervals. The breeze-induced circulation pattern in the

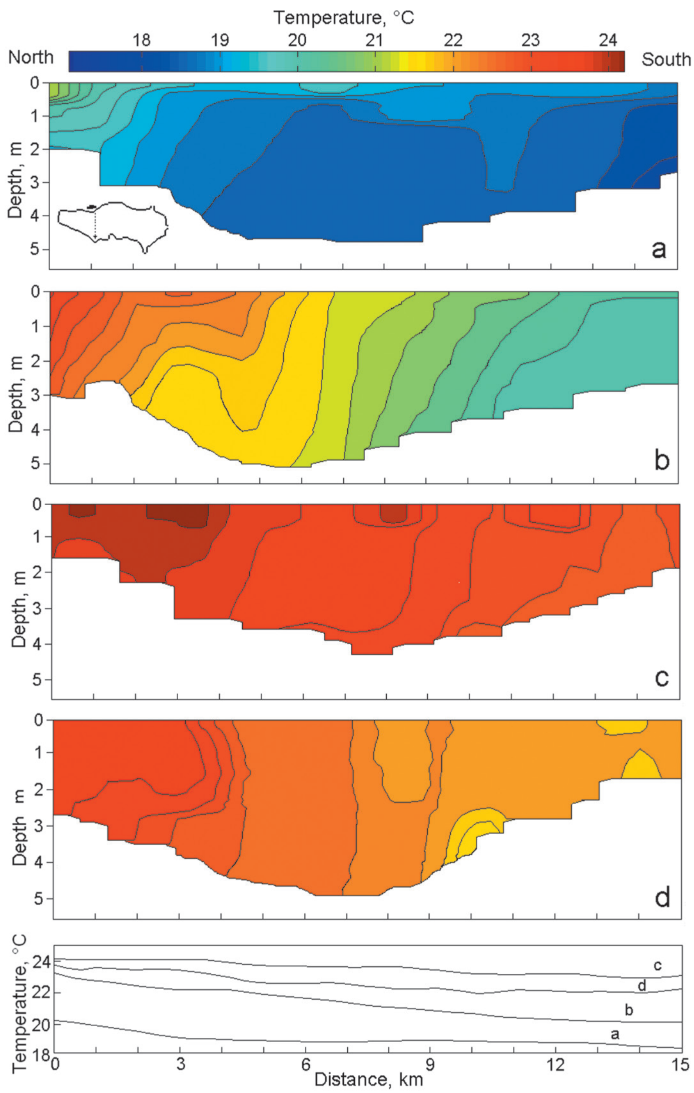

Figure 3. Vertical sections of temperature variation across the lake made in February (a), April (b), July (c) and October 2006 (d). In the lower part of the figure shows the graph of the vertical averaged temperature at the sections.

lake is represented by two gyres. One of them is cyclonic (counterclockwise rotation) and located in the east-central part of the lake. The other gyre is anticyclonic (clockwise rotation) and located in the west-central part. The model results exhibit a very complex dynamics, whose small-scale features are difficult to interpret. Nevertheless, similar gyres were identified near the east and west coast.

The core of the anticyclonic gyre which was generated in the west part of the lake propagates to the northwest and continues to develop during the most part of the simulation period. Conversely, the cyclonic gyre originally located in the east-central part moves to the south-west part of the lake. Subsequently, it vanishes due to the bottom friction and its remainder merges into the returning flow of the anticyclonic gyre. The model simulations show that the currents near the south and north coast reach 12 cm/s. These and other model results require the comparisons with current meter data. Therefore, two special experiments were carried out in January 2007 and June 2014.

Temperature and currents variability within two lake polygons

In order to quantitatively describe the spatial-temporal variability of temperature and circulation in the Lake Chapala, two special experiments were conducted: (i) on January 10, 2007 (the Alacranes polygon, Figure 6a, center-left) and (ii) on June 1, 2014 (the Mezcala polygon, Figure 6a, center). Both experiments were conducted with the use of a vertical array of temperature recorders and a boat-mounted ADCP.

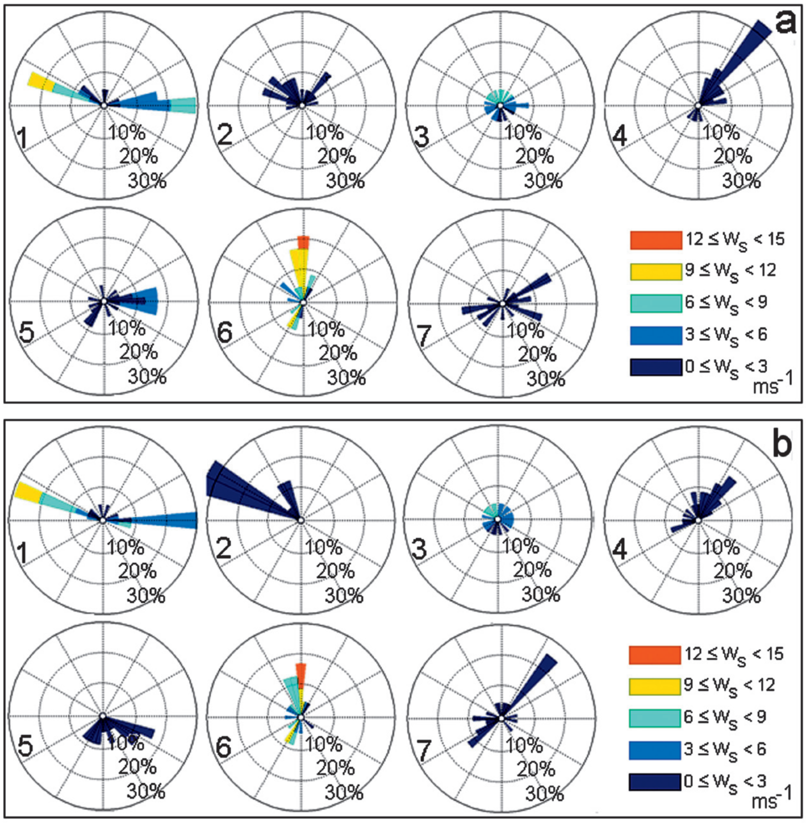

Figure 4. Annual wind rose at meteorological stations around the lake: a) for the dry season; b) for the wet season. The data was averaged for 2006-2007.

The array contained 15 temperature recorders (13 HOBO Pro v2, one HOBO-LEVEL sensor and one SBE-39), evenly placed from the surface to 7.2-m depth. The array was towed by the boat. A down-looking ADCP RDI 600 kHz set up in bottom-track mode was mounted on the starboard side of the boat. The bin size was set to 15 cm (the total of 13 bins) and the ensemble interval was 15 sec.

The instruments were protected from fishing nets by a specially designed triangular metal case shaped to fit the recorders so that no damage was caused by the fishing gear. The designated depth of the array was controlled by HOBO-LEVEL and SBE-39 pressure sensors and weights (Figure 6b). The sampling rate of temperature and pressure sensors was 1 min. The towing speed of about 2 m/s allowed the acquisition of temperature and currents data with the horizontal spatial resolutions of 120 and 30 m respectively.

The ADCP data were processed in accordance with Trump and Marmorino (1997) and outliers were removed following the procedure described in Valle-Levinson and Atkinson (1999).

The Alacranes Polygon

The spatial distribution of temperature along the transect **S** (carried out from 12:00 to 14:30, the boat sailed southward) is shown in Figure 7a. The transect **N** (on which the boat sailed from south to north) was carried out from 16:40 to 17:50 and the corresponding temperature field is shown in Figure 7b. On both transects, the meteorological conditions were recorded. During the transect **S** the average air temperature was 14.5 ºC; the wind was blowing onshore, and its speed was 12 m/s. Later, during the transect **N,** the average air temperature was higher and reached 20.9 ºC; the wind was blowing offshore, which is a typical breeze circulation in the Lake Chapala (Filonov, 2002).

It is seen from these transects that the heat fluxes were directed towards the surface layer of the water column, whereby the vertical gradient reached 2.5 ºC per the top meter of the column. During the transect **a)**, all temperature fluctuations were confined between 17 and 18.5 ºC. A few hours later the rapid development of a thermocline was observed on transect b) (Figure 7) with temperatures ranging between

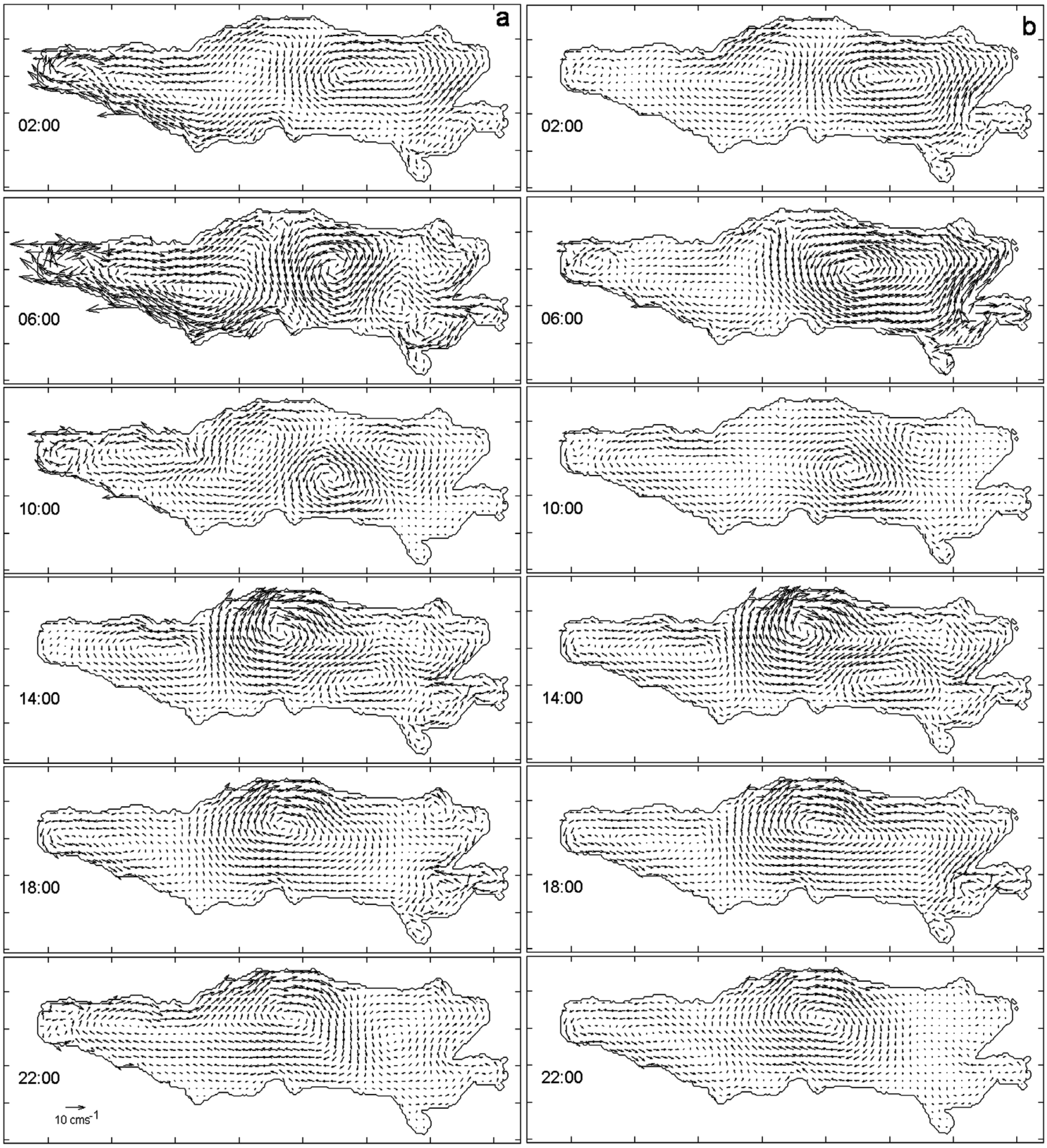

Figure 5. Result of the currents simulation induced by the wind fields in the lake: a) for the dry season; b) for the wet season. The data was averaged for 2006-2007.

17 and 20 ºC. At the end of the b) transect, the coastal water began to mix due to the lake breeze effect. Furthermore, at the north end of the transect a) the water was warmer than at the south by 1ºC (Figure 7).

The wind field is believed to be the main mechanism that continually sustains the circulation in the Lake Chapala, including the gyres. Figure 8 presents the vector plots of vertically averaged currents measured by the towed ADCP and simulated by the HAMSOM model. In general, the modeled and observed data are in good agreement.

The transect a) was carried out from 12:00 to 14:30, while the boat was sailing from north to south. The speed of the northeastward flow along the transect peaked at 10 cm/s. The flow was presumably generated by the prevailing onshore wind dubbed "the Mexican" by local fishermen (Avalos, 2003). The 13:00 model simulations are in good agreement with the data collected in the northern part of the lake (Figure 8a). At the same time the south part is characterized with a significant difference between the modeled and observed data, both in terms the currents and temperature field.

Figure 6. a) General scheme of experiments on Lake Chapala conducted on January 10, 2007 (polygon Alacranes left of the center of the figure) and June 1, 2014 (polygon Mezcala, in the center of the figure). b) Scheme of the towed sensor system. 1- 600 kHz RDI ADCP, 2 – Metallic angular pattern in which fixed thermographs, 3 - thermograph's mount, 4 - lattices for deep penetration of the chains.

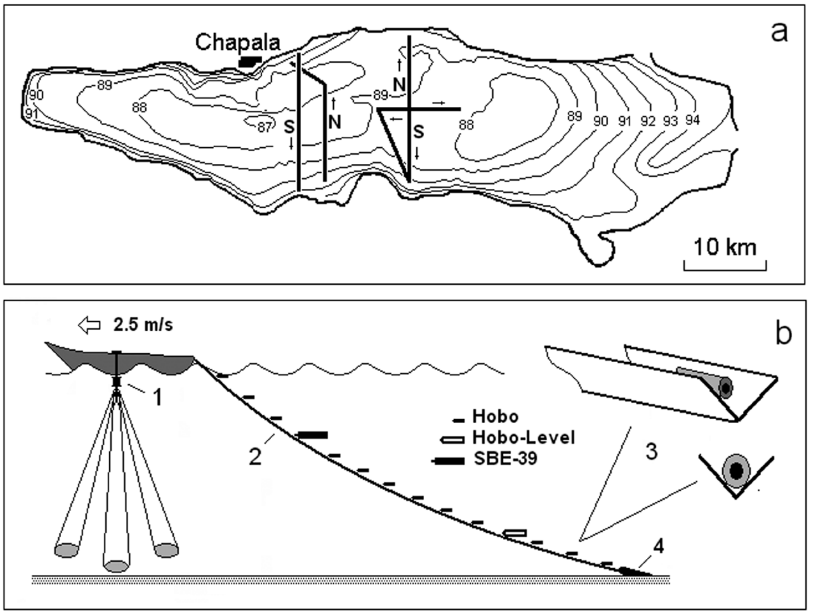

Nevertheless, the transect b) data collected between 16:30 and 18:00 show fairly good agreement with the southern part of the 18:00 model field, with velocities reaching 15 cm/s. It was found that in the southern part of the lake, the direction of the flow can change from west to south in only two hours. The wind speed of 12 m/s was recorded by the Chapala city weather station at the same time when transect a) displayed southeastward flow. In just two hours upon the completion of transect b) the wind changed its direction to southeastward and gained speed of 10 cm/s. These results suggest that the model successfully simulates the effect of the morning breeze circulation.

The Mezcala Polygon

The model simulations show the presence of a steady anticyclonic gyre of 10-12 km diameter in the central part of the lake, across from the town of Mezcala, during both seasons (Figure 5b). To confirm these numerical calculations we have carried out the Mezcala polygon survey. The temperature and currents within the gyre where observed with the use of towed temperature recorders and ADCP. The cross-shaped polygon of about 6-km length was situated in the deepest part of the lake, inside the gyre. Continuous measurements along the three directions (Figure 6a) were taken on July 1, 2014 from 8:30 to 19:00, whereby the boat was sailing back and forth.

Figure 7. Vertical sections of temperature variation across the lake made on transect north-south (S) and south-north (N), registered by the sensor chains on January 10th, 2007, in Chapala's lake. The lower figure is a vertically average spatial range from the transect S and transect N.

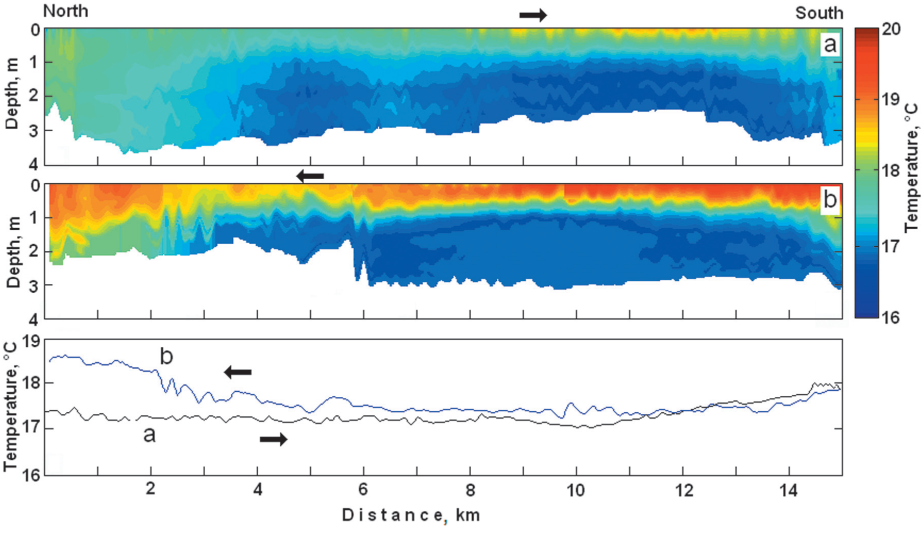

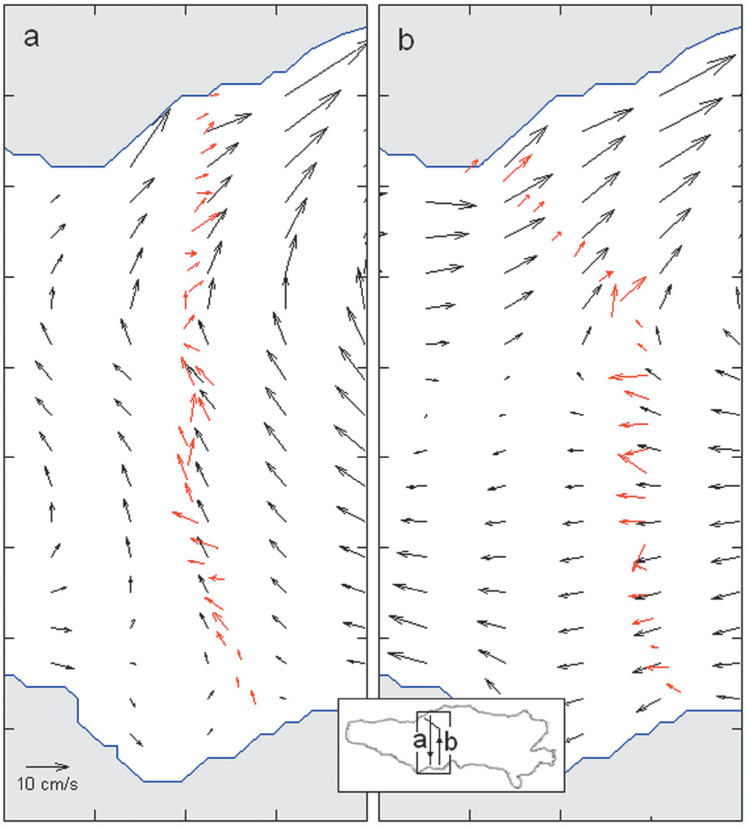

Figure 8. (a) Modeled currents (black vectors) versus currents observed (red vectors) in the area of the S transect sampling, and for N transect. The experiment was conducted on January 10, 2007, the simulations were at 12:30 and 19:00, respectively.

Presented in Figure 9 are the temperature distributions along the two transects: the transect a), which was carried out from 8:30 to 10:20, while the boat was sailing south and the transect b), which were carried out from 17:00 to 19:00. The meteorological conditions during the experiment were typical for this time of the year: the morning was calm followed by a moderate breeze in the afternoon. The towing speed was higher than on the Alacranes polygon, therefore the deepest recorder was only at a 2.2-m depth. Nevertheless, the collected data shed a new light on the horizontal and vertical structure of the temperature field on the polygon in the presence of the anticyclonic gyre.

As seen from Figure 9a, in the morning, at the time when the boat was sailing south (from 9:15 to 10:22 AM), the stratification of the lake was moderate. The average temperature near the southern shore of the lake was steady at 23.4 °C (Figure 9b). During the reverse leg along the transect (from the south to the north) the measurements were taken only in the afternoon (from 17:00 to 19:00), when the wind and temperature conditions over the lake were quite different from the morning. The simulated currents are reasonably comparable with the observed data and suggest that in the second half of the day the gyre was well-developed. The gyre exerts a strong impact on the spatial temperature distribution in the study area.

A zone of strong vertical mixing was discovered on the last leg, about 1 kilometer east from the Mezcala Islands, when the array of the recorders was towed from the south to the north. These islands are about 1.5-km long. They are perpendicular to the flow of the gyre and create dynamic shadows (the shaded area in Figure 10). Within this area, the upwelling of cold bottom water due to the Bernoulli effect resulted in its mixing with the warm surface water. Unfortunately, the spatial grid of the model (300x300 m) was too coarse to simulate this effect.

More detailed hydrographic surveys off the Mezcala Islands and the Alacranes polygon are planned for the future with the subsequent assimilation of the collected data into 3D numerical models. This will allow us to confirm the above mentioned assumptions about the impact of the vortex on the vertical and horizontal mixing near the islands.

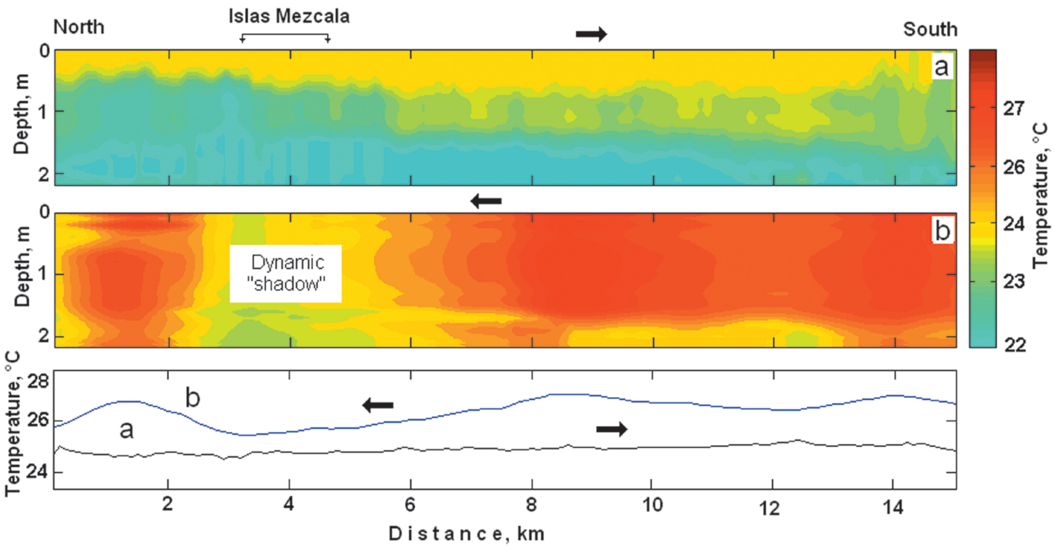

Figure 9. Vertical sections of temperature variation across the lake were taken on transect north-south (S) and south-north (N), registered by the sensor chains on July 1, 2014. (c) Vertical average spatial range from transect S and transect N. (d) Simulation corresponding to 18:00 (black vectors) versus currents observed (red vectors) in the area of sampling at polygon Mezcala.

Discussion and conclusions

A great deal of results presented here are unique for the Lake Chapala. Although this study was carried out during different time periods, on average it gives a fair account of the dynamic processes occurring in the lake and its surroundings. The main dynamic process occurring in the lake is the breeze circulation. The daytime breeze does not usually exceed 4 m/s. Beyond any doubt the lake breeze results in the increased evaporation from the lake's surface and also generates free seiches waves.

The spectral analysis of the lake level fluctuations measured by a high-precision HOBO-Level recorder shows that there are two seiches modes in the lake with the periods of 5.7 and 2.8 hours, with the average amplitudes of 15.4 and 8.1 mm. Our earlier study (Filonov, 2002) reports almost similar results, except that there is no well-defined mode with the 2.8-hour period due to the weak amplitude. The seiches generate periodic currents which peak at 1 cm/s in nodal line areas (Filonov, 2002).

The spatial distribution of surface temperature in the Chapala Lake has been previously discussed in the works of Filonov and Tereshchenko, 1999a, 1999b; Filonov *et al.,* 2001; Filonov, 2002, based on the data sets acquired with the use of high-precision instruments. Tereshchenko, *et al.,* 2002 report the results of the analysis of fairly long temperature data sets remotely sensed with high spatial resolution (the AVHRR-NOAA satellite images). The study shows that the northern part of the lake is warmer than its central and southern parts, which is essentially an important feature of the circulation. However, until now there were no detailed accounts of the horizontal and vertical structure of the temperature field in the lake in different seasons.

Our *in situ* measurements taken in February, April, July and October 2006 confirmed the previous finding that the temperature in the central and northern parts of the lake during different seasons is always higher than in the southern part, which holds true not only for the surface but also for the entire water column. In all four seasons the average temperatures at the north and south coast's differ by 2-3 °C. The vertical distribution of temperature along the transects was not homogeneous.

The results of numerical simulations of the Lake Chapala circulations are reported in some publications (Simons, 1984; Escalante, 1992; Filonov and Tereshchenko, 1999a; Filonov, 2002; Avalos, 2003), but none of them is based on the experimental and observational wind data sets collected in the study area during different seasons.

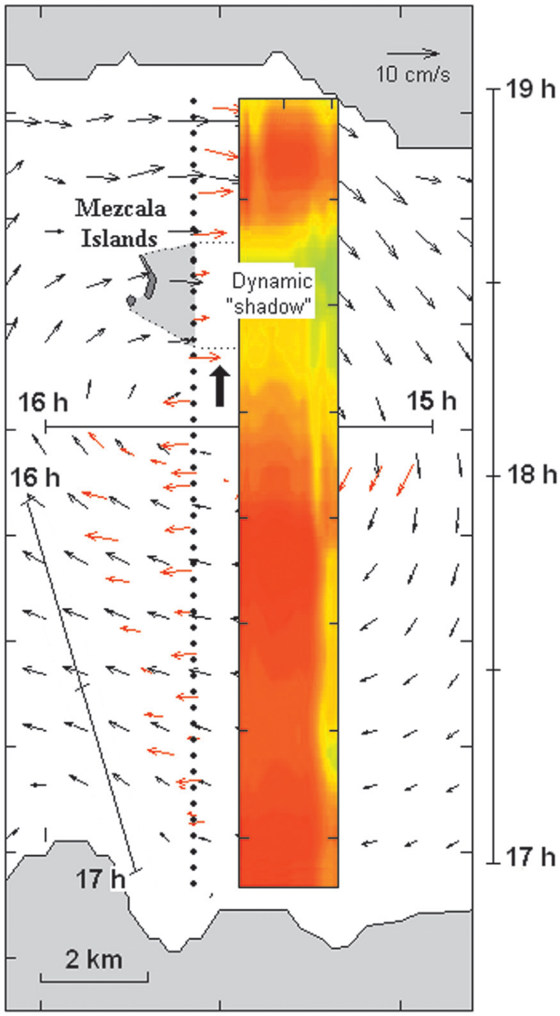

Figure 10. Modeled currents (black vectors) versus currents observed by towing ADCP (red vectors) at the Mezcala region. The experiment was conducted on January 10, 2007. The simulations were from 15:00 to 19:00, respectively. The bullet points with the arrow show the direction of the towed sensor system on the section of South-North. Color stripes are a sectional view of the temperature field. The straight thin lines on figure show the sections taken at appropriate times.

In this study the simulation of currents was carried out by means of the 2D HAMSOM model for the dry and wet seasons. The model was initialized with the wind data from the network of weather stations in the Chapala Lake area collected in 2006-2007. The model results demonstrate very complex dynamics, in particular, the continuous presence of two gyres. One of them rotates counterclockwise (cyclonic rotation) and is located in the east-central part of the lake. The other one rotates clockwise (anticyclonic rotation) and is located in the west-central part.

In order to describe the spatial-temporal variability of temperature in the lake and compare the model simulations with the observed data, two special experiments were conducted in the Lake Chapala on January 10, 2007 (polygon Alacranes) and on June 1, 2014 (polygon Mezcala). In these experiments a vertical array of temperature recorders aligned in the antenna-like pattern was towed along the transect by a boat with onboard ADCP. These high-frequency measurements on both polygons shed new light on the distribution of temperature and currents in these parts of the lake. The data collected on the Mezcala polygon confirm the presence of an anticyclonic gyre and show the influence of the islands on the dynamics of water masses and the temperature distribution in the lake.

Acknowledgements

The authors are also grateful to the Consejo Nacional de Ciencia y Tecnología (Mexico) for their financial support of projects 33667-T and 41667.

References

Aparicio J., 2001, Hydrology of the Lerma-Chapala watershed. Chapter of the book: "The Lerma-Chapala watershed: evaluation and management", Kluwer Academic Publishers/Plenum Press, New York, pp. 151-182.

Ávalos-Cueva D., 2003, Circulation of breeze and its influence on the thermal structure of Lake Chapala, Mexico. Master of Science Thesis in Spanish. University of Guadalajara, Jalisco, 61 p.

Backhaus J.O., 1983, A semi-implicit scheme for the shallow water equation for application to shelf water sea modeling. *Continental Shelf Research*, 2, 243–254.

Carbajal N., 1993, Modeling of the Circulation in the Gulf of California. Ph. D. Thesis. Institute of Oceanography. University Hamburg. 186 p.

De-Anda J., 2004, Solids distribution in Lake Chapala, México. *Journal of the American Water Resources Association*, 40, 97-109.

Escalante M.E., 1992, Transporte de contaminación en el Lago de Chapala (etapa inicial) informe técnico CH-9206/07.

Filonov A.E., Tereshchenko I.E., 1997, Preliminary Results on the thermic regime of Chapala Lake, Mexico. *Suppl. to EOS Transact*, AGU, 78, 46.

Filonov A.E., Tereshchenko I.E., 1999a, Thermal fronts and internal nonlinear waves in shallow tropical Lake Chapala, Mexico. *Russian Meteorology and Hydrology*, 1, 58-64.

Filonov A.E., Tereshchenko I.E., 1999b, Thermal lenses and internal solitones in the shallow lake Chapala, Mexico. *Chinese Journal of Oceanology and Limnology*, 17, 308-314.

Filonov A.E., Tereshchenko I.E., Monzón C.O., 1998, Oscillations of the hydrometeorological characteristics in the region of Lake Chapala for intervals of days to decades. *Geofísica Internacional*, 37, 393-308.

Filonov A.E., Tereshchenko I.E., Monzón C.O., 2001, Hydrometeorology of Lake Chapala. Chapter of the book: "The Lerma-Chapala watershed: evaluation and management", Kluwer Academic Publishers/Plenum Press, New York, pp. 151-182.

Filonov A.E., Tereshchenko I.E., Alcocer J., 2006, Dynamic response to mountain breeze circulation in Alchichica, a crater lake in Mexico. *Geophysical Research Letters*, 33, L07404, doi:10.1029/2006GL025901.

Filonov, A.E., Tereshchenko I.E., Alcocer J., Monzón C.O., 2015, Dynamics of internal waves generated by mountain breeze in Alchichica Crater Lake, Mexico. *Geofísica Internacional*, 54, 1, 21-30.

Filonov A.E., 1998, ¿Morirá el lago de Chapala? Existe la posibilidad de salvarlo. *Teorema* 3, 16-18.

Filonov A.E., 2002, On the Dynamical Response of Lake Chapala, Mexico to lake breeze forcing. *Hidrobiología*, 467, 141-157.

Hansen A.M., 1994, Migración de la Contaminación. *Gaceta del Lerma Especial*, 77-93.

Hansen A.M., Manfred van Afferden, 2001, Toxic substances. Chapter of the book: "The Lerma-Chapala watershed: evaluation and management", Kluwer Academic Publishers/ Plenum Press, New York, pp. 95-121.

Jay J.A., T.E. Ford, 2001,Water concentration, bioaccumulation, and human health implications of heavy metals in Lake Chapala. Chapter of the book: "The Lerma-Chapala watershed: evaluation and management", Kluwer Academic Publishers/Plenum Press, New York, pp. 123-136.

Jáuregui E., 1995, Rainfall fluctuations and tropical storm activity in Mexico, *Erdkunde* 49, 39-48.

LeBlond P.H., Mysak, L.A., 1978, Waves in the Ocean. *Elsevier Oceanography Series* 20, Amsterdam, 602 pp.

Marinone S.G., 2003, A three-dimensional model of the mean and seasonal circulation of the Gulf of California. *Journal of Geophysical Research: Oceans* 108:C103325.

Mosiño P.A., E. Garcia E., 1974, The climate of Mexico. In Bryson R.A., F.K. Hare (eds). The Climates of North America. Word survey of climatology Elsevier Sci. New York. 11, 345–404.

Riehl H., 1979, Climate and Weather of the Tropics. Academic Press. London. 611 pp.

Sandoval F., 1994, Pasado y futuro del Lago de Chapala. Editorial UNED. Guadalajara, México. 94 pp.

Serrano D., Filonov A.E., Tereshchenko I.E., 2002, Dynamic response to valley breeze circulation in Santa Maria del Oro, a volcanic lake in Mexico. *Geophysical Research Letters*, 29, 27-31.

Simons T.J., 1984, Effect of outflow diversion on circulation and water quality of Lake Chapala. Report Project MKX CWS-01: 23pp.

Scorer R.S., 1978, Environmental Aerodynamics. John Wiley, New York, 523 pp.

Tereshchenko I.E., Filonov A.E., Gallegos A., Monzón C.O., Rodríguez R., 2002, El Niño 1997–98 and the hydrometeorological variability of Chapala, a shallow tropical lake in Mexico. *Journal of Hydrology*, 264, 133-146.

Trump C.L., Marmorino G., 1997, Calibration of a gyrocompass using ADCP and DGPS data. *Journal of Atmospheric and Oceanic Technology*, 14, 211–214.

Valle-Levinson A., Atkinson L., 1999, Spatial gradients in the flow over an estuarine channel. *Estuaries and Costs*, 22, 179-193.

Geofísica Internacional (2016) 55-3: 189-198

Original paper

Eliminated aliasing effect on wavelet transform based multiresolution analysis

Ernesto González-Flores*, José Oscar Campos-Enríquez, Erick Camacho-Ramírez and David Ernesto Rivera-Recillas

Received: September 04, 2015; accepted: May 11, 2016; published on line: July 01, 2016

DOI: 10.19155/rgi20165531611

Resumen

El análisis multiresolución basado en la transformada ondicular discreta se incorpora al procesamiento de señales sísmicas. Ésta técnica de análisis permite descomponer una señal sísmica en diferentes bandas de frecuencia, y así analizar la información contenida en dichas bandas. El análisis de multiresolución permite visualizar en el dominio del tiempo la información contenida en las bandas de frecuencia. Las ondículas usadas comúnmente en la transformada ondicular discreta presentan un traslape entre escalas, lo que da origen a un efecto aliasing e introduce información espuria. La ondícula Vaidyanathan minimiza el traslape entre escalas. Aplicamos esta ondícula a datos sintéticos y a un cubo sísmico 3D. De acuerdo a este estudio, los efectos espurios generados por el traslape entre escalas es minimizado con la ondícula Vaidyanathan.

Palabras clave: análisis multiresolución, descomposición espectral, transformada ondicular discreta.

Abstract

Multiresolution analysis, based on the discrete wavelet transform, is here incorporated in seismic signal processing. This analysis technique enables decomposing a seismic signal, in different frequency bands, and thus to analyze the information contained in these frequency bands. Multiresolution analysis allows visualizing in the time domain the information contained in the frequency bands. Wavelets commonly used in the discrete wavelet transform present an overlay between scales, this constitutes an aliasing effect that gives rise to spurious effects. Vaidyanathan wavelet minimizes the overlay between scales. We applied this wavelet to synthetic data and to a 3D seismic cube. Accordingly, spurious effects from aliasing generated by overlay between scales are minimized with the Vaidyanathan wavelet.

Key words: multiresolution analysis, spectral decomposition, discrete wavelet transform.

E. González-Flores*
D. E. Rivera-Recillas
Instituto Mexicano del Petróleo
México D.F., México
**Corresponding author: 85ernesto@gmail.com*

E. Camacho-Ramírez
E. González-Flores
Posgrado en Ciencias de la Tierra
Universidad Nacional Autónoma de México
Ciudad Universitaria
Delegación Coyoacán, 04510
México, D.F. México

J. O. Campos-Enríquez[3]
Instituto de Geofísica
Universidad Nacional Autónoma de México
Ciudad Universitaria
Delegación Coyoacán, 04510
México, D.F. México

E. Camacho-Ramírez
Petróleos Mexicanos
Activo de Producción Samaria Luna Región Sur
México, D.F. México

Introduction

Seismic signal analysis plays a key role in petroleum exploration by helping to enhance information difficult to visualize naked eye. Today several techniques and algorithms are used to interpret seismic 3-D data. Spectral analysis comprises several methods that enhance specific seismic information enabling to solve stratigraphic and structural details (i.e., Rivera-Recillas et al., 2005 and Coconi-Morales et al., 2010), to estimate reservoir dimensions, etc. Fourier transform is commonly used to analyze frequency content of a seismic signal. However, when frequency content varies with time, this tool cannot show time position of the frequency content. Spectral content of seismograms varies significantly with time, i.e., they are non stationary and require non-standard decomposition methods. The discrete wavelet transform enables decomposing a non–stationary time series in its different frequency components and transforms the time domain information into a time–scale domain where scale is inversely proportional to frequency.

Discrete wavelet transform (DWT) is based in filter bank theory. Convolution of a filter bank with a signal provides frequency rank windows. The filter banks for a particular wavelet must satisfy two conditions; must be of compact support and of zero average. This tool enables separating high frequencies from low frequencies and locating its position in time. A growing number of geophysical studies using DWT have provided satisfactory results; however sometime, separation between scales is not fully achieved due to an intra–scale coupling effect. So that, an appropriate wavelet is needed to conduct a successful data processing based in this technique. There are many wavelets but many present the aliasing problem, here we present a performance analysis of several wavelets with respect to the aliasing effect in multiresolution analysis of seismic signals. We tested the performance of Vaidyanathan wavelet with a real 3-D seismic cube data.

We first briefly introduce the wavelet theory. Then we describe the Vaidyanathan wavelet. We reconstructed seismic sections based in the respective multiresolution analysis of the Boonsville field seismic cube, located in north-central Texas (Bureau of Economic Geology, 1996). The seismic cube is open access and well documented.

Theory

A signal can be expressed in terms of a set of functions with different resolution. Multiresolution based on the discrete wavelet transform generates this function base, to each resolution a certain information content of the signal is associated. The theory of discrete wavelet transform has been exposed in many books (i.e., Hubbard, 1998; Chui, 1992; Dwight and Olejniczak, 2003). This technique can be developed on Daubechies´s (1992) pyramidal algorithm where the discrete wavelet transform is obtained by convolving the signal with a quadrature mirror filter (QMF) bank, built from a compact support and zero mean wavelet. The wavelet is dilated to different scales by a factor of two. Translation is done in binary form.

The dilatation and shifting of a wavelet $\psi(x)$, can be expressed as:

$$\psi(x)_{j,k} = 2^{-j/2}\psi(2^{-j}x - k) \qquad (1)$$

where j denote scale and k translation. At small scales, when the wavelet is contracted, high frequencies are displayed; at great scales, when the wavelet is expanded, low frequency contents are obtained. From expression (1) two functions are generated which are employed in the decomposition: a wavelet function as expression (1) and a scalar function as:

$$\varphi(x)_{j,k} = 2^{-j/2}\varphi(2^{-j}x - k) \qquad (2)$$

The functions $\psi(x)_{j,\,k}$ and $\varphi(x)_{j,\,k}$ generates a sub–set of a vector space that spans signals orthonormal to the analyzed signal.

The respective filter bank is constituted by one high and one low pass filter. The low pass filter is obtained from the wavelet function (ψ), while the high pass filter is obtained from the corresponding scalar function (φ).

So, when the high pass filter is applied to a non-stationary signal detailed coefficients are obtained, and when the low pass filter is applied to the same signal, we obtain smooth or approximate coefficients. The detail coefficients capture the top half frequency content of the data while the smooth coefficients contain the bottom half frequency content. This first step corresponds to the first decomposition level and is named first scale. To generate the next scale the smooth coefficients are used as input signal, and the above described process is repeated (Figure 1). To decompose the signal, a sub–sampling is done, because the translation of a wavelet along the signal is made in a binary form.

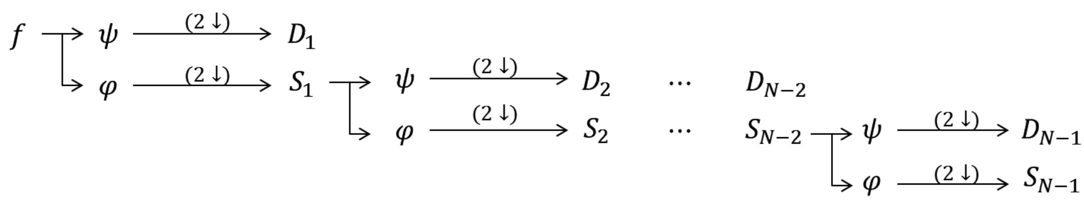

Figure 1. Schema of DWT decomposition. The signal f is non–stationary, φ is the low pass filter, ψ is the high pass filter, S_1 are smooth coefficients and D_1 are detail coefficients. The subscript indicates scale and 2↓ represents a sub–sampling.

The wavelet coefficients can be inverse transformed to exactly reproduce the original time series. This is achieved by using the filter bank in its synthesis form and reversing the sequence of the forward transform algorithm (Figure 2). Because the sub–sampling introduced in the forward decomposition, in reconstructing the signal it is needed an up–sampling by 2, and this can be achieved by adding one zero between two coefficients.

Vaidyanathan wavelet

As mentioned, discrete wavelet transform uses a wavelet to build an analysis based in frequency content, and such a wavelet can be derived from a pair of filters which satisfies the following frequency domain conditions for a perfect reconstruction (Foster *et al*., 1997):

$$L(\omega)\overline{L}(\omega)+H(\omega)\overline{H}(\omega)=2 \qquad (3)$$

$$L(\omega)\overline{L}(\omega+\pi)+H(\omega)\overline{H}(\omega+\pi)=0 \qquad (4)$$

where $L(\omega)$ and $\overline{L}(\omega+\pi)$ are an analysis low pass filter and a synthesis low pass filter, derived from a wavelet function (ψ), while $H(\omega)$ and $\overline{H}(\omega+\pi)$ are an analysis high pass filter and a synthesis high pass filter, correspondingly, obtained from a scalar function (φ). These conditions are known as normalization (Equation 3) and aliasing conditions (Equation 4). If aliasing condition is not satisfied, aliased energy will be present in the output signal. So that, orthonormal filter banks that satisficed this conditions are constructed by setting (Foster *et al*., 1997):

$$H(0)=e^{-i\omega}\overline{L}(\omega+\pi) \qquad (5)$$

$$\overline{H}(w)=e^{i\omega}L(\omega+\pi) \qquad (6)$$

these are known in the literature as a Quadrature Mirror Filter (QMF). In wavelet applications Finite Impulse Response (FIR) filters satisfying conditions (3) and (4), are compact support in the time domain, which is important for space–time operations.

There exists a group of wavelets that satisfies these conditions. The choice of a wavelet is very important for any wavelet domain processing application. In seismic processing it is desirable a wavelet that produces an optimal separation of information between scales and gives rise to a minimum overlap. Thus we need a wavelet which enables a perfect reconstruction and will minimize any artifact that may be introduced in the processing of a signal and appearing in its reconstruction.

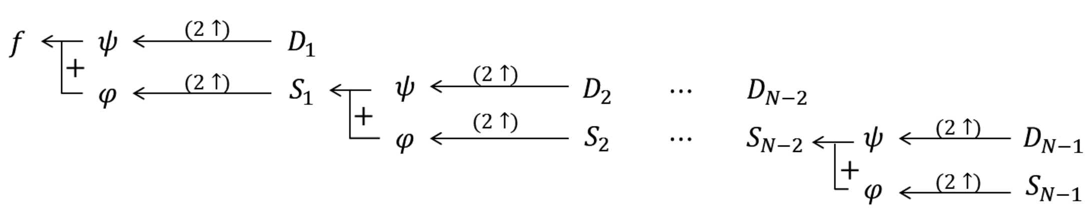

Figure 2. Schema of DWT reconstruction. The signal f is reconstructed, φ is the low pass synthesis filter, ψ is the high pass synthesis filter, S_1 are smooth coefficients and D_1 are detail coefficients. The subscript indicates scale and 2↑ is an up–sampling. Sign of plus indicate one sum between up–sampled detail and smooth coefficients.

There exists a two–channel QMF bank which satisfies the condition for a perfect reconstruction, and ensures a good stop–band of frequencies. Vaidyanathan and Hoang. (1988) introduced this filter. This wavelet is known as Vaidyanathan wavelet (Figure 3). We implemented the multiresolution analysis and conducted a performance test of several wavelets including the Vaidyanathan wavelet.

Programming

The programmed multiresolution analysis was based on the pyramidal algorithm, and on the 1D discrete wavelet transform. The programmed structure comprises five sub–programs to allow an optimal execution (Figure 4).

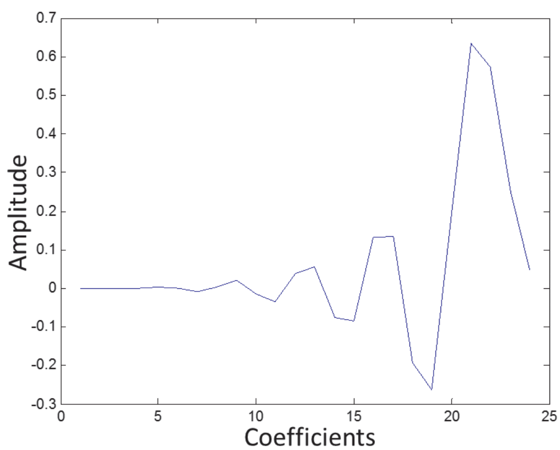

Figure 3. Vaidyanathan wavelet (Vaidyanathan and Hoang, 1988).

The objective of the first program is to communicate with the user (i.e., a friendly interface). Several windows enable the user to input the data file, to select a wavelet, as well as the scale or resolution level to be displayed.

The second sub–program distributes this information to other three sub–programs. The third sub program allocates enough space for all of the needed variables. The fourth subprogram contains all information defining each of the wavelets contained in the catalog shown in the first subprogram. Finally, the fifth subprogram performs the wavelet transform by means of the pyramidal algorithm.

This last subprogram analyses the seismic information trace by trace. It handles in this way a 3D data volume. When the user wants to elaborate a time–slice, this program shows the values at the user selected time. The case of one horizon is managed similarly.

Performance assessment

To assess how well isolated is the frequency content associated with a given scale was the goal of this study (i.e., which wavelet does preserve the power spectrum in an optimum way). Figure 5 shows a signal created by summing a series of sines with frequencies between 30 and 211 Hz. This signal encompass a wide frequency range: it has a 511 msec length and a sampling rate of 1 msec. It can be considered a non-stationary signal. This is not a seismic signal but is useful to assess

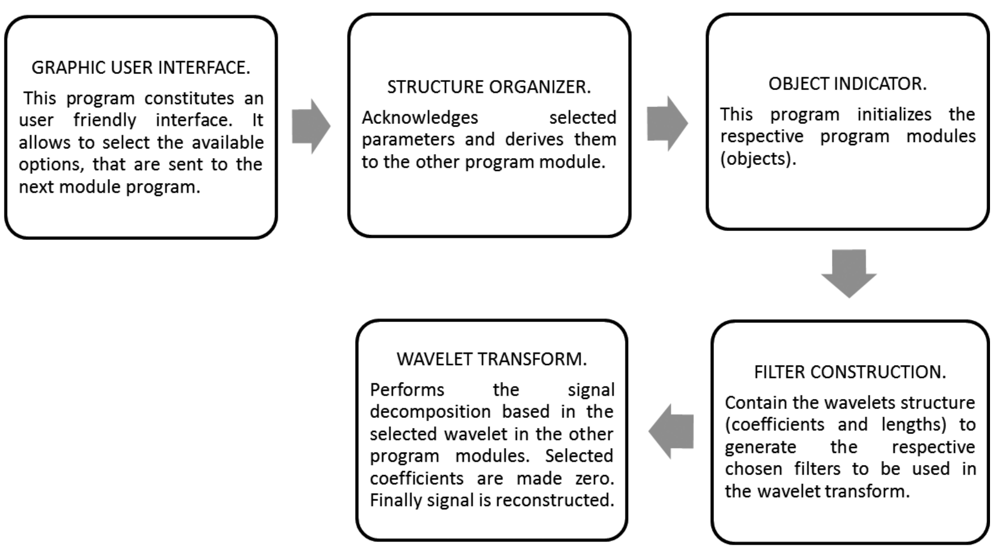

Figure 4. Structure of the developed program based in object oriented programming.

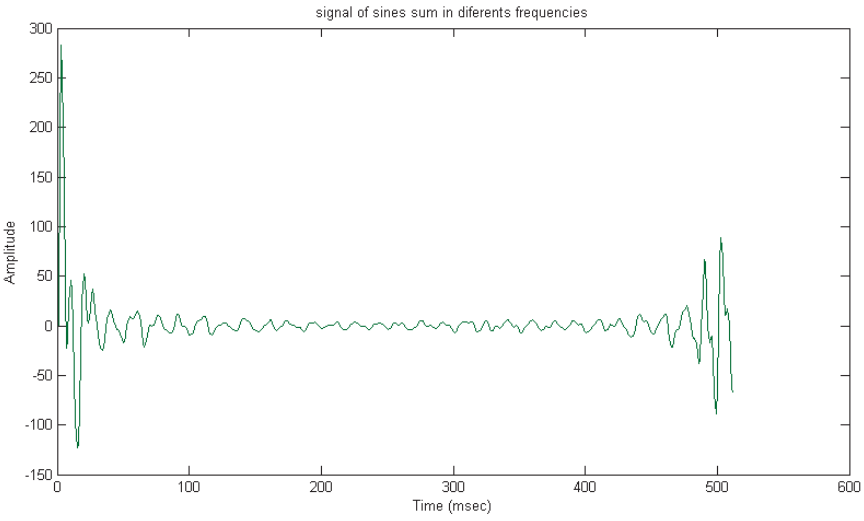

Figure 5. Signal created to assess the performance of several wavelets in multiresolution analysis. This signal is a sum of sine functions in the frequency range from 30–211 Hz.

the performance, in multiresolution analysis, of the following wavelets: Haar, Symplet, Coiflet, Daubechies (wavelets employed in Matlab, Misiti *et al*., 1996) and Vaidyanathan (Vaidyanathan and Hoang, 1988).

Figure 6 shows the power spectrums of the original signal and those corresponding to the second level (or scale) of the multiresolution analysis based on the above mentioned wavelets.

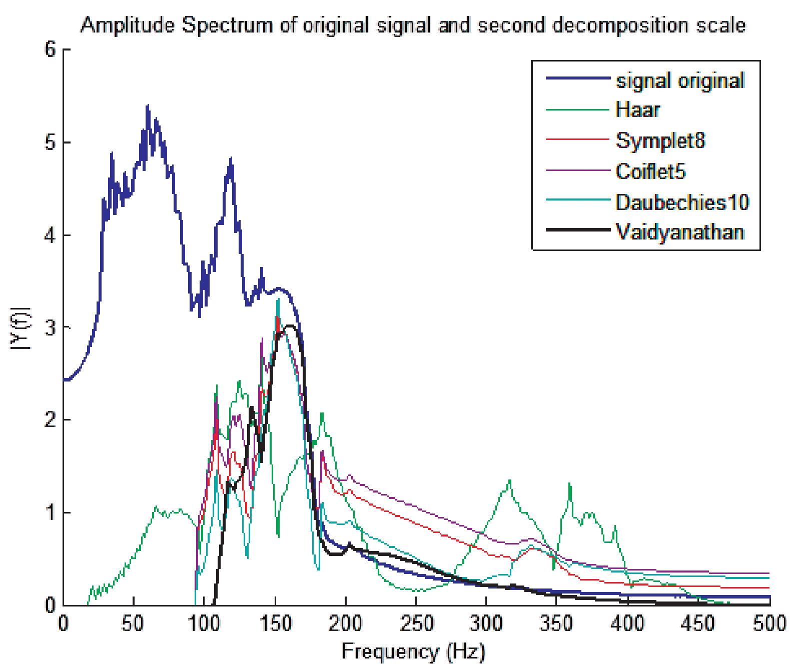

Figure 6. Power spectrums obtained from the multiresolution analysis using several wavelets. In blue line is presented the power spectrum of the original signal (Figure 5). Also, are presented power spectrums of multiresolution analysis based on the Haar, Symplet, Coiflet, Daubechies, and Vaidyanathan wavelets. The signal reconstructed corresponds to the second scale.

To the second decomposition scale approximately corresponds the frequency content between 125 and 250 Hz of the original signal. The original signal (blue line) power spectrum has a stronger gradient towards approximately 170 Hz. In this portion, the reconstructed spectrums from the multiresolution analysis based on Haar, Symplet, Coiflet, Daubechies wavelets show spurious effects. The exception corresponds to the Vaidyanathan wavelet. At 350 Hz approximately, Haar, Symplet, Coiflet, Daubechies wavelets produce a spurious pike, possible an armonic from the information contained in the frequency range of the second scale. We can see that for the Vaidyanathan wavelet this effect is minimum.

This performance analysis indicates that the Vaidyanathan wavelet best preserves the original signal power spectrum (i.e., it distorts in a minimum degree the spectrum of the original signal), so that, in particular, this wavelet is very well suited to conduct the multiresolution analysis (trace by trace in this study) of 3D seismic data, where it is very important to preserve the original seismic amplitude and no to introduce artifacts.

Example of multiresolution of 3D seismic data

Boonsville 3D seismic data

Boonsville 3D seismic dataset were obtained in the Jack and Wise counties, Fort Worth Basin, north–central Texas (Figure 7). The study area comprises approximately 67 km^2. The data are well documented and can be acquired from the Bureau of Economic Geology. Vaidyanathan and Hoang, (1988) wavelet based multiresolution analysis of the Boonsville 3-D seismic cube is now presented.

The data length is two seconds, sampling of the seismic data were done at 1 ms (Bureau of Economic Geology, 1996), with a 500 Hz corresponding Nyquist frequency. The dominat frequency is 57 Hz, with mean velocity of 3,600 m/s. According to Rayleigh criterium, the corresponding vertical resolution only allows to study layers with a thickness > 15 m.

Figure 8 shows the Boonsville seismic 3-D cube layout and the location of the oblique section used to illustrate the performance of the multiresolution analysis. This section was

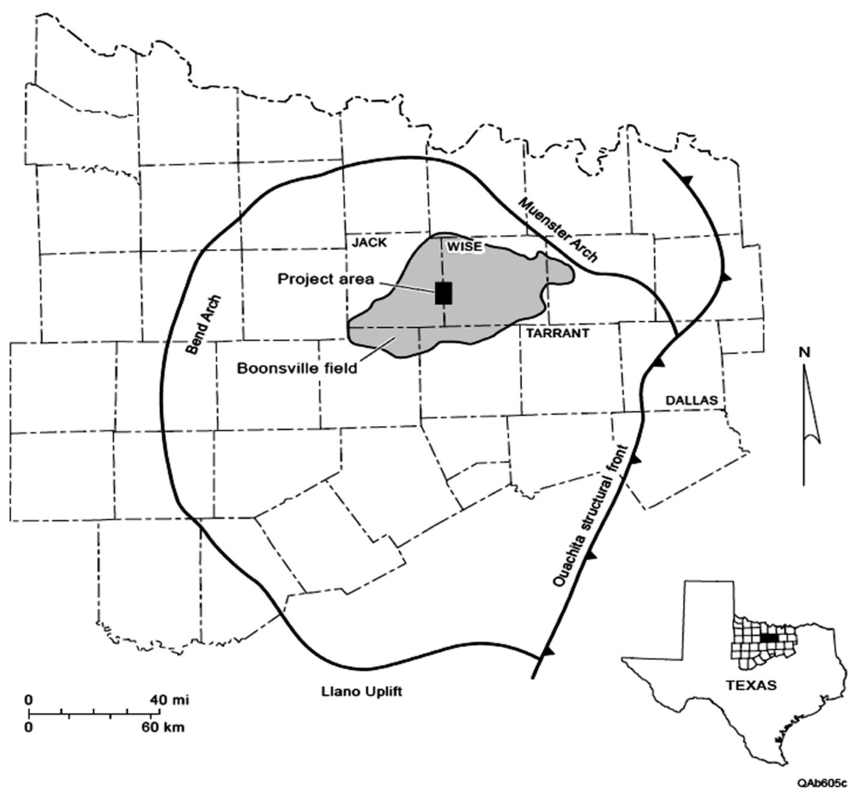

Figure 7. Boonsville study area is located between Jack and Wise counties , in North–Central Texas.

created to pass through two wells (BY11 and BY13 wells), because we wanted a zoom along of the well length to see information at detail. Figure 9 shows the seismic events along this oblique section, in the right lower part it is showed the respective power spectrum. We can shown that approximatly the dominant frequencies range from 30 to 115 Hz. We use one scale within this dominant frequency range to conduct an multiresolution analysis using Vaidyanathan wavelet and the Daubechies wavelet of order 10 (see Figure 6).

Figure 10 shows the reconstructed section using only the fourth scale (frequency content between 31.25 and 62.5 Hz). The respective multiresolution analysis was based on Vaidyanathan wavelet. Figure 11 presents the corresponding fourth scale obtained from the Daubechies wavelet of order 10 based multiresolution analysis.

The power spectra of the reconstructed sections based respectively on the Vaidyadanath and Daubechies wavelets (Figures 10 and 11) indicate that the aliasing effect due to the Vaidyanathan wavelet is not visible (i.e., negligible). However, the Daubechies wavelet of order 10 introduces high frequencies armonics enclosed by black elipsoids (i.e., a noticeable effect).

We can note that the seismic horizons in Figure 10 correlate quite well with the original seismic information. The seismic horizons in Figure 11 correlate fair well with then original seismic horizons. However, seismic horizonts in Figure 10 change its position along the seismic section in a smooth manner, but the seismic horizons in Figure 11 presents jumps. We believe that it is due to high frequency associated with the high frequency armonics introduced by the Daubechies wavelet of order 10 (see the power spectrum of Figure 11).

Finally, Figure 12 shows the FFT based bandpass filtered section of the original data. The band pass filter encompasses the fourth scale frequency range (31.25 – 62.5 Hz). Figures 10 and 12 correlate very well, which illustrates how the Vaidyadanath wavelet minimizes the aliasing effect.

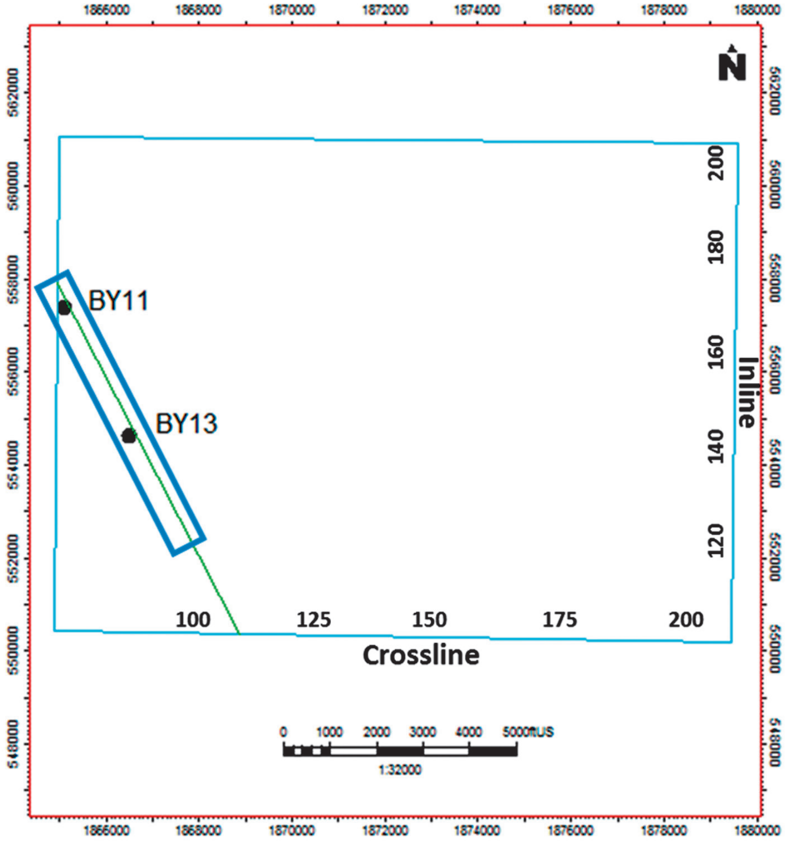

Figure 8. Locations of BY11 and BY13 wells in the Boonsville 3-D seismic cube. An oblique section through these wells was generated to test with a zoom along well lenghts.

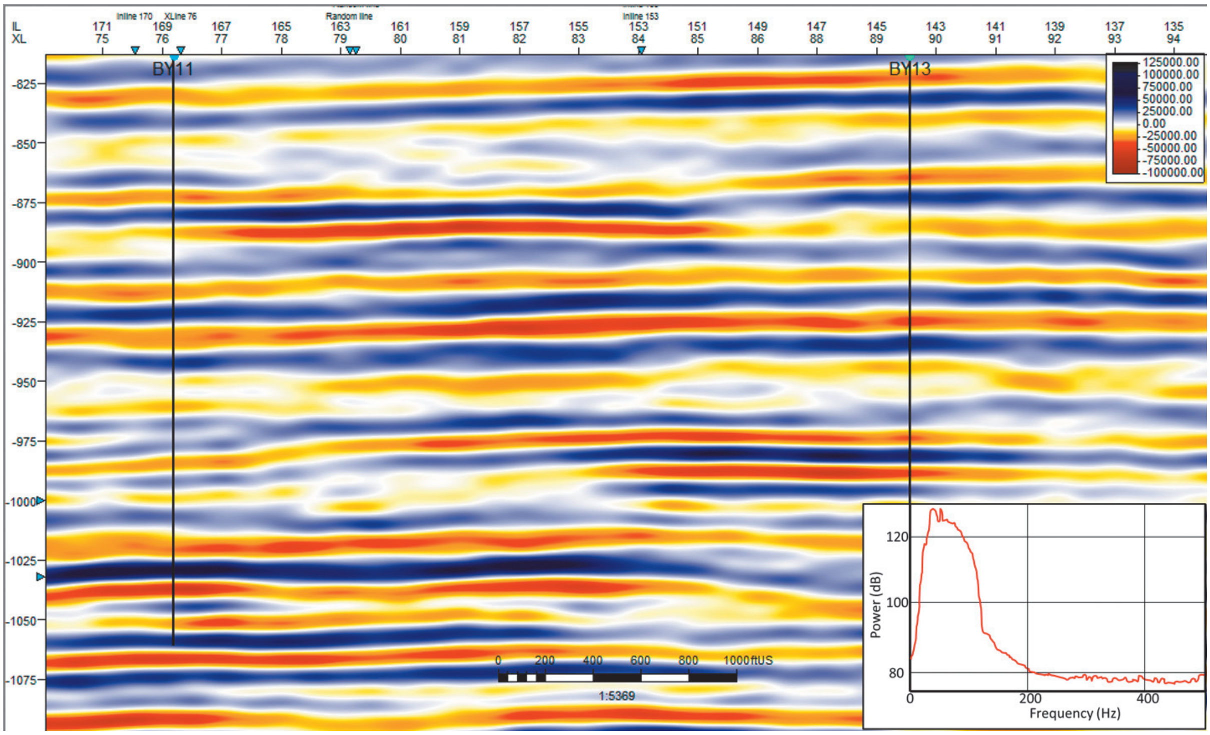

Figure 9. Oblique seismic section with original seismic (location in Figure 8) through wells BY11 (right) and BY13 (left). In the right lower part it is shown the respective power spectrum.

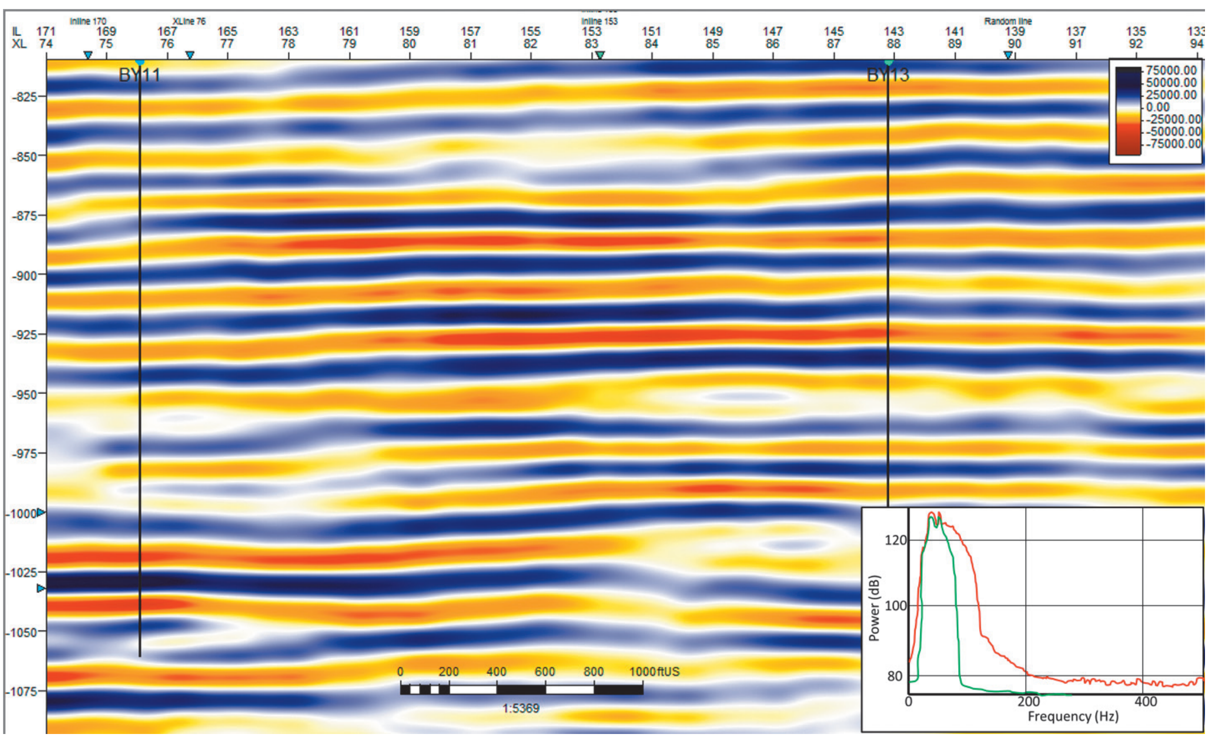

Figure 10. Seismic section reconstructed only from the fourth scale (31.25 to 62.5 Hz) using Vaidyanathan wavelet. In the right lower part it is shown the respective power spectrum.

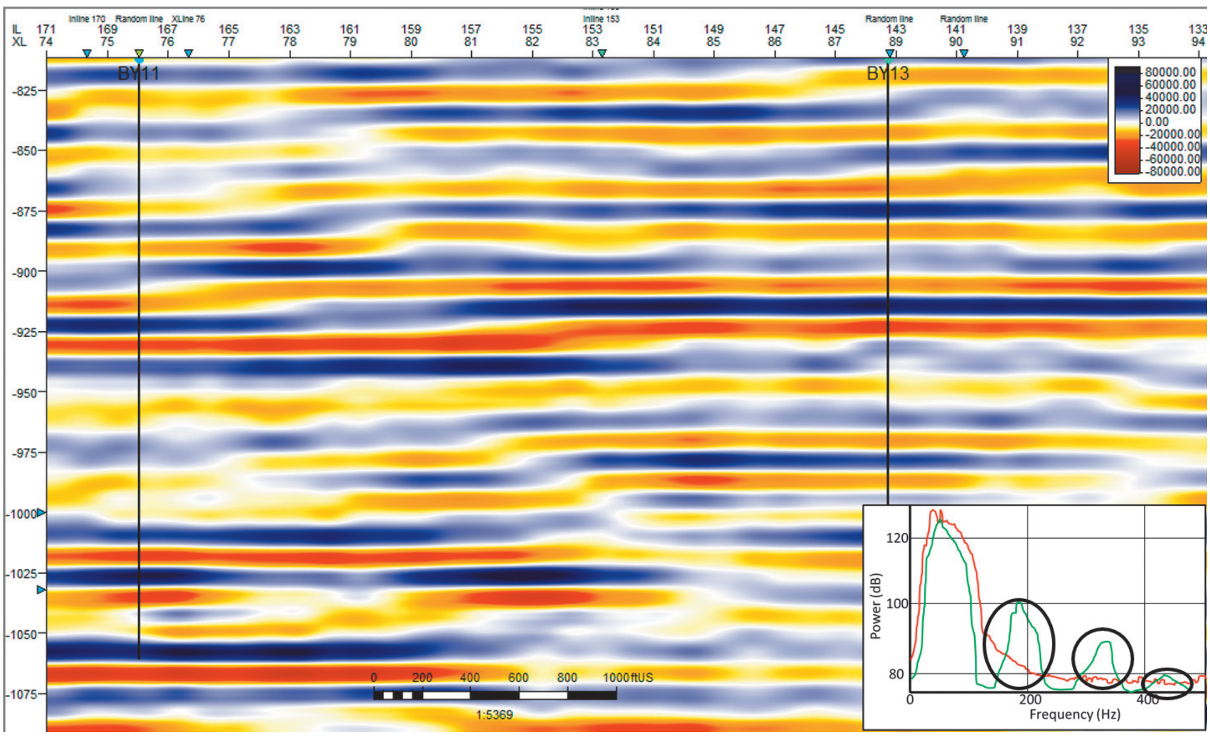

Figure 11. Seismic section reconstructed only from the fourth scale (31.25 to 62.5 Hz) using Daubechies wavelet of order 10. In the right lower part it is shown the respective power spectrum. Black ellipses indicate aliasing effect.

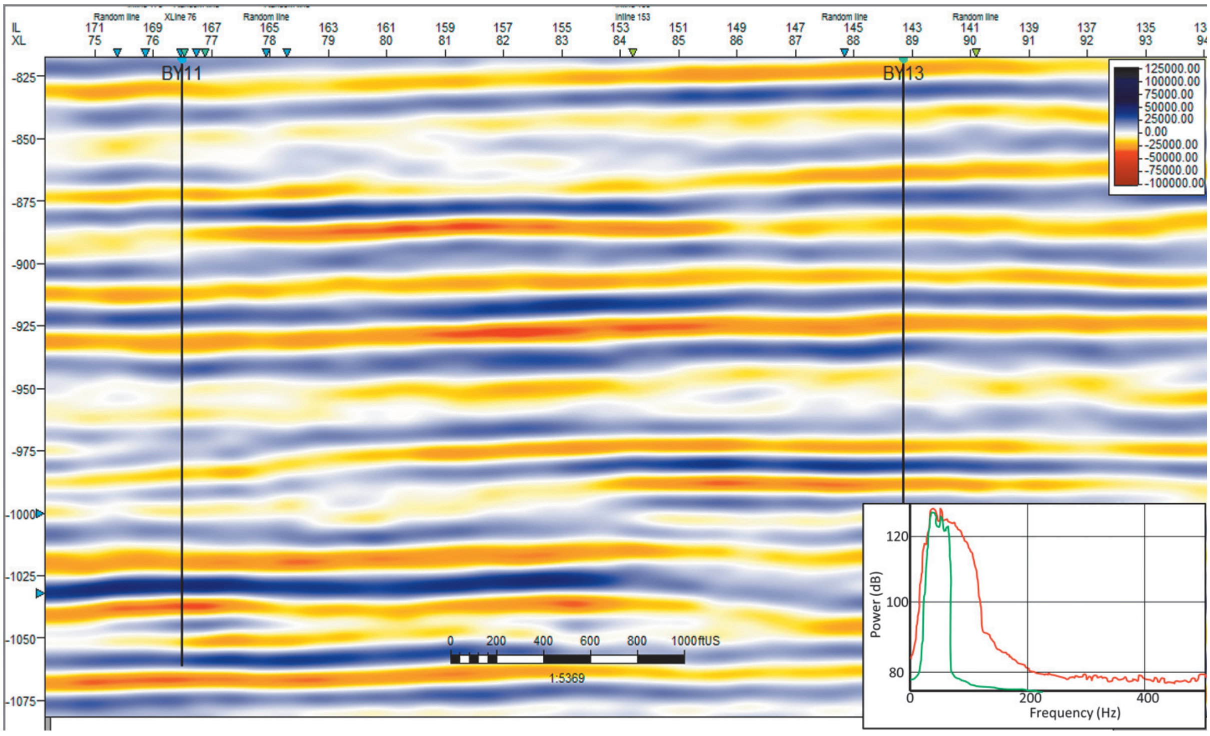

Figure 12.- Seismic section reconstructed from bandpass (using Fourier Transform) in frequency range of 31.25 to 62.5 Hz. In the right lower part it is shown the respective power spectrum.

Conclusions

This study reports a performance analysis of the Vaidyanathan wavelet that minimizes the aliasing effect (Figures 5 and 6) (Vaidyanathan and Hoang, 1988). Several wavelets have been tested with a synthetic signal and with a real 3–D seismic dataset. The best results were obtained with Vaidyanathan wavelet.

This study has illustrated how a discrete wavelet transform based multiresolution analysis makes possible separation of the information content of a non–stationary signal in different frequency ranges. This descomposition provides the seismic interpreter frequency information of interest that might not be visible in band-pass filters. This numerical study shows that several wavelets can be used with this technique, but it is important to select the appropriate wavelet, because a bad selection can give rise to spurious effects (i.e., artifacts) due to the overlay between scales, causing that the amplitude of the frequency content of some frequencies be enhanced, and the seismic interpreter can be mislead with these artifacts, and consider them subsoil information.

References

Bureau of Economic Geology, 1996, Boonsville 3-D Seismic Data Set, The University of Texas at Austin, pp. 39.

Hubbard B.B., 1998, The world according to wavelets: the story of a mathematical technique in the making, A. K. Peters Ltd., pp. 319.

Chui, Ch.K., 1992, An introduction to wavelets, Academic Press Limited, pp. 265.

Coconi-Morales E., Ronquillo-Jarillo G., Campos-Enriquez J.O., 2010, Multi-scale analysis of well-logging data in Petrophysical and Stratigraphic correlation. *Geofísica Internacional*, 49, 2, 55-67.

Daubechies I., 1992, Ten lectures on wavelets: SIAM, Capital City Press, pp. 377.

Dwight F. Mix, Kraig J. Olejniczak, 2003, Elements of wavelets for engineers and scientists, *Wiley-Interscience*, pp. 236.

Foster Douglas J., Lane F. David, Mosher Charles C., Wu Ru–Shan, 1997, Wavelet transforms for seismic data processing, SEG Technical Program Expanded Abstracts, pp. 1318 – 1321.

Misiti Michel, Misiti Yves, Oppenheim Georges, Jean-Michel Poggi, 1996, Wavelet Toolbox for use with MATLAB, Version 1, *The Mathworks Inc*., pp. 1–572.

Rivera-Recillas D.E., Lozada-Zumaeta M., Ronquillo-Jarillo G., Campos-Enriquez J.O., 2005, Multiresolution analysis applied to interpretation of seismic reflection data. *Geofisica Internacional*, 44, 4, 355-368.

Vaidyanathan P.P., Phuong–Quan Hoang, 1988, Lattice Structures for Optimal Design and Robust Implementation of Two–Channel Perfect Reconstruction QMF Bancks, IEEE transactions on Acoustics, Speech, and Signal Processing, 36, 1, 81–94.

Geofísica Internacional (2016) 55-3: 199-214

Original paper

Study of salt structures from gravity and seismic data in Santos Basin, Brazil

Renata Regina Constantino*, Eder Cassola Molina and Iata Anderson de Souza

Received: October 19, 2015; accepted: April 15, 2016; published on line: July 01, 2016

DOI: 10.19155/rgi20165531612

Resumen

El método sísmico es uno de los muchos usados para la identificación de estructuras y en estudios estratigráficos en cuencas sedimentarias. En la cuenca de Santos, numerosos estudios sísmicos han sido llevados a cabo con el propósito de obtener una mejor imagen de la sección geológica a profundidades más allá de la base de la capa de sal. En la literatura, se encuentran estudios de modelado de la corteza que hacen interpretación conjunta de datos sísmicos y de gravedad, sin embargo, hay pocos estudios que relacionan directamente anomalías de gravedad a estructuras de sal. Este trabajo busca asociar anomalías de gravedad con estructuras de sal interpretadas a partir de datos sísmicos y gravimétricos. Para los estudios encaminados a modelar la corteza a partir de datos de campo de gravedad de la corteza, se requiere el conocimiento de las dos mayores discontinuidades, basamento y Moho. Estas interfaces a menudo no son fáciles de ver mediante sísmica y por esto durante este estudio, ellas fueron encontradas por diferentes métodos envolviendo análisis de anomalías de gravedad. Las otras interfaces que involucran contrastes de densidad se analizaron mediante interpretación sísmica. Los resultados mostraron que las interpretaciones sísmicas y geológicas obtenidas podrían proporcionar información adicional al compararlas con los datos de anomalía de gravedad. En todos los perfiles modelados, alguna información geológica de la cuenca de Santos que no es visible en la sísmica, podría ser interpretada de acuerdo a el modelo geológico y al ajuste de las curvas de anomalía de gravedad. Como una conclusión final de este trabajo, es sugerido que el análisis combinado de los dos métodos geofísicos citados, puede proveer información importante acerca de la estructura de la corteza y ayudar en el modelado de la capa de sal.

Palabras clave: estructura de la corteza, capa de sal, interpretación sísmica, interpretación gravimétrica, Cuenca de Santos, Presal.

R. Regina Constantino
Institute of Astronomy
Geophysics and Atmospheric Sciences
University of São Paulo
Brazil
**Corresponding author: renata@iag.usp.br*

E. Cassola Molina
Institute of Astronomy
Geophysics and Atmospheric Sciences
University of São Paulo
Brazil

I. Anderson de Souza
UNESPetro
São Paulo State University
Brazil

Abstract

Seismic is one of the main methods used for the identification of structures and stratigraphic studies in sedimentary basins. In the Santos Basin, numerous 2D and 3D seismic surveys are being conducted in order to get a better image of the geological section to depths beyond the base of salt layer. Crustal modelling studies that make joint interpretation of seismic and gravity data are found in the literature, however there are few studies that relate gravity anomalies directly to salt structures. This work aims to associate gravity anomalies with salt structures from seismic and gravimetric interpretation. For studies aimed to model the crustal structure from gravity field data, the knowledge of two major discontinuities is required, the basement and the Moho. Such interfaces are often not easily seen by seismic and so, during this study, they were found by different methods involving analysis of gravity anomalies. The other interfaces involving density contrasts were analyzed based on seismic interpretation. The results showed that the obtained seismic geological interpretations may provide additional information when compared to gravity anomaly data. In all the modelled profiles, some geological information of the Santos Basin that are not visible in the seismic, could be interpreted according to the geological model and the adjustment of gravity anomaly curves. As a final conclusion of this work, it is suggested that the combined analysis of the two cited geophysical methods, can provide important information about the crustal structure and to assist in modelling the salt layer.

Key words: crustal structure, salt layer, seismic interpretation, gravity interpretation, Santos Basin, Pre-Salt.

Introduction

The Santos Basin is located in the southeastern region of the Brazilian continental margin, between 23°00'S e 28°00'S, and extends up to the bathymetric depth of 3.000 m (figure 1). It has about 350.000 km^2, covering the coastal states of Rio de Janeiro, São Paulo, Paraná and Santa Catarina (Moreira *et al*., 2007). The basin is bounded to the north by the Cabo Frio High and to the south by the Florianópolis lineament.

The formation of this basin is related to the opening of Supercontinent Gondwana, from the Lower Cretaceous (± 135 Ma), which resulted in the separation of South American and African continents. During the Neoaptian, the deposition of thick evaporite packages, generally composed of halite and anhydrite. This evaporite sequence was deposited due to the high rate of thermal subsidence in the Santos Basin, coupled with a gradual water intake isolated sea by proto-Gulf South (Gamboa *et al*., 2008).

In the Upper Cretaceous (Santonian-Campanian), due to reactivation of old faults of the basement, there was an uplift in the continental area, causing a remarkable siliciclastic erosion and progradation of clastic wedges into the basin, that was in subsidence process in the same period (Macedo, 1987 and 1989; Almeida and Carneiro, 1998). This siliciclastic progradation during this period, was responsible for the deformation of the evaporite packages and for moving these packages into the depocenter of the basin, providing a thick layer in the region known as Plateau of São Paulo, where the seismic investigations show remarkable presence of halokinetic structures, such as diapirs and salt walls.

The evaporite packages in the Santos Basin show interleaves with halite domain and a few layers of anhydrite. Both have constant seismic velocity with burial and thus, the seismic amplitude contrast between layers of these salts and adjacent sediments depends only on their the acoustic properties. On the other hand, the density contrast of sediments may vary with depth (Jackson & Talbot, 1986). The halite has a high seismic speed but a low density, around 2.17 g / cm3. The anhydrite has a high speed and a high density value, of approximately 2.98 g / cm3 (Bassiouni, 1994). Due to these differences of density, interpreting seismic data set using the gravity anomaly data can be a good solution to identify these different types of salt, modelling more precisely the evaporite packages and the adjacent sedimentary packages.

Previous studies as Mio (2005) and Lima & Mohriak (2013), show modelled crustal structures in the region of the Santos Basin from seismic data and gravity data, originating geological models for the studied regions. These works ~~focuses~~ primarily on modelling the seismic data and subsequently obtaining

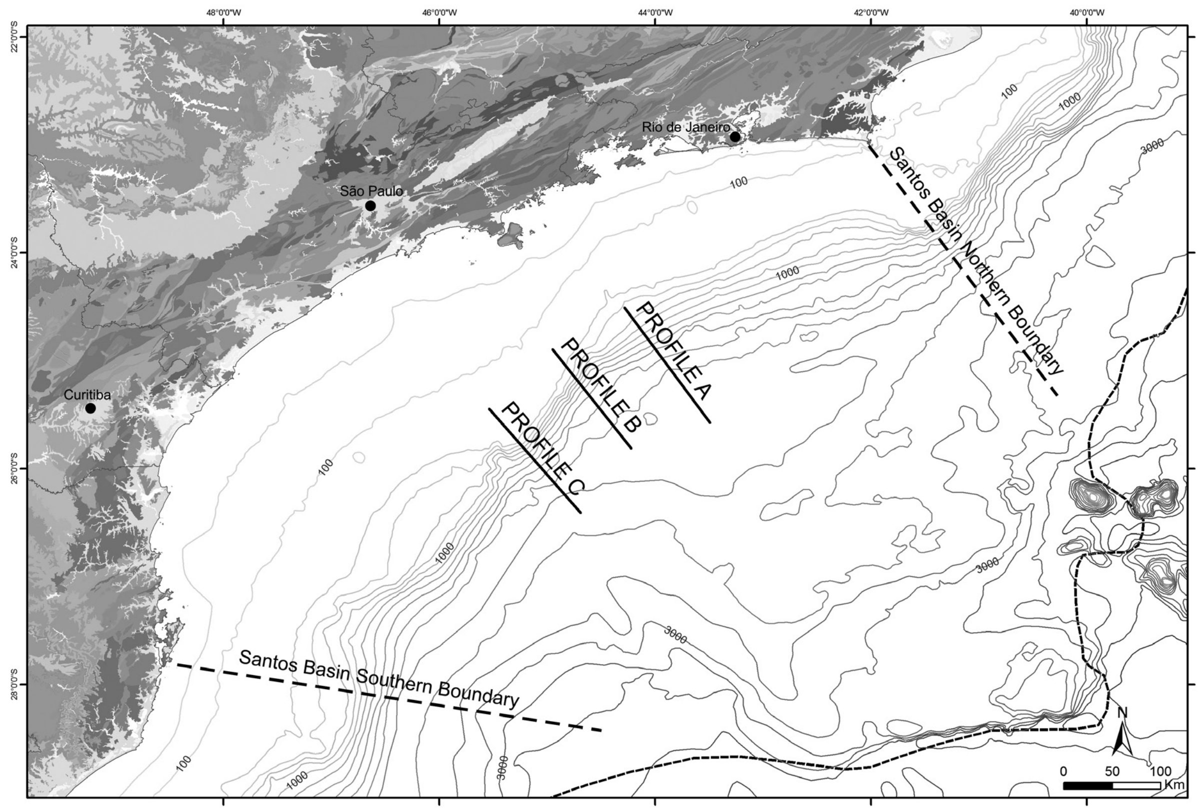

Figure 1. Location of Santos Basin. The continent-ocean boundary, according to Cainelli and Moriak (1999) is represented by the dashed line and bathymetric isolines are represented by blue the blue lines. The studied profiles A,B and C are also shown.

the adjustment together with the gravity data. In 2D seismic data, the top basement surface, due to the low resolution of the data at depth, is performed with less precision than shallower and more defined surfaces, such as the top and the base of the salt. In the case of the Moho, most of the time the horizon cannot even be interpreted with 2D seismic data. Thus, two horizons that separate packages with high density contrast are modelled by approximation and the effect of this inaccuracy may be impacting the final geological model. In this study, the focus will be to elaborate geological models and to calculate the gravity anomaly associated with each of the proposed geological models. Two different models are elaborated for each chosen profile, one considering the salt layer and the other not, both using the Moho and the basement horizon obtained by gravimetric inversion. The gravimetric signal generated by the created models and the residual anomaly are analyzed in order to find a relationship between the residual anomaly and the salt layer.

The main objective of this study is to find residual gravity anomalies related to salt with a method that is independent of seismics. Such data will only be used to validate the model. The specific objectives are to determine the depth of the Moho and basement interface from gravity inversion and, to identify possible anhydrite in layers of salt in the Santos Basin.

The methodology can be hereafter applied to suggest possible locations of salt reservoirs from gravimetric data, facilitating and reducing costs of oil exploration.

Methodology

The structure of the method is divided into two steps:

Step 1: Gravimetric inversion

In this step the depth of Moho and basement interfaces from gravity inversion is found.

The free-air anomaly data set (Molina, 2009) is corrected to obtain the Bouguer anomaly. The gravity field thus obtained is then adjusted to remove the effect of the sedimentary cover. The gravity effect of the sedimentary cover can be calculated by Parker algorithm (Parker, 1972), which makes use of a series expansion up to order 5 of the gravity field generated by an oscillating boundary. The calculation can be done with a constant density contrast along the discontinuity; however, to obtain more realistic results, the sediment compaction with depth should be considered. For taking this into account, in this study we use a compaction model described by Sclater & Christie (1980), based on an exponential reduction of the porosity with depth. According to these authors, the density in dependence of depth below the ocean floor (z) is calculated from the exponential compaction described below:

$$\rho(z) = \rho_f \varphi_0 e^{-\frac{z}{d}} + \rho_g(1 - \varphi_0 e^{-\frac{z}{d}}) \qquad (1)$$

where:

ρ_f = Fluid density

ρ_g = Rock/grain density

φ_0 = Initial porosity of sediments

d = Decay parameter

The gravity effect of sediments is calculated by applying this model to a series of thin layers (10 m thick) with lateral variable density, described by equation (1).

The values of density, porosity and decay parameter are calibrated from well data information and the fluid density is a standard value of 1030 kg/m³. After calculating the gravity effect of the sedimentary cover, the residual field (resulting from subtracting the gravitational effect of the sediments from the Bouguer anomaly) is inverted by applying the iterative constrained inverse modelling, proposed by Braitenberg & Zadro (1999) and applied later in continental and oceanic areas (e.g. Braitenberg and Ebbing, 2009; Mariani *et al*., 2013) and the Moho interface is then obtained.

To find out the basement topography, the gravity effect of the Moho is calculated using a constant density contrast along the Moho interface by applying the Parker algorithm (Parker, 1972). The objective of this procedure is to isolate the gravity effect of the sediments and the Moho from the of the observed gravity anomaly:

$$g_{res} = g_{obs} - g_{MOHO} - g_{sed} \qquad (2)$$

The obtained residual field (g_{res}) is inverted by applying the iterative constrained inverse modelling. The procedure results in the basement topography.

Iterative Constrained Inverse Modelling

The methodology proposed by Braitenberg & Zadro (1999) is an iterative solution that alternates the downward continuation law with the direct calculation of the gravity field of the model.

Considering $g_0(x, y)$ as the Bouguer anomaly, d the reference depth and r(x, y) the boundary oscillation, defined as the deviations from the depth d, and being $g_d(x, y)$ the downward continued field for depth d, taking the Fourier transform of the gravity field, one obtains

$$g_d(k_x, k_y) = e^{d\gamma} g_0(k_x, k_y) \qquad (3)$$
$$Y = \sqrt{k_x^2 + k_y^2}$$

where k_x, k_y are the wave numbers along the coordinate axis

Assuming that the gravity field is generated by a sheet mass located at a depth d, the surface mass density of the sheet mass σ (x, y) is given by:

$$\sigma(x,y) = \frac{1}{2\Pi G} g_d(x,y)$$

$$= \frac{1}{2\Pi G} FT^{-1} \; gd(k_x, k_y) \qquad (4)$$

where FT^{-1} is the inverse Fourier transform and G the gravitational constant.

The sheet mass with superficial density horizontally variable is interpreted as the oscillating interface separating two layers with a density contrast $\Delta\rho$. The amplitude of the interface oscillation is given by:

$$r_1(x,y) = \frac{1}{\rho}\sigma(x,y) \qquad (5)$$

It should be noted that the gravity field generated by the interface coincides with the field $g_0(x, y)$ only to a first approximation. In this method an approximation of the interface is done through a series of rectangular prisms and the gravity field is calculated by applying the algorithm described by Nagy (1966). The gravity residual field $\delta g_1(x, y)$ is defined as the difference between the observed field ($g_0(x, y)$) and the field ($g_1(x, y)$) generated by a series of prisms

$$\delta g_1(x,y) = g_0(x,y) - g_1(x,y) \qquad (6)$$

The residual field is continued downward and the correction introduced in the density surface of the sheet mass is obtained by the Eq. 5. The corrections affect the oscillation amplitude of the density interface according to Eq.6. The procedure is repeated iteratively, obtaining at each new iteration (k) the residual gravity field $\delta g_k(x, y)$ and the oscillation amplitude of the interface $r_k(x, y)$.

Step 2 - Forward Modelling

In this step, two-dimensional forward models of the crust are created, and the gravity response for each model is calculated based on Talwani *et al*. (1959) and compared to the observed anomaly. For each studied profile (figure 1), the following models were created:

Model 1: the first model is created with only the horizons obtained by gravimetric inversion. It will have the main discontinuities: mantle, crust and sediments. Due to the absence of the salt package, a high residual anomaly (calculated - observed) is expected.

Model 2: to investigate if the residual anomaly obtained in the previous model is associated or not to the salt package, a forward model is developed, considering, from seismic interpretation, only the salt package. The gravity response regarding the created model is then compared with the residual anomaly obtained in the previous model. If the error between the two anomalies can be considered low, one assumes that the residual anomaly is directly linked to the salt package. If the error is considered high, a new model to map the source of the error must be created.

Results

Step 1 - Gravimetric inversion

The Bouguer anomaly contains the sum of the gravimetric effects of different sources (Weidmann *et al*., 2013). The first procedure of this step aims to correct the Bouguer gravity field to the effect of the sedimentary cover. For this calculation, values of the sediment thickness (figure 2), initial porosity taken from the Deep Sea Drilling Project leg 39, site 356 (Supko *et al*. 1997), density and decay parameter were used. To choose these parameters, several tests were made with different values. For each result obtained with the Sclater & Christie (1980) model, a comparison was made with well data provided by the National Agency of Petroleum (ANP). The best fit was found for a density value of 2.6 g / cm3 and a 0.00078 decay pattern.

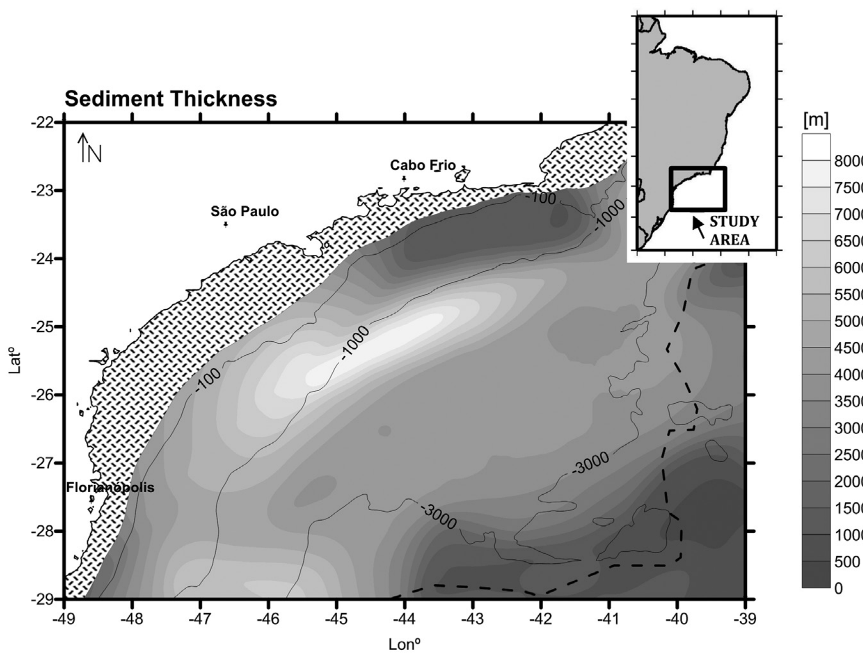

Figure 2. Sediment Thickness. The continent-ocean boundary, according to Cainelli and Moriak (1999), is represented by the dashed line and the bathymetric isolines for water depths 100, 1,000 and 3,000 m are shown. The hatched area next to the coast represents an area where the data are not reliable.

The sediments contribute with a non negligible amount to the gravity signal and then, to obtain the Moho depth, the contribution of the sediments is subtracted from the Bouguer anomaly (figure 3). The sediment corrected Bouguer anomaly is displayed in figure 4 and it will be used in the inversion process. According to Blakely (1995), the long wavelength part of the observed gravity field is generated by CMI undulations and the short-wavelength part is due to the superficial masses. For this study, the cut-off wavelength is estimated from the decay of the amplitude spectrum of the gravity field (Russo & Speed, 1994), found as 120 km. The gravity field was inverted for a laterally variable density contrast, taken from the CRUST 2.0 model (Bassin *et al*., 2000).

In addition to the cut-off wavelength and the density contrast, a reference depth value had to be assumed, and for that, several tests were performed changing the reference depth within 20 km - 35 km. For each result, the Root Mean Square Error (RMS) in relation to Moho depth values from Zalán *et al*. (2011) was calculated. The best RMS (0.9 km) was found for a reference depth of 31 km. The calculated Moho is shown on figure 5.

Found the Moho depth, its gravity effect was calculated by Parker algorithm (Parker, 1972) for a constant density contrast along the interface. This effect and the gravity effect of the sediments were subtracted from the observed gravity anomaly, resulting in a residual field which is associated with the basement.

For the inversion of this residual field, a constant density contrast of 1,640 kg/m^3 was used, related to the density contrast between the upper crust and the water. All wavelengths are taken into account and the reference depth was defined as the zero level (Hwang, 1999). By "basement" in this study we refer to the physical surface that lies below the sediment layer. The sediment thickness data used in this study represents the depth of the acoustic basement, defined, according to Constantino & Molina (2014), as the deepest observable reflector in the seismic reflection profiles, and may not necessarily represent the base of the sediments. Furthermore the sediment isopachs are relatively smooth with respect to the gravity signal which is used to find the details of the top basement. The result of the present study work provides the base of the sediments and the results are shown on figure 6. The values amount to 10,500 m at the central portion of the basin, near the bathymetric level of 1,000 m, coinciding with the high sediment thickness values (figure 2).

Step 2 - Forward modelling

During step 2, three profiles in the Santos Basin were modelled in order to obtain the geological information and the values of the gravity field. *Model 1* was built only with the horizons obtained by gravimetric inversion, where three sedimentary layers were considered: mantle, crust and sediments (figure 7).

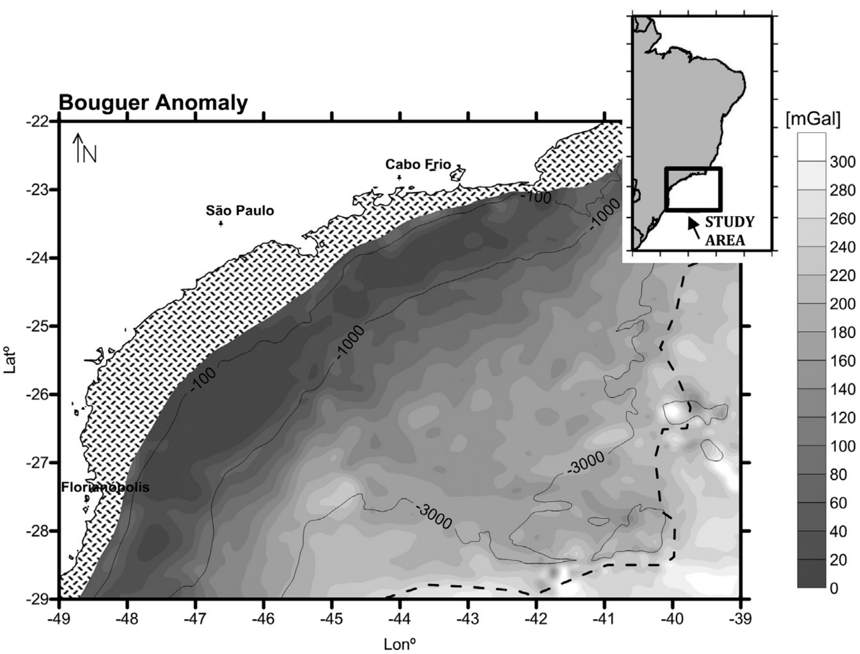

Figure 3. Bouguer anomaly from Molina (2009). The continent-ocean boundary, according to Cainelli and Moriak (1999), is represented by the dashed line and the bathymetric isolines for water depths 100, 1,000 and 3,000 m are shown. The hatched area next to the coast represents an area where the data are not reliable.

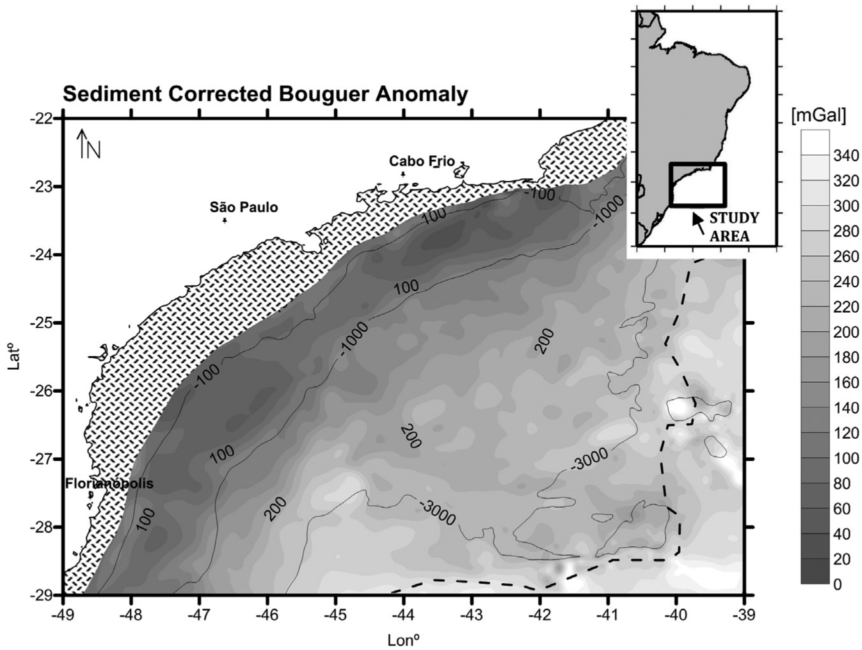

Figure 4. Sediment correct bouguer anomaly. The continent-ocean boundary, according to Cainelli and Moriak (1999), is represented by the dashed line and the bathymetric isolines for water depths 100, 1,000 and 3,000 m are shown. The hatched area next to the coast represents an area where the data are not reliable.

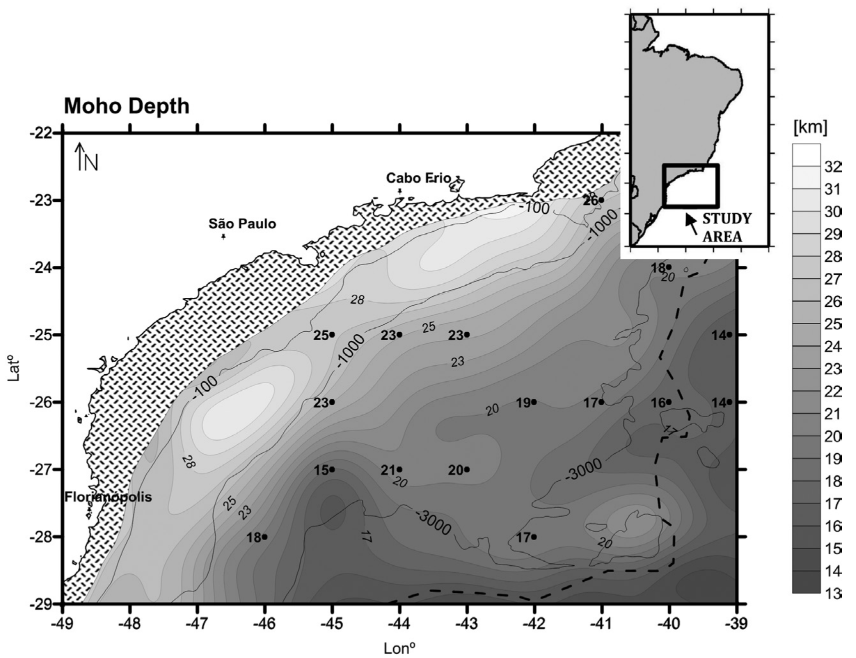

Figure 5. Moho Interface map obtained from inversion of the gravity field. Values marked in black are constraining data from Zalán *et al*., (2011). Isolines for Moho depths of 17 km, 20 km, 23 km, 25 km and 28 km are set to reference level. The continent-ocean boundary, according to Cainelli and Moriak (1999), is represented by the dashed line and the bathymetric isolines for water depths 100, 1,000 and 3,000 m are shown. The hatched area next to the coast represents an area where the data are not reliable.

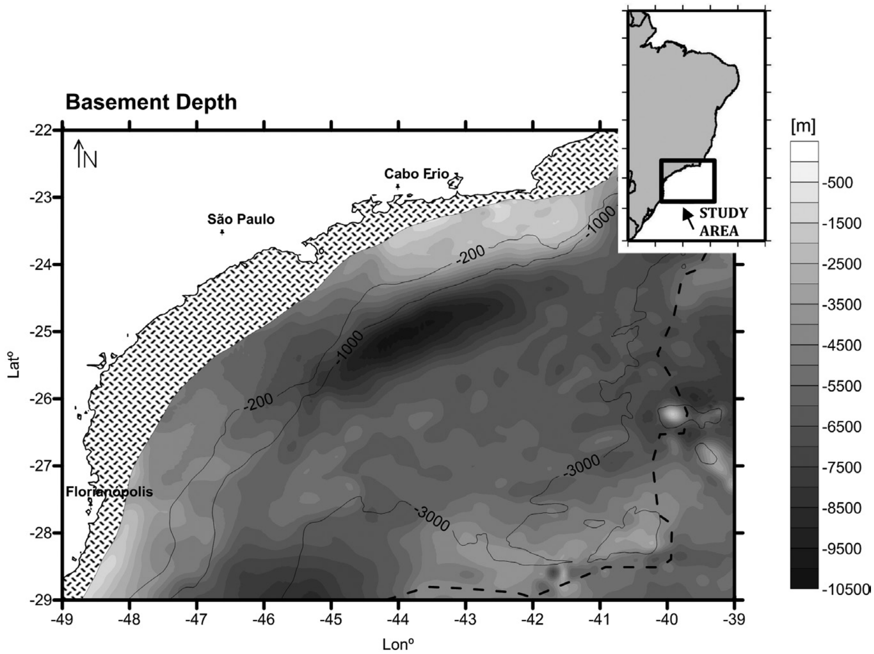

Figure 6. Basement Depth. The continent-ocean boundary, according to Cainelli and Moriak (1999), is represented by the dashed line and the bathymetric isolines for water depths 100, 1,000 and 3,000 m are shown. The hatched area next to the coast represents an area where the data are not reliable.

The density values used for the three profiles are average values, being 2.45 g/cm^3 for the sediment layer, 2.67 g/cm^3 for the crust and 3.4 g/cm^3 for the mantle (Mio, 2005; Gamboa *et al*. 2008). The gravimetric response of the elaborate models when compared to the observed anomaly shows RMS error values considered high, being 8.483 mGal for profile A, 12,757 mGal for profile B and 13.02 mGal for the profile C (figure 7).These results were expected, whereas the salt package present in the region was not considered in the interpretation.

Model 2, developed only for the salt package in contrast with the sediments is shown in figure 8. The observed gravity anomaly in this case is the residual anomaly obtained in the previous model (figure 8). The salt thickness was obtained from seismic interpretation and It has an uncertainty on the order of one hundred meters. The time-depth conversion was calculated using the classic methodology (Dobrin, 1976; Dobrin & Savit, 1988) with velocities of 1.500 m/s, 2.500 m/s and 4.000 m/s for the ocean bottom, sediments and salt, respectively.

Analyzing profile A, the interpreted salt package can be observed. As the prevalence is halite a density of 2.17 g/cm^3 was used. A portion of stratified salt, previously interpreted by other authors such as Cobbold *et al*. (2005), Mohriak & Stazamari (2012) and Mohriak *et al*. (2015) is also interpreted in the model. The adjustment of the observed and calculated curves in this case is satisfactory, with an RMS error of 0.96 mGal. However, in addition to the salt package, a dense body had to be added to the model.

In profile B, the presence of a dense body was also necessary and the adjustment of anomalies appear satisfactory, with an error of 1.98 mGal. The package of salt, with an average density of 2.17 g/cm^3, shows a salt diapir well placed on the proximal part of the profile and a salt wall on the distal part of the profile. No evidence of stratified salt was found during the seismic and gravimetric interpretation.

The last profile also showed the presence of a dense body and a thick layer of salt, with evidences of stratified salt. The adjustment of the curves was satisfactory, with an RMS error of 1.14 mGal.

During the interpretation, the presence of anhydrite was not considered Despite having a high density compared to other sediments (2.98 g/cm^3), the anhydrite when present in the salt package, appears intercalated with halite,

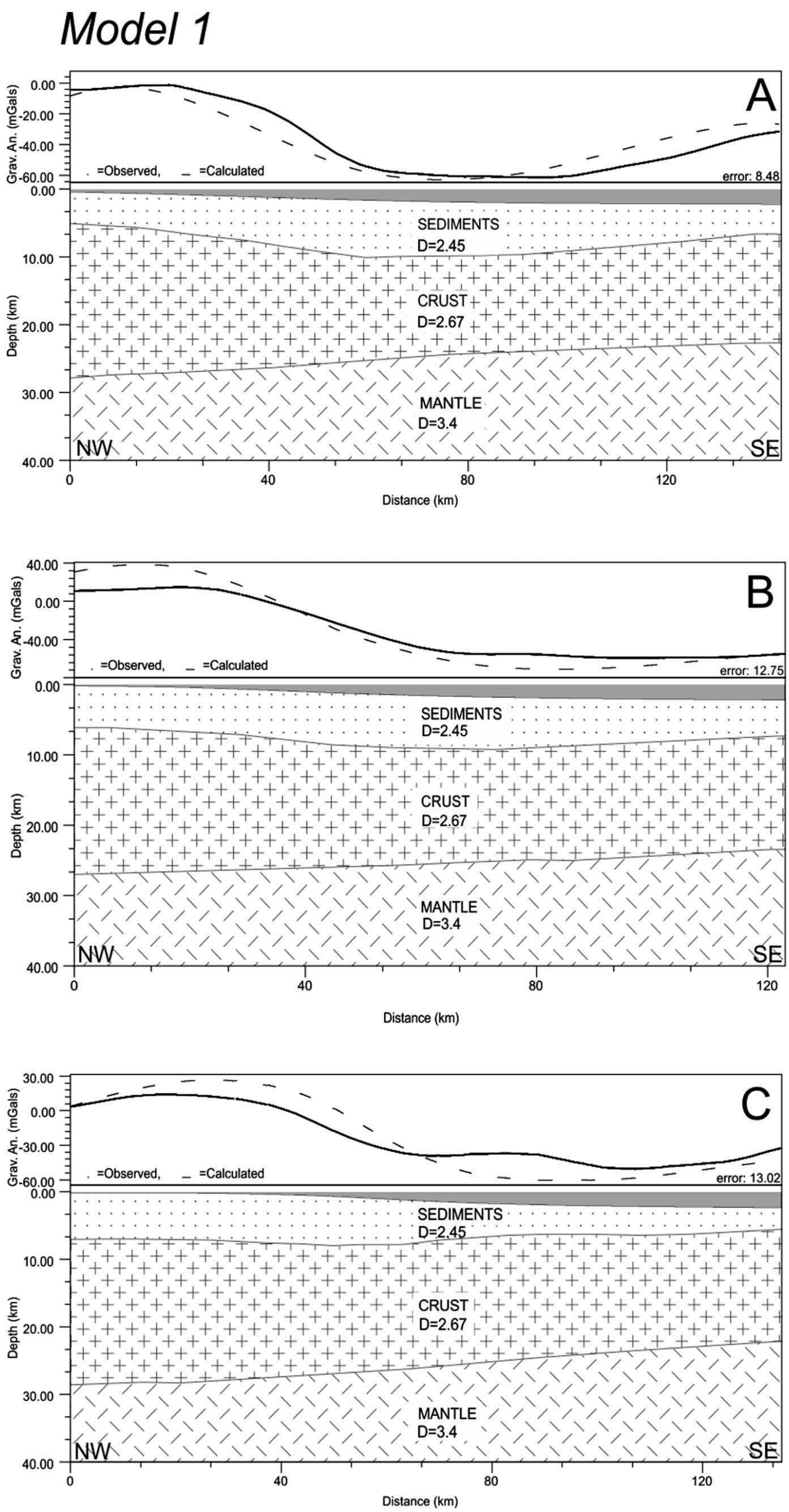

Figure 7. *Model 1* - Two dimensional forward gravity model for the profiles shown in figure 1.

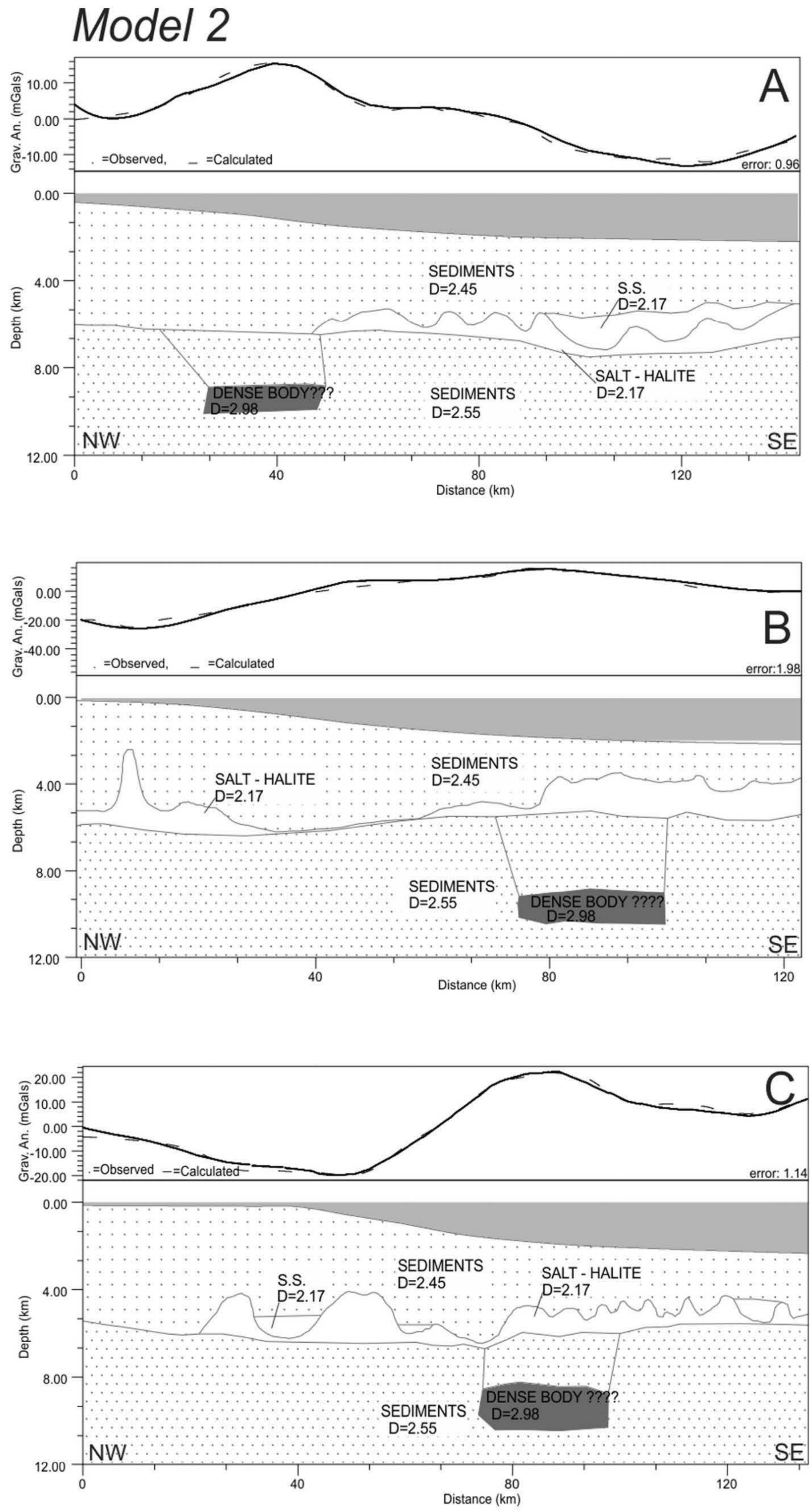

Figure 8. *Model* 2- Two dimensional forward gravity model for the profiles shown in figure 1.

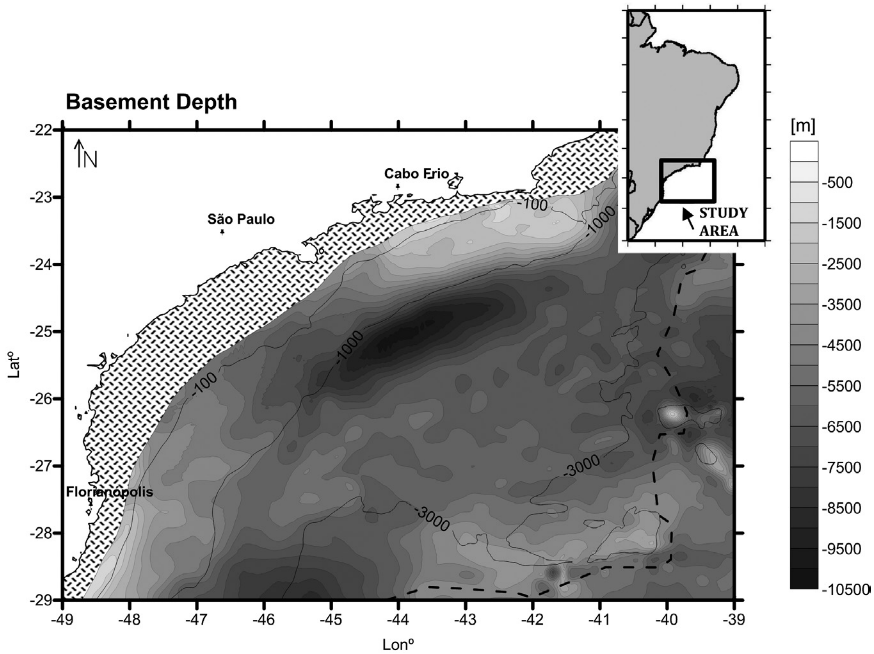

Figure 9. Bathymetric map from GEBCO. The continent-ocean boundary, according to Cainelli and Moriak (1999), is represented by the dashed line and the bathymetric isolines for water depths 100, 1,000 and 3,000 m are shown. The hatched area next to the coast represents an area where the data are not reliable.

in thicknesses that usually do not exceed 30 m, not generating a considerable response in gravity anomaly.

Discussion

Step 1 - Gravimetric inversion

The Moho values obtained by gravimetric inversion when compared to Moho values from Zalán *et al*. (2011) showed a RMS error of only 0.9 km. Furthermore, our model seems to be in agreement with other crust models proposed before such as by Zálan *et al*. (2011), Mohriak (2014) and Rigoti (2015), where they presented a very similar Moho high next to the continent-ocean transition. In the model, it is possible to see a “tongue” structure between 44-46W. This same structure is discussed by Rigoti (op. cit.) as a grabbroic proto-oceanic crust or a serpentinized mantle.

A good model of the Moho is of great importance in many geophysical and geological studies, but specially in this case, it is essential. The crust to mantle transition has the high density contrast in the Earth´s upper layers, and any small changes in its depth can result in a high value of the gravity anomaly.

There are lots of studies found in the literature that make joint models of seismic and gravimetric data, but with a poor approximation of the Moho, which could result in a wrong adjustment of the observed and calculated gravity anomalies. The same happens with the basement. Because of the salt layer in Santos basin, it is very difficult to interpret what is above this layer from seismic data, and usually the basement is also an approximation. In this study, in this study, a special care has been taken with these two discontinuities, making sure that they were well delimited using the best data available for the study.

The basement structure of the Santos Basin is calculated at this last step. This is done by the inversion of the residual gravity field (g_{res}) found in step 3, using the Iterative Gravity Inversion model (Braitenberg and Zadro, 1999). The results of this study show that some basement features, that could be determined from the available data following the methodology proposed by Braitenberg *et al*. (2006), are hidden by the sedimentary layer in the region of the Santos Basin.

The depth of the basement so calculated reaches 10,500 meters. Comparing to the bathymetric data (figure 9), this depth shows

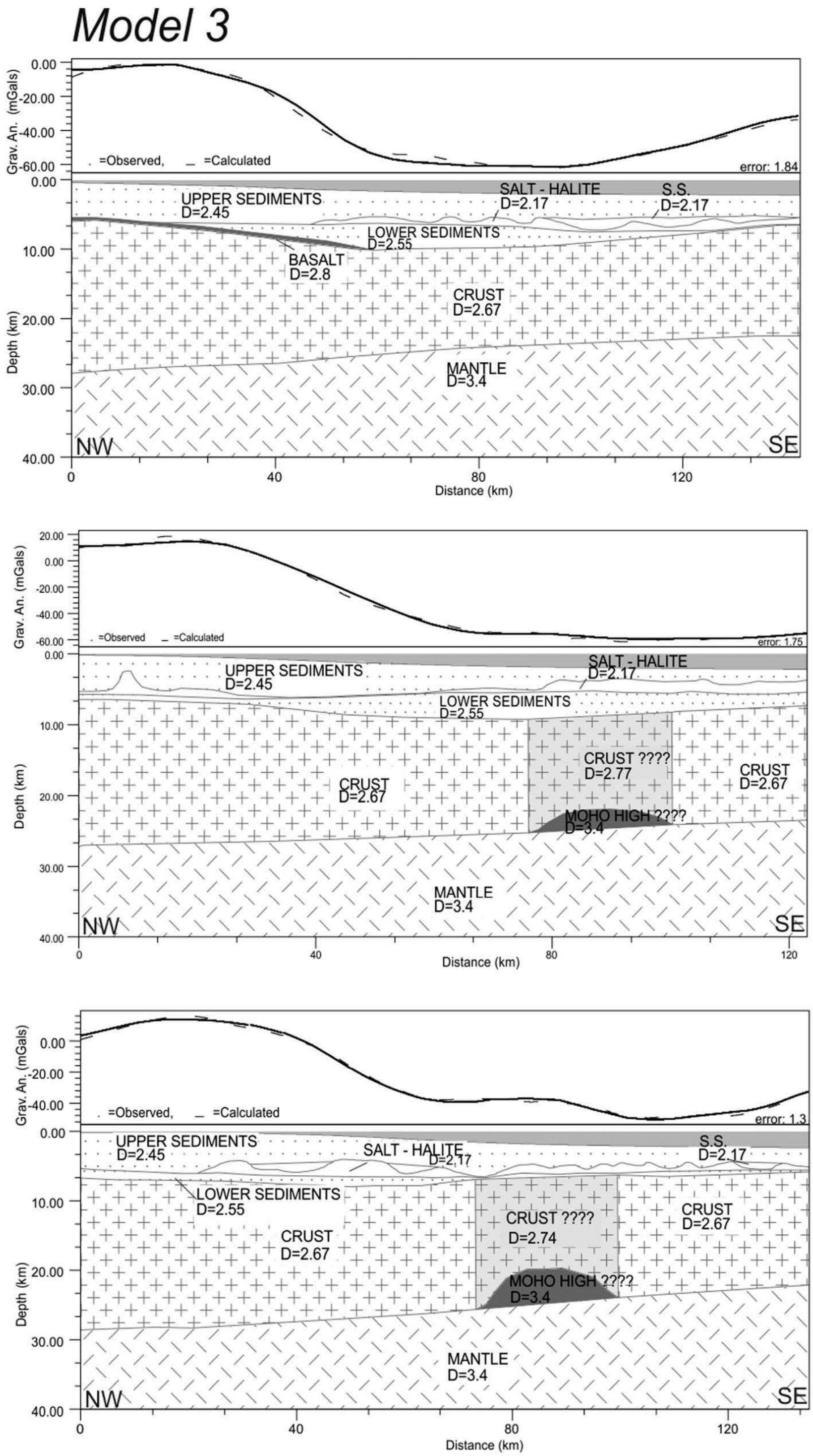

Figure 10. *Model 3* - Two dimensional forward gravity model for the profiles shown in figure 1.

greater values and it is possible to observe salient features that are not present in the bathymetric model. This can be due to the sedimentary cover that conceals some tectonic features of the basement.

Step 2 - Forward modelling

In this study, the initial hypothesis was that the residual anomaly obtained in the *Model 1* (figure 7) is linked to the salt package in the Santos Basin region. To confirm this hypothesis, the interpretation of the salt with this residual anomaly and the adjustment of the observed (in this case, the residual) and calculated curves was analyzed.

For profiles A and C, a layer of stratified salt was interpreted. According to Gamboa *et al*. (2008), the stratified salt consists of interbedded salt, such as anhydrite, halite and complex salts, deposited in shallow waters inside mini basins. Even with the possible presence of anhydrite and complex salts with higher densities than halite in the stratified salt package, we used the average density value for halite, 2.17 g/cm^3, and the results can be explained by two arguments: the first one is the good adjustment of the observed and the calculated gravimetric anomalies, and the second one is due to the gravimetric method that is unable to discern this type of horizontal stratification within a larger sedimentary package.

For the three studied profiles, the presence of a dense body was pointed out and the curves were adjusted satisfactorily. To analyze it, another model was prepared *(Model 3)*, this time with all the information presented in the results: mantle, crust, lower sediments, salt package and upper sediments (figure 10).

In profile A (figure 10), the suggested dense body can be explained by a seaward-dipping reflector (SDR), which represents flood basalts rapidly extruded during the rifting or seafloor spreading. According to Jackson *et al*. (2000), SDRs can be present but seismically obscured bellow salt basins. After interpreting the dense body as a flood basalt, with a density of 2.8 g/cm^3, the observed anomaly, when compared to the calculated anomaly, shows an error of 0.96 mGal, which can be considered very small.

To adjust the observed and the calculated anomalies of profiles B and C (figure 10), two possible interpretations were made. The first one is a laterally density variation into the crust. For all modeled profiles, a constant density of 2.67 g/cm^3 was used for the crust, because there were not enough information to assume neither a lateral density variation nor a depth variation in the lower and upper crust.

Where a dense body is modeled in both profiles B and C, the anomalies can be fitted dividing the crust vertically and changing densities from 2.67 to for 2.74 and 2.77 respectively (figure 10).

Another possible interpretation could be a Moho high, marked in dark gray on profiles B and C (figure 10). Some authors, such as Gomes *et al*. (2009), Zálan *et al*., (2011), Kumar *et al*. 2012 and Mohriak, (2014) show the presence of a Moho high in the Santos Basin, discussed in their articles as a piece of exhumed mantle. A possible explanation for the exhumed mantle would be due to the lithospheric stretching associated with crustal thinning and mantle exhumation by detachment faults. According to Zálan *et al*. (2011), the exhumed mantle occurs in the continental-oceanic crustal transition and can be mapped continuously from the Santos to the Espírito Santo basins. As can be observed in figure 1, the lines are far away from the continental-oceanic crustal transition, and therefore the Moho high interpreted in our data cannot be explained by the exhumed mantle. In this case, as the Moho model is a smooth surface, this high could be explained by a feature that cannot be detected by the methodologies used in this work.

Conclusions

The Moho depth obtained from the inversion of the corrected gravity field was satisfactory and presented an RMS error of approximately 0.9 km between the values of the obtained model and constraining data from Zalán *et al*. (2011). The basement depth, also found from gravity inversion, could not be constrained due to the absence of previous works in the studied region. Nevertheless, during the forward modelling where the observed and calculated anomalies were compared, the use of the basement and the Moho depth resulted in a good adjustment of the gravity anomaly curves, which confirms the validity of the basement depth model.

The first forward model (*Model 1*), using information from the mantle, the crust and the sediments delimited by the Moho and the basement obtained by gravity inversion, showed high RMS values between the observed and calculated anomalies for all the 3 analyzed profiles. This was expected because the salt package was not considered during this first interpretation. Moreover, the main goal of this study is to associate the residual anomaly to the salt package present in the region, and the poor obtained adjustment may reflect this situation, as the salt package represents a high density contrast body that was not considered in this interpretation.

When the residual anomaly obtained from *Model 1* is adjusted considering the presence of the salt package inferred from seismic data (*Model 2*), the errors between the observed and the calculated anomaly still remain high, and a body with high density should be added to the model in order to obtain a reasonable fit. This body could not be observed in the seismic data, probably because below the salt layer the seismic reflectors barely can be detected. Additionally, the presence of anhydrite was not considered in the model. It might appear intercalated with halite and the gravimetric method is unable to discern this type of horizontal stratification within a larger sedimentary package.

One last model (*Model 3*) was built with all the information obtained during this study: the upper sediments, the salt package, the lower sediments, the basement, the crust, the Moho and the mantle. The error so obtained is very low for all the 3 studied profiles. The salt package could not account for all the residual anomaly, and a possible basalt intrusion or a Moho high were suggested to explain the dense body proposed in *Model 2.*

As a final conclusion of this work, it is shown that the combined analysis of the two used geophysical methods can provide important information about the crustal structure and to assist in modelling the salt layer. For a future study, it would be interesting to work with an inversion method and apply it to the residual gravity anomaly. If this anomaly could be free of influences such as the basalt intrusion and the Moho high presented in this study, the inversion of the residual anomaly could be directly associated to the salt package. This could bring a new methodology where the gravity data may play a major role associated with seismic data to characterize structures containing salt packages, which could be of great interest for pre-salt studies and oil exploration.

References

Almeida F.F.M., Carneiro C.D.R., 1998, A origem e evolução da Serra do Mar. *Revista Brasileira de Geociências*, Brasília, 28, 2, p.135-150, 1998.

Bassiouni Z., 1994, Theory, Measurement, and Interpretation of Well Logs; SPE Textbook Series Vol. 4: Society of Petroleum Engineers,Richardson, Texas, Capítulo VIII, p: 159-171.

Bassin C, Laske G., Masters G., 2000, The Current Limits of Resolution for Surface Wave Tomography in North America, EOS Trans AGU, 81, F897.

Blakely R.J., 1995, Potential Theory in Gravity and Magnetic Applications, Cambridge Univ. Press, 441 p.

Braitenberg C., Zadro M., 1999, Iterative 3D gravity inversion with integration of seismologic data, *Bollettino Di Geofisica Teorica ed Applicata*, 40, 3-4, p. 469-475.

Braitenberg C., Wienecke S., Wang Y., 2006, Basement structures from satellite-derived gravity field: South China Sea ridge, *J. Geophysical Res.*, 111, B05407, doi:10.1029/2005JB003938.

Braitenberg C., Ebbing J., 2009, New insights into the basement structure of the west-Siberian basin from forward and inverse modelling of Grace satellite gravity data,. *J. Geophysical Res.*, 114, B06402, doi:10.1029/2008JB005799.

Cainelli C., Mohriak W.U., 1999, Some remarks on the evolution of sedimentary basins along the Eastern Brazilian continental margin. *Episodes*, 22, 3, 206 – 216 p.

Cobbold P.R., Szatamari P., Demercian L.S., Coelho D., Rossello E.A., 1995, Seismic experimental evidence for thin-skinned horizontal shortening by convergent radial gliding on evaporites, deep-water Santos Basin. In: JACKSON, M. P. A., ROBERTS, D. G. & SNELSON, S. (eds) Salt tectonics: a global perspective. *American Association of Petroleum Geologists Memoirs*, 65, 305–321.

Constantino R., Molina E.C., 2014, Basement Structure of the Santos Basin from Gravity Data, Gravity, Geoid and Height Systems, *International Association of Geodesy Symposia*, 141, DOI 10.1007/978-3-319-10837-7_1, v.141, p. 319-328

Dobrin M.B ., 1976, Introduction to geophysical prospecting (3d ed.) : New York, McGraw-Hill, 619 p.

Dobrin M.B., Savit C.H., 1988, Introduction to geophysical prospecting: 4th edition: McGraw-Hill Book Co., 867p.

Gamboa L.A.P., Machado M.A.P., da Silveira D.P., de Freitas J.T.R., da Silva S.R.P., 2008, Evaporitos estratificados no Atlântico Sul, in W.U. Mohriak, P. Szatmariand S.M. Couto Anjos, eds., *Sal: Geologia e Tectônica,* Ediçoes Beca, Petrobras, Sao Paulo, p. 340-359.

Gomes P.O., Kilsdonk B., Minken J., Grow T., Barragan R., 2009, The outer high of the Santos Basin, Southern São Paulo Plateau, Brazil: pre-salt exploration outbreak, Paleogeographic setting, and evolution of the syn-rift structures. In: AAPG International Conference and Exhibition, 15–18 November 2009, Rio de Janeiro, Brazil. *AAPG*, Search and Discovery Article #10193. World Wide Web Address: http://www.searchanddiscovery.net/documents/2009/10193gomes/index.htm

Hwang C., 1999, A bathymetric model for the South China Sea from Satellite altimetry and depth data, *Mar. Geod*., 22,37-51.

Jackson M.P.A., Talbot C.J., 1986, External shapes, strain rates, and dynamics of salt structures. *Geol. Sot. Am. Bull*., 97, 305-325.

Jackson M.P.A., Cramez C., Fonck J-M., 2000, Role of subaerial volcanic rocks and mantle plumes in creation of South Atlantic margins: implications for salt tectonics and source rocks. *Marine and Petroleum Geology*, 17, 427–498.

Kumar N., Danforth P., Nuttall J. Helwig D.E. Bird S., 2012, Venkatraman From oceanic crust to exhumed mantle: a 40 year (1970–2010) perspective on the nature of crust under the Santos Basin, SE Brazil W.U. Mohriak, A. Danforth, P.J. Post, D.E. Brown, G.C. Tari, M. Nemcok, S.T. Sinha (Eds.), *Geol. Soc*. (Lond.) Spec. Publ., 369.

Lima J.V., Mohriak W., 2013, Análise Regional e Geológica das Estruturas Profundas na Bacia de Santos in 13th International Congress of the Brazilian Geophysical Society, Rio de Janeiro, Brazil

Macedo J.M.,1987, Evolução estrutural da Bacia de Santos e áreas continentais adjacentes. 1987. 173f. Dissertação (Mestrado em Geociências) – Departamento de Geologia, Universidade Federal de Ouro Preto, Ouro Preto.

Mariani P., Braitenberg C., Ussami N., 2013, Explaining the thick crust in Parana' basin, Brazil, with satellite GOCE-gravity observations. *Journal of South American Earth Sciences*, 45, p. 209-223, doi:10.1016/j.jsames.2013.03.008

Mio E.,2005, Modelagem crustal da Bacia de Santos pela integração de métodos geofísicos. Dissertação de Mestrado, Universidade Estadual Paulista, Rio Claro. 94 p.

Mohriak W., 2014, Birth and Development of Continental Margin Basins: Analogies from the South Atlantic, North Atlantic, and the Red Sea. In 2013-2014 AAPG Foundation Distinguished Lecture, Search and Discovery Article #41502. World Wide WebAddress: http://www.searchanddiscovery.com/documents/2014/41502mohriak/ndx_mohriak

Mohriak W., Newcok M., Enciso G., 2015, South Atlantic divergent margin evolution: rift-border uplift and salt tectonics in the basins of SE Brazil Geological Society, London, *Special Publications*, 2008, 294, p. 365-398 doi: 10.1144/SP294.19

Mohriak W., Szatmari P., Anjos S., 2012, Salt: geology and tectonics of selected Brazilian basins in their global context, Geological Society, London, *Special Publications*, 2012, 363, p131-158, doi: 10.1144/SP363.7

Molina E.C., 2009, O uso de dados de missões geodésicas de altimetria por satélite e gravimetria marinha para a representação dos elementos do campo de gravidade terrestre. Tese de livre docência. Departamento de Geofísica do IAG-USP. Universidade de São Paulo. 100 p.

Moreira J.L.P., Madeira C.V., Gil J.A., Machado M.A.P, 2007, Bacia de Santos, *Boletim de Geociências da Petrobrás*, 15, 2, 531-549.

Parker R.L., 1972, The rapid calculation of potential anomalies. Geophys. J. R. Astr. Soc., 31, p. 447-455.

Rigoti C., Valeriano C., Viana A., 2015, Evolução Tectônica da Bacia de Santos com ênfase na geometria crustal. In: IX International Symposium on Tectonics, 18-21 May 2015, Vitória, ES, Brazil.

Russo R.M., Speed R.C., 1994, Spectral analysis of gravity anomalies and the architecture of tectonic wedging, NE Venezuela and Trinidad, *Tectonics*, 13, 2: 613– 622.

Sclater J.G., Christie P.A.F., 1980, Continental stretching: An explanation of the post mid-Cretaceous subsidence of the central North Sea basin, *J. Geophys. Res*., 85, 3711 –3739.

Supko P.R., Perch-Nielsen K., Carlson R.L., 1997, General synthesis of central and south atlantic drilling results, LEG 39, Deep Sea Drilling Project, doi:10.2973/dsdp.proc.39.101.

Talwani M., Worzel J.L., Landisman M., 1959, Rapid gravity computations for two-dimensional bodies with application to the Mendocino submarine fracture zone: *J. Geophys. Res*., 64, 49-59.

Weidmann C., Spagnotto S., Giménez M., Martínez P., Álvarez O., Sánchez M., Klinger F.L., 2013, Crustal structure and tectonic setting of the south central Andes from gravimetric analysis, *Geofísica Internacional*, 52-3, 197-208

Zalán P.V., Severino M.C.G., Rigoti C.A., Magnaviva L.P., Oliveira J.A.B., Vianna A.R., 2011, An entirely new 3D-view of the crustal and mantle structure of a South Atlantic passive margin — Santos, Campos and Espírito Santo Basins, Brazil. In: AAPG Annual Convention, Houston TX, USA, *Extended Abstracts*, Search and Discovery, article #30177. World Wide Web Address: http://www.searchanddiscovery.com/pdfz/documents/2011/30177zalan/ndx_zalan.pdf.html

Geofísica Internacional (2016) 55-3: 215-225

Original paper

Shallow geoelectrical characterization of a small portion of the Basin of Mexico aquifer: Towards a better resource management

Claudia Arango-Galván*, Elsa Leticia Flores-Márquez, Antonio Hernández-Espriú, Alberto Arias-Paz and Edgar Jesús Sagahón-López

Received: October 31, 2015; accepted: March 11, 2016; published on line: July 01, 2016

DOI: 10.19155/rgi20165531613

Resumen

La escasez en el suministro de agua potable en las grandes ciudades es cada vez más común. La Ciudad de México es parte de este problema porque se han observado reducciones dramáticas en los niveles de agua subterránea en años recientes, junto con problemas asociados, tales como subsidencia y mala calidad del agua, poniendo en peligro el acceso a este recurso. El campus de Ciudad Universitaria está localizado en la parte sur de esta mega ciudad y cuenta con más de 150,000 usuarios, cuya demanda de agua limpia es satisfecha por tres pozos de extracción que suministran casi tres millones de metros cúbicos por año. Sin embargo, la configuración de esta parte del acuífero de la Cuenca de México no es bien conocida y ha mostrado una fuerte disminución del nivel freático. Así, se llevó a cabo un estudio integrado con el objetivo de caracterizar esta porción del acuífero para proporcionar información que permita una mejor evaluación de la situación actual y mejorar su gestión. A pesar de la dificultad de implementar una caracterización directa de las unidades hidrogeológicas que afloran en la zona, ya que casi todo el campus está cubierto con infraestructura (i.e. instalaciones académicas, caminos, jardines), se llevó a cabo un reconocimiento geológico en las inmediaciones de los pozos de explotación y se realizó una caracterización geofísica usando el método electromagnético en dominio de tiempo. Adicionalmente, se implementó una prueba de bombeo en el pozo principal de explotación con el fin de estimar las propiedades hidráulicas del acuífero. Así, la integración de estas técnicas permite inferir algunas cuestiones importantes relacionadas con el acuífero y su explotación en esta área.

Palabras clave: Cuenca de México, sobreexplotación, método electromagnético en el dominio del tiempo, gestión de recursos hídricos, seguridad del agua.

Abstract

Shortage in supply of fresh water in megacities is becoming increasingly common. Mexico City is part of this problem because dramatic reductions in groundwater levels have been observed in recent years along with associated problems such as subsidence and poor water quality, endangering access to this resource. The Ciudad Universitaria *campus* is located in the southern part of this mega city and has over 150,000 users, whose clean water demand is met from three abstraction wells supplying almost three million cubic meters per year. However, the configuration of this portion of the Mexico Basin aquifer is not well known and has shown a strong depletion in the water table. Thus, an integrated study was conducted with the aim to characterize this portion of the aquifer to provide information that allows carrying out a better assessment of its current situation and improving its management. Despite the difficulty to conduct a direct characterization of the hydrogeological units outcropping in the area since almost all the *campus* is covered with infrastructure (*i.e.* academic facilities, roads, gardens), a geological reconnaissance was carried out in the vicinity of exploitation wells and a geophysical characterization was performed using time-domain electromagnetics. Additio-nally, a pumping test was conducted in the main exploitation well in order to estimate hydraulic properties of the aquifer. Thus, the integration of these techniques allows inferring some important issues regarding the aquifer and its exploitation in this area.

Key words: Basin of Mexico, overexploitation, time domain electromagnetics, water resource management, water security.

C. Arango-Galván*
E.L. Flores-Márquez
Instituto de Geofísica
Universidad Nacional Autónoma de México
Ciudad Universitaria, Delegación Coyoacán, 04510
México, D.F. México
**Corresponding author: claudiar@geofisica.unam.mx*

A. Hernández-Espriú
A. Arias-Paz
Grupo de Hidrogeología
Facultad de Ingeniería
Universidad Nacional Autónoma de México
Ciudad Universitaria, Delegación Coyoacán, 04510
México, D.F. México

E.J. Sagahón-López
Facultad de Ingeniería
Benemérita Universidad Autónoma de Puebla
Blvd. Valsequillo y Av. San Claudio
Col. San Manuel, C.P. 72570
Puebla, Puebla.

Introduction

In the recent decades, both rapid population growth and industrial development have increased the demand of basic services such as drinking water supply. In contrast, water resources at the surface are decreasing gradually because of contamination, climatic changes and hazards. Moreover, the water resources for human consumption are continuously depleting and management of this essential resource has become a top priority in several parts of our world, particularly in semi-arid and arid regions. In addition, the vulnerability of groundwater resources to drought, over-extraction and quality deterioration must be assessed, and the natural functions of groundwater safeguarded.

According to Food and Agriculture Organization of the United Nations (FAO, 2015), the availability of water per capita per year in China decreased from 2317 m^3 in 1992 to 2005 m^3 in 2014, *i.e.* a loss of 13% in 22 years. In the same period, the water availability per habitant dropped by 28% (2115 m^3 to 1526 m^3) in India. In this global context, the larger cities of Mexico face similar water supply crisis.

Particularly, the aquifer system of Mexico City presents a water supply crisis. According to Leyva-Suárez (2010), the evolution of static levels measured from 1985 to 2003, show a strong dropping of the potentiometric surface, with the presence of a cone of depression of about 20 m, identified in a 6 km wide area located nearly center of the Mexico City (Figure 1).

According to the National Water Commission (CONAGUA, 2014), the water availability per person per year has decreased from 5812 m^3 in 1990 to 4573 m^3 in 2005. This value will continue to drop to 3430 m^3 by 2030. An important part of this water (~36%) is currently exploited from underground sources. Thus, the lack of planning in water withdrawal causes the problem of groundwater overdraft leading to increasing pumping and drawdown rates inversion of the vertical hydraulic gradient, land subsidence, water quality concerns and seawater intrusion into coastal environments among others. This means that the case of Mexico City is exceptionally critical since the availability decreased 27% from 1992 to 2014. In contrast, the decline in water level was no so notorious in other countries like Germany and Japan since both these countries have reduced

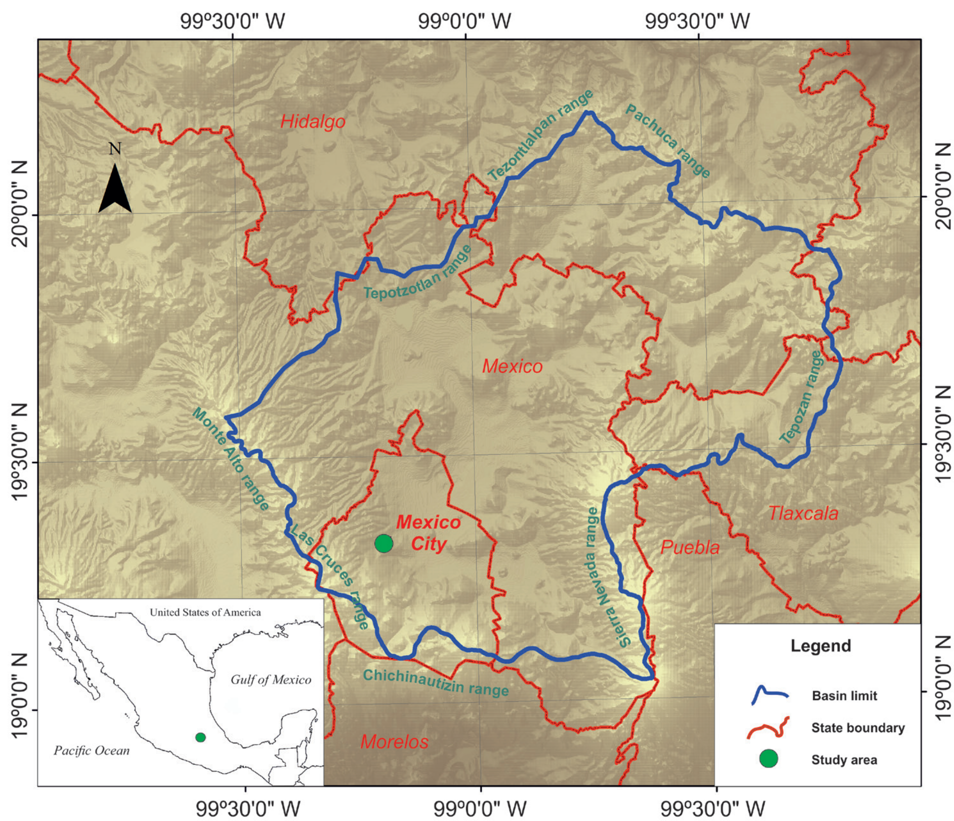

Figure 1. The Basin of Mexico. Survey area is shown as a green dot.

the availability of renewable water per capita per year by 1.3% and 3.1%, respectively in the same period (FAO, 2015).

Even if it is considered that the Basin of Mexico has a large water catchment, its inadequate management to over the centuries has limited the population to safeguard sustainable access to a good quality and quantity resource (United Nations, 2013).

This scenario has forced the authorities to search new sources of fresh water in deeper aquifers. The San Lorenzo Tezonco well, drilled in 2014, reached 2008 m depth and presently provides a flow up to 90 L/s to eastern zone of the City (Morales-Casique *et al*., 2014; Arce *et al*., 2015). However, the adverse water quality and increased costs to make it affordable to the population are some of the associated problems. With this discouraging background, increasing the knowledge of groundwater resources (new affordable sources and proper development management strategies) becomes a top priority in Mexico City.

The Ciudad Universitaria *campus* (CU) is located at the southern zone of Mexico City. It is the biggest *campus* of The National Autonomous University of Mexico (UNAM), one of the most important public universities in Mexico (Figure 2). This zone of the aquifer supplies drinking water to an approximate 150,000 population and there is no available information of the physical characteristics of this portion of the aquifer (González-Villarreal *et al*., 2008). In 2007, as a result of 4th World Water Forum held in Mexico, UNAM proposes the implementation of PUMAGUA, a program to management, use and recycling water resources within their university *campï*. This program has been basically focused in management of networks water distributions. However, the current state of groundwater at its principal *campus* has not been studied in detail. Thus, the present study is a first attempt to characterize the aquifer region at this *campus* zone.

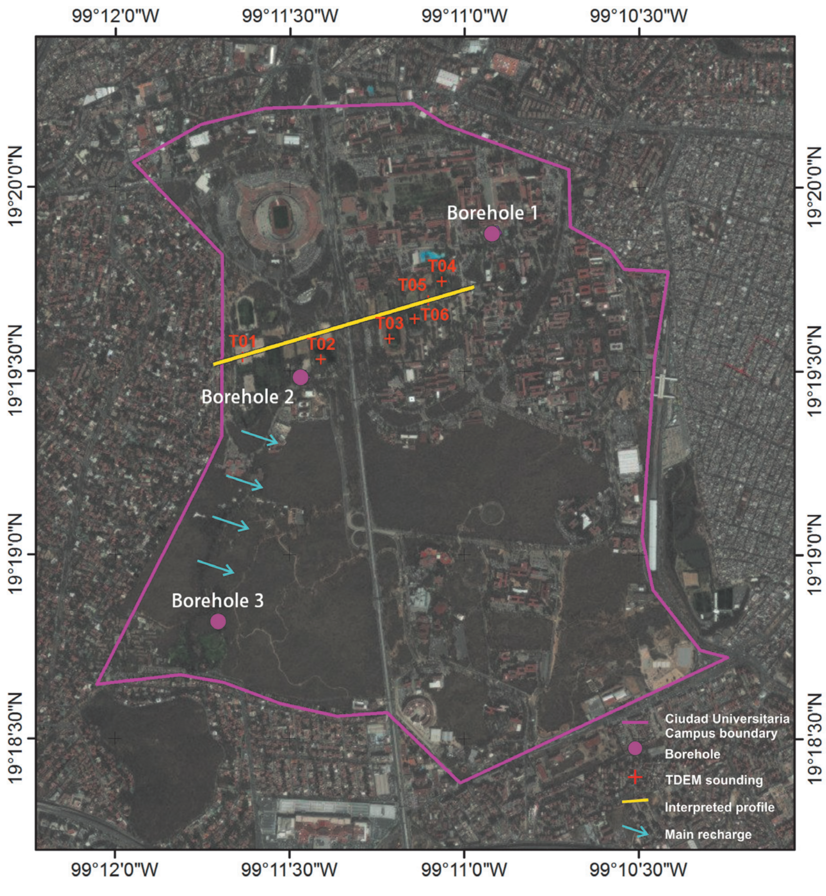

Figure 2. Location of the TDEM soundings within Ciudad Universitaria *campus*. Purple circles depict currently abstraction wells.

Three different wells located inside the *campus* extract about 100-170 L/s (Figure 2). Nevertheless, a gradual drop in the water table has led to reduce the total extraction to a third part of the usual withdrawal (Rocha-Guzman, 2010). The overdraft resulted in the increasing salinity that affects both water quality and integrity of distribution pipelines. It was difficult to conduct a direct characterization of the hydrogeological units outcropping in the area as almost all the *campus* is covered with infrastructure (*i.e.* academic facilities, roads, gardens). However, a geological reconnaissance was carried out surrounding the abstraction wells. The main characterization was performed using time-domain electromagnetics (TDEM). It is a suitable geophysical technique because it does not require very large areas for data acquisition. Additionally, a pumping test was conducted in the main abstraction well in order to assess the hydraulic properties of the aquifer. Therefore, the integration of these techniques will allow inferring some important issues regarding the aquifer and its exploitation scheme in this area, to characterize geological and geophysical the local aquifer system and to contribute to a sustainable management of the same.

Geological setting

Mexico City is located within the southwestern sector of the Basin of Mexico (BM), which in turn lies between the southern boundary of the south Mesa Central and the eastern part of the Trans-Mexican Volcanic Belt (Ferrari *et al*., 2012), During the early Tertiary period, intense volcanic activity gave way to the Chichinautzin volcanic field called Sierra del Chichinautzin. As a result, the basin's flow pattern changed from exorheic to endorheic. It is considered as a lake plateau at 2240 m.a.s.l. and surrounded by alluvial plains and up to 5000 m high volcanic structures (Figure 1). BM is limited in the south by a trending of monogenetic volcanoes (Chichinautzin range); is bounded in the northern portion by three different ranges (Pachuca, Tezontlapan and Guadalupe); is limited in the east by the Patlachique and the Sierra Nevada ranges, and is border in the west by Monte Alto and Las Cruces ranges (Valadez-Cabrera, 2009).

Regional stratigraphy

The volcanic rocks of Las Cruces and Monte Alto ranges were mainly described by Schlaepfer (1968). They are widely distributed in the southwestern boundary of the BM, where a range of three stratovolcanoes, along with pyroclastic deposits, is oriented NNW to SSE, and divide the basins of Mexico and Río Lerma. It is covers discordantly the Middle to Late Miocene extrusive rocks and Early Pliocene volcanic units; also it is covered by Quaternary alluvial and lacustrine deposits, as well as by lava and pyroclastic flows of the Chichinautzin volcanic range. The outcropping volcanic rocks consist of lavas, conglomerates, breccias, tuffs and pyroclastic products of andesitic, dacitic and andesitic-basaltic composition. These units are also covered or interbedded with alluvial material and fluvial palaeochannels (Vázquez-Sánchez and Jaimes-Palomera, 1989).

Local geology

Before Schlaepfer (1968) described Las Cruces Formation, Bryan (1948) defined a group of pyroclastic deposits from effusive volcanic sequences of Las Cruces volcanic range deposited in water as Tarango Formation; it is mainly composed by tuffs, volcanic breccias, conglomerates, volcanic gravels of fluvial origin and layers of pumice of Pliocene age. This formation shows a very scarce fracturing and different degrees of compaction. Overlying this formation, there is a Quaternary basaltic flow erupted from the southern flank of the Xitle volcano. This lava flow is called Ciudad Universitaria Unit and is covering part of the study area as pahoehoe and pillow lavas type with a maximum thickness of 30 m.

Hydrogeology of the Basin of Mexico

The hydrogeological setting of the study area is a very complex system composed by different geologic units, which have different hydraulic properties. The fresh water aquifer within the BM setting is made up of Quaternary alluvial deposits, volcaniclastic and pyroclastic rocks and Plio-Quaternary basaltic-andesitic rocks. Groundwater depth ranges between 60-170 m, while saturated thickness might exceed 800 m in some areas (Hernández-Espriú *et al*., 2014), however, extraction wells are screened within the uppermost 300-400 m of this unit (Herrera *et al*., 1989). That also coincides with the geophysical characterization carried out by Campos-Enríquez *et al*., (1997) situating the maximum depth at 530 m.

Related to the deep hydrostratigraphy, Pérez-Cruz (1988) integrated results from four deep boreholes drilled by PEMEX after the M 8.1 earthquake occurred in Mexico City in 1985. The results suggest the presence of four different geological units reported from deepest to shallowest as: 1) Limestone unit (probably part of the Morelos and/or Cuautla formation), 2) Lower volcanic unit, 3) Upper volcanic unit, and 4) Lacustrine deposits. Regarding the limestone aquifer, only two boreholes reached it at 1500 m and 2100 m depth. The other two wells did not reach it despite one of them was drilled until 3200 m.

According to previous studies (Mooser *et al*., 1996; Pérez-Cruz, 1988; Vázquez-Sánchez and Jaimes-Palomera, 1989) the hydrogeological setting can be summarized into the following major units: (1) a confining aquitard (Quaternary alluvial, fluvial and lacustrine low-permeability deposits), (2) an upper granular aquifer (Quaternary alluvial, volcaniclastic and Plio-Quaternary andesitic-basaltic deposits), (3) a lower fractured aquifer (Miocene andesitic rocks and Oligocene basaltic and rhyolitic deposits) and (4) the cretaceous basement (folded and fractured limestones, sandstones and shales).

Despite all this available information, the local configuration of the aquifer within Ciudad Universitaria *campus* is barely known. In this sense, the development of this work aims to get a better insight of the aquifer in order to provide useful information to improve its management.

Methodology

Geophysical prospecting

Regarding geophysical characterization of natural resources (*e.g*. aquifers, hydrocarbons, mining and geothermal sources), it is known they are genetically related to water. Here, the physical property of the subsurface materials most affected by the change in water content is the electrical conductivity, so that many of the potential exploitation zones can be located by measuring this property (Meju *et al*., 1999; Meju, 2002; Fontes *et al*., 1997).

In particular, we decided use the time domain electromagnetic method (TDEM) to characterize the shallower part of the upper CU aquifer. TDEM physical principle involves the induction of a primary magnetic field through a square coil, which is abruptly interrupted in order to produce eddy currents into the subsurface. These currents will generate a secondary magnetic field, which can be detected by an appropriate receiver coil on the surface (Nabighian and Macnae, 1991).

Thus, it is possible to characterize the electrical property of the subsoil by measuring the voltage registered by the receiver coil, which varies according to the behavior of the magnetic field decay. Thus, this time dependent function can be transformed in an apparent resistivity curve that is used to estimate the resistivity distribution using appropriate inversion techniques (Nabighian, 1979).

Given the required conditions to implement this methodology (*i.e.* electromagnetic noise-free zones, flat terrain, metal-free areas) and the intensive anthropogenic activity within the *campus*, we have proposed as acquisition areas those designated for sport fields because they fulfill the space and flatness requirements.

Data acquisition was performed in two stages; the first one consisted of four electromagnetic soundings using a single loop configuration of 50x50 m by side. This survey was done during November 2011. In the second stage, performed during February 2012, two additional electromagnetic soundings were acquired using the same configuration. All measurements were performed with the pumping system off, using the transient electromagnetic survey system terraTEM by MonexGeoscope. The transmitting current reached between 5 and 6 amperes. To increase the statistical quality of estimations, measurements were taken with gains of 1, 10, 100 and 1000 (Figure 2).

Local hydrogeological characterization

A short-term, constant-rate pumping test was performed to borehole 2, called Multifamiliar well (next to the prospected area) as a complimentary technique. This well is one of the three main suppliers of drinking water to Ciudad Universitaria *campus*. Pumping tests are a widespread method for assessing the hydrodynamic behavior of aquifers and/or the mechanical performance of abstraction wells (Fetter, 2001).

The static (no pumped) water table was initially measured at a depth of 72.16 m. Then we start the test at a constant flow rate of 90 L/s during 2.16 hours. When the steady dynamic level was reached (83.67 m) the submersible pump was shutdown and we registered the buildup period, during 1.5 hours. The measurements were taken manually with an electric sounding, following overall recommendations reported in Brassington (2006).

On one hand, a non-parametric approach of the test was carried out in order to identify possible flow regimes, evaluating the semi-log and log-log drawdown transient response. On the other hand, the parametric approach was computed using analytical solutions of the general flow equation. The best fit between measured and calculated drawdown was achieved using the Hantush and Jacob model (Hantush and Jacob, 1955; Hantush, 1964) that considers an exact solution for non-steady flow to a partially penetrating well in an anisotropic, infinite leaky aquifer.

Data processing and modeling

TDEM data

After editing and averaging the decay curves, final apparent resistivity *versus* time curves were obtained for each TDEM station. Thereby, we could apply Occam's inversion for generating smooth and simplified geoelectrical models (Constable *et al*., 1987). In order to obtain detailed information about the different hydrogeological layers, one profile in an approximate EW direction was interpreted (Figure 3).

Five different geoelectrical layers were inferred from geoelectrical section, which are described below and summarized in Table 1:

U1: This geoelectrical unit was only detected below sites T01, T05 and T04. This horizon the highest resistivities detected in the profile with values greater than 100 Ohm.m, and an average thickness of 20 m. Possibly related to Ciudad Universitaria Unit.

U2: This unit is underlying horizon U1, it has a variable thickness ranging from 12 to 45 m, with resistivities of 30 to 50 Ohm.m.

U3: This geoelectrical unit is showing a value resistivity between 25 to 32 Ohm.m, it has a variable thickness ranging from 23 to 74 m below site T03.

U4: It is the most conductive layer observed in the interpreted profile, showing resitivities lower than 10 Ohm.m. The top layer coincides with the reported water table depth so this horizon is related with the aquifer. It also shows internal variations reaching more conductive values beneath sites T01, T02, T06 and T05.

U5: At greater depths below 180 m, the unit U5 is observed having an average resistivity about 20 Ohm.m.

According to the stratigraphy reported in Pérez-Cruz (1988), the upper horizons inferred from borehole Copilco-1, the so-called Upper Volcanic Unit, are also correlated to our geoelectrical image. The shallower horizon described is a basaltic unit of 30 m thick coinciding with U1; underlying this horizon a

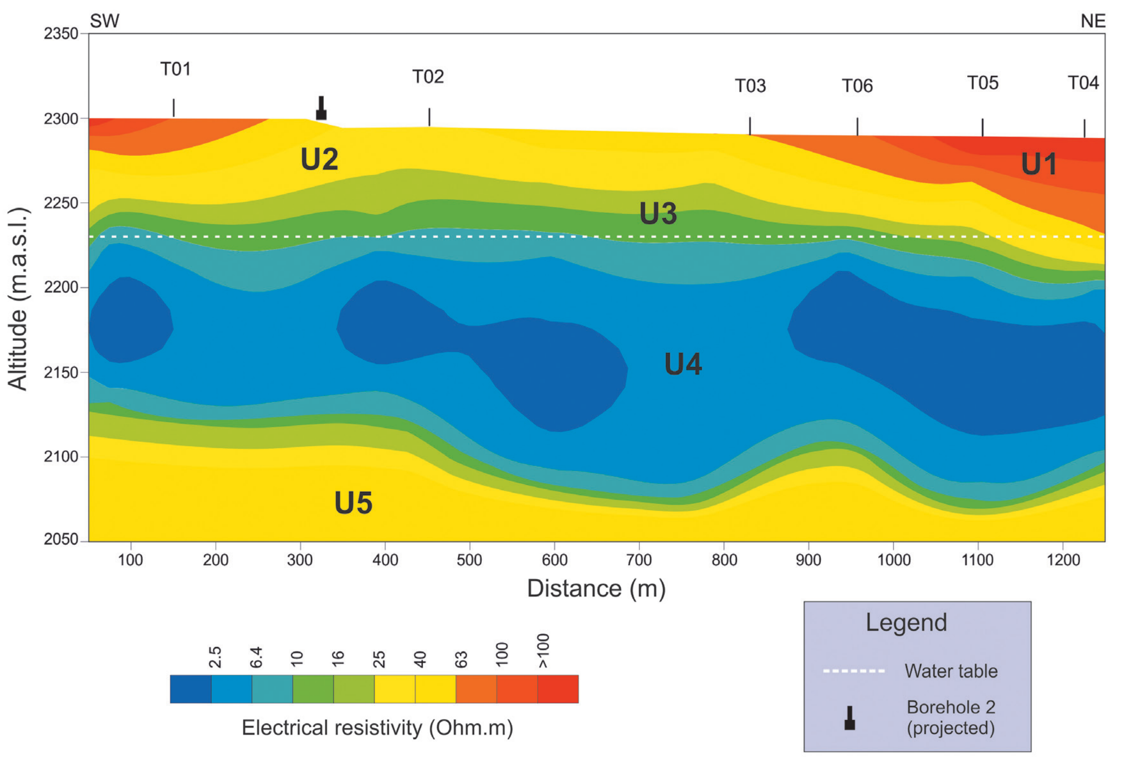

Figure 3. Geoelectrical model inverted from TDEM data.

Table 1. Geoelectrical units inferred from TDEM inversion.

		U1	U2	U3	U4		U5	rms
T01	ρ_a (Ohm.m)	102	50	32	11	1	25	0.501
	Thickness (m)	16	33	23	34	61	∞	
T02	ρ_a (Ohm.m)	-	35	18	4	2	20	0.287
	Thickness (m)	-	45	24	13	70	∞	
T03	ρ_a (Ohm.m)	-	46	26	11	2	18	0.151
	Thickness (m)	-	12	74	39	47	∞	
T06	ρ_a (Ohm.m)	-	13	30	6	1	15	0.410
	Thickness (m)	-	34	32	10	62	∞	
T05	ρ_a (Ohm.m)	103	45	29	4	1	15	0.270
	Thickness (m)	21	28	27	48	70	∞	
T04	ρ_a (Ohm.m)	94	50	33	8	1	17	0.314
	Thickness (m)	24	34	29	22	71	∞	

30 m breccia layer was observed, probably related to resistivity values observed in U2. Finally, this horizon is overlying a sequence of tuff and clayish tuff that reached 400 m depth, which could be correlated to units U3 to U5, depending on the water content, consolidation and clay content.

Pumping test data

Figure 4 shows the drawdown transient response during the pumping test. As noted in Figure 4a, the buildup period was measured up to quasi-static conditions, prior to pumping. In addition, the drawdown was drop in the order of ~ 6 m within the first 15 seconds of pumping, suggesting a well loss component, *i.e.* well skin or damage (not evaluated).

In addition, the early-time response seems to fit a straight line (Figure 4b), however, at late times (> 1000 sec), drawdown trend to stabilize. This effect suggests a constant head boundary or a leaky behavior. In order to verify this, we compare the field data with several transient models and the best fit was achieved using the Hantush and Jacob, leaky aquifer model (Hantush and Jacob, 1955; Hantush, 1964). The fitting process was optimized in both drawdown and buildup periods, based on a non-linear weighted least-squared parameter estimation, using the Gauss-Newton linearization method. With this procedure, the difference between observed and calculated drawdown (mean residual value, n = 34) is about 2.5 x 10^{-3} m. The final fit is presented in Figures 4b, c and d.

For comparison purposes, we are showing two fits: the Hantush and Jacob model and the classic Theis model (Theis, 1935) for an infinite, confined and isotropic model. As shown, the field test has a leaky aquifer behavior. Therefore, one or more low-permeability thin layers (*e.g.* heterogeneities within the Tarango Formation, associated to lacustrine or fine-grained sediments) located above the abstraction aquifer can be inferred from the dynamic behavior of the test, even when the geophysical prospection is not detecting this changes, due to the vertical resolution of the technique.

From the parametric approach, the leaky aquifer model allowed us to estimate the following parameters: aquifer transmissivity (T) of 480 m^2/d, storage coefficient (S) of 1.3 x 10^{-3} and vertical hydraulic conductivity of the leaky layer, k', in the order of ~ 0.08, 0.4 or 0.8 m/d (rough estimation), considering hypothetical aquitard thicknesses of 1, 5 or 10 m, respectively. Note that the T estimates derive from the buildup period (Figure 4d) using the Cooper and Jacob straight line (Horner time) was computed in the order of 530 m^2/d.

As far as we know, these are the first reported hydraulic parameters within the Ciudad Universitaria *campus* that can be used to improve groundwater management strategies in this small portion of the drinking water aquifer.

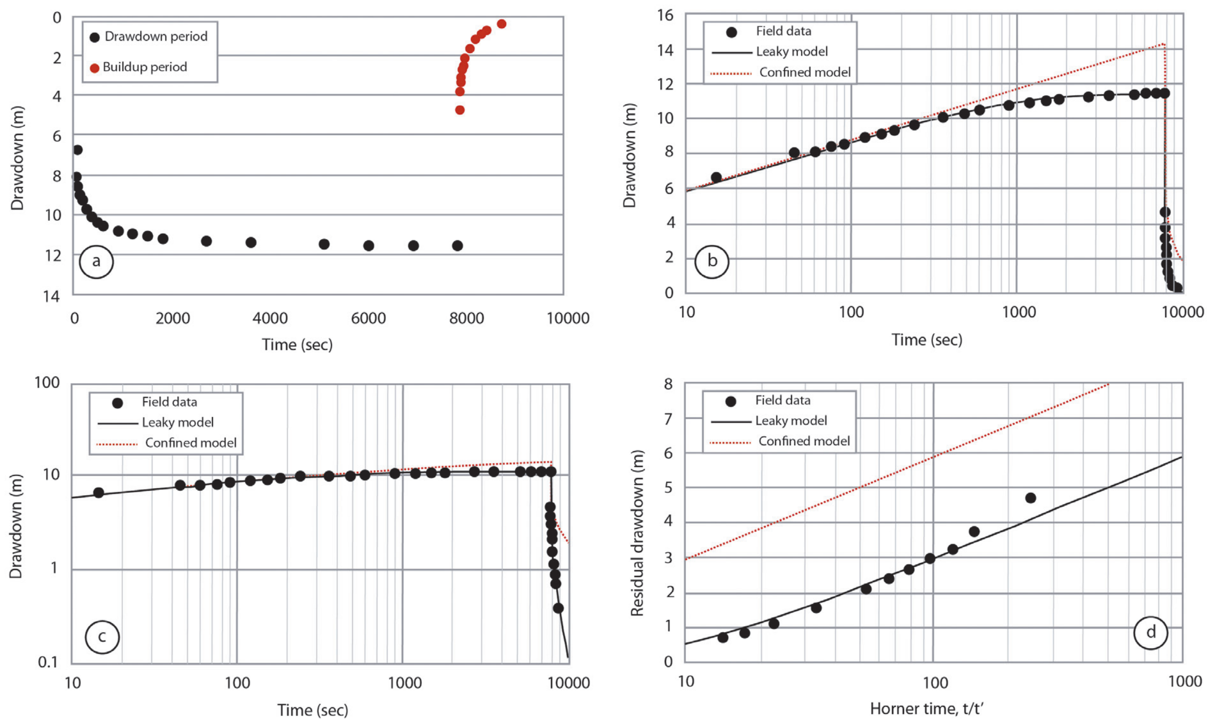

Figure 4. Drawdown transient response of the Borehole 2 (Multifamiliar) groundwater abstraction well within Ciudad Universitaria *campus*. (a) Drawdown and buildup periods. (b) Semi-log transient response. (c) Log-log transient response. (d) Semi-log analysis for the buildup period using Horner time. In b, c and d the continuous blue line represent the Hantush and Jacob (leaky) aquifer model and dotted red line the Theis (confined) aquifer model.

Aquifer characterization

Recently, Solano-Rojas *et al*. (2015) have establish the relationship between land subsidence and decreasing in groundwater levels in the Mexico City Metropolitan Area (MCMA). Their results suggest that the aquifer system is under severe stress due to the extreme groundwater extraction that far exceeds the magnitude of natural recharge. According with this study, Ciudad Universitaria *campus* is located within a region where the land subsidence is ranging from 5 to 26 mm/yr; which placed it in a zone with the lowest subsidence rates in the MCMA. Moreover, one of the natural recharge areas for the Basin of Mexico aquifer is located near of the study zone, which in theory helps to water table to be less affected by intensive extraction.

Within Ciudad Universitaria *campus* the water demand is supplied by three wells (Table 2), one of them exploited since early fifties, borehole 1. The *campus* is affected by the same problems as the aquifer of BM, *i.e.* increasing population and increasing demand of drinking water, so the extraction regimes in wells have also increased. Analyzing the water levels evolution during last ten years (Figure 5), we can establish that borehole 2 present the worst drawdown in two years, reaching a decrease of 2 m per year, while borehole 3 has a better performance to the extraction, which has declined 0.80 m per year. A linear fitting was performed to the measured levels for the three boreholes (Figure 5) showing a drawdown trending that evolves from 0.6 to 1.5 m per year, for boreholes 3 and 1, respectively.

We have also analyzed two hydraulic gradients, one from borehole 1 to borehole 2 and the other one between boreholes 2 and 3. They show changes along time, *i.e.* about zero between boreholes 2 and 3, because the alignment between them is almost perpendicular to groundwater recharge. The obtained gradient ranges from -6.72×10^{-6}, before 2009, to 7.23×10^{-5} from 2010 to nowadays. This change in the hydraulic gradient could be related to the fact that borehole 2 present the worst drawdown in recent years. The hydraulic gradient between boreholes 1 and 2 remained about 0.0259 for more than 10 years, but in 2015 reached 0.0931; this means

Table 2. Boreholes in CU campus providing fresh water for 150,000 users.

Borehole Number	Borehole Name	Topographic level (m)	Total depth (m)	Groundwater withdrawal (L/s)	Drop/year (m)
1	Química	2279	132	125	1.05
2	Multifamiliar	2312	157	250	1.80
3	Vivero Alto	2335	193	250	0.80

that the aquifer is suffering more stress than before and overexploitation, moreover taking into account the alignment between boreholes 1 and 2 that is tangential to the direction of the groundwater recharge, so we could infer the potentiometric surface of the aquifer is tilting to the southeast.

Conclusions

This study characterizes electrical resistivity distribution in order to get a better insight of the hydrogeoelogical configuration of a small portion of the Mexico Basin aquifer within the Ciudad Universitaria *campus*. TDEM provided accurate information about the distribution of electrical resistivities in the subsurface and allow us to establish a complete hydrogeological assessment. The geoelectrical section coincides with the already reported stratigraphy of the so-called Upper Volcanic Unit (Pérez-Cruz, 1988). The shallower layer U1 corresponds to basaltic Ciudad Universitaria Unit, which shows the highest resistivity values.

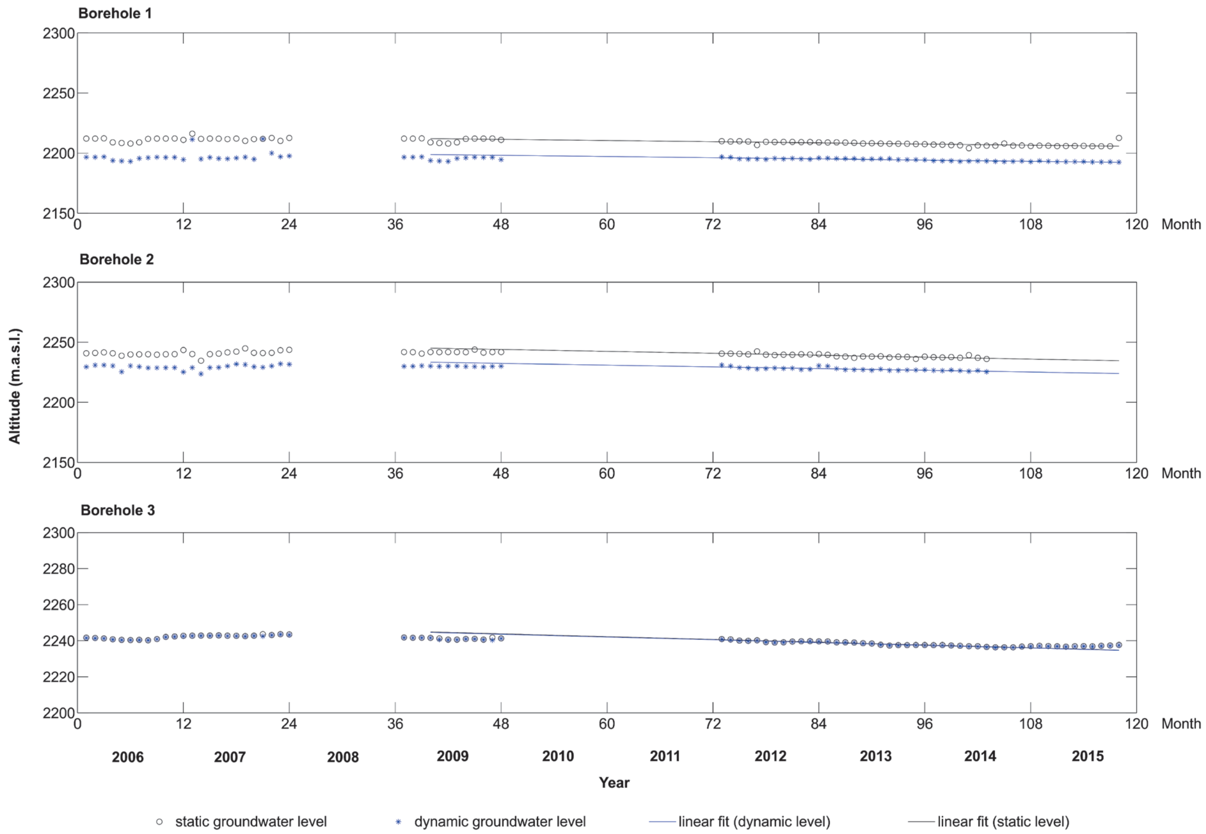

Figure 5. Evolution of the water table from 2009 to 2015 for all abstraction wells inside Ciudad Universitaria *campus*.

Underlying this horizon we observed a layer with resistivity values about 30-50 Ohm.m that could be related to a volcanic breccia. The water table depth coincides with the presence of a conductive layer of more than 150 m thick and resistivity values below 10 Ohm.m. Finally, underlying the conductive horizon the resistivity values increase until reach a mean value of 20 Ohm.m.

If an increment on water supply is needed in the future, the geoelectrical horizon with the greatest potential for extraction is layer U4, and the water table is expected to be at 70 m depth.

Regarding aquifer characterization, the estimated drawdown for the potentiometric surface in ten years is almost of 8 m in the area of the *campus*. The prediction, by linear fitting, for the dropdown of water level for the three boreholes by assuming the current extraction rate for the next year is of at least 1.5 m below the current level.

The computed hydraulic gradients, between wells 1 and 2 has remained about 0.0259 for more than 10 years, but in 2015, this value reached 0.0931, denoting excessive stress on the aquifer; and between wells 2 and 3, this value fluctuates from -6.72×10^{-6}, before 2009, to 7.23×10^{-5} nowadays. Thus, this change is probably related to the stress suffered by the entire BM aquifer system.

Finally, this study of a small portion of the BM aquifer can be used as a pilot model to implement improvements in the management of the entire system since this studied area could be considered as a closed hydraulic system due to the constrained interaction with the rest of the aquifer system.

Acknowledgments

Authors thank DGOyC staff, particularly Gabriel Martínez, for their assistance during the compilation of information. We also thank José Luis Salas and Ulises Valencia for their help in collecting, reviewing, and processing data. Thanks also to the reviewers for their helpful comments to improve the manuscript. This study was supported by Project DGAPA-PAPIIT IA-100812-2 “Caracterización geofísica de una porción del acuífero de la Cuenca de México en la zona de Ciudad Universitaria”.

References

Arce J.L., Layer P., Martínez I., Salinas J.I., Macías-Romo M.C., Morales-Casique E., Benowitz J., Escolero O., Lenhardt N., 2015, Geología y estratigrafía del pozo profundo San Lorenzo Tezonco y de sus alrededores, sur de la Cuenca de México. *Boletín de la Sociedad Geológica Mexicana*, 67, 2, 123-143.

Brassington R., 2006, Field Hydrogeology. The Geological field guide series. 3rd. ed. John Wiley & Sons. London, 255 p.

Bryan K., 1948, Los Suelos Complejos y Fósiles de la Altiplanicie de México en Relación con los Cambios Climáticos. *Boletín de la Sociedad Geológica Mexicana*, XIII, 1-20.

Campos-Enríquez J.O., Flores-Márquez E.L., Chávez-Segura R., 1997, Geophysical characterization of hydrogeologic systems, *The Leading Edge*, 16, 12, 1769-1773.

Carrera-Hernández J.J., Gaskin S.J., 2007, The Basin of Mexico aquifer system: regional groundwater level dynamics and database development. *Hydrogeology Journal*, 15, 1577-1590.

Constable C.S., Parker L.R., Constable G.C., 1987, Occam´s inversion: A practical algorithm for generating smooth models from electromagnetic sounding data. *Geophysics*, 52, 3, 289-300.

CONAGUA, 2014, Atlas del Agua en México. Comisión Nacional del Agua. Ciudad de México, México. 141 pp.

FAO, 2015, AQUASTAT website. Food and Agriculture Organization of the United Nations (FAO). Website accessed on 2015/07/22.

Fetter, C W., 2001, Applied Hydrogeology. 4th ed. Prentice Hall. New York, 605 p.

Ferrari L., Orozco-Esquivel T., Manea V., Manea M., 2012, The dynamic history of the Trans-Mexican Volcanic Belt and the Mexico subduction zone. *Tectonophysics* 522-523:122–149. doi: 10.1016/j.tecto.2011.09.018.

Fontes S.L., Meju M.A., Lima J.P.R., Carvalho R.M., La Terra E.F., Germano C.R., Metelo M., 1997, Geophysical investigation of major structural controls on groundwater distribution, north of São Raimundo Nonato, Piaui State. 5th Internat. Congr. Brazil. Geophys. Soc., Expanded Abstracts, 766-769.

González-Villareal F.J., Val-Segura R., Rocha-Guzmán J.D., 2008, Diagnóstico del Sistema de Agua Potable de Ciudad Universitaria de la Universidad Nacional Autónoma de México. XX Congreso Nacional de Hidráulica. Toluca, Estado de México, México. 15-18 de octubre.

Hantush M.S., Jacob C.E., 1955, Non-steady radial flow in an infinite leaky aquifer. *Transactions of the American geophysical Union*, 36:95-100.

Hantush M.S., 1964, Hydraulics of wells. In: Chow, E. (ed), Advances in Hydroscience. Academic Press, New York, 281-442 p.

Hernández-Espriú A., Reyna-Gutiérrez J.A., Sánchez-León E., Cabral-Cano E., Carrera-Hernández J., Martínez-Santos P., Macías-Medrano S., Falorni G., Colombo C., 2014, The DRASTIC-Sg model: an extension to the DRASTIC approach for mapping groundwater vulnerability in aquifers subject to differential land subsidence, with application to Mexico City. *Hydrogeology Journal*, 22:1469-1485. doi: 10.1007/s10040-014-1130-4.

Herrera I., Martínez R., Hernández G., 1989, Contribución para la administración científica del agua subterránea de la Cuenca de México. *Geofísica Internacional*, 28, 2, 297-334.

Herrera-Revilla I., Cortés-Silva A., 1989, El sistema acuífero de la cuenca de México. *Ingeniería Hidráulica en México*, 28, 2, 60-66.

Meju M.A., 2002, Geoelectromagnetic Exploration For Natural Resources: Models, Case Studies And Challenges. *Surveys in Geophysics*, 23, 2, 133-206.

Meju M.A., Fontes S.L., Oliveira M.F.B., Lima J.P.R., Ulugergerli E.U., Carrasquilla A.A., 1999, Regional aquifer mapping using combined VES-TEM-AMT/EMAP methods in the semiarid eastern margin of Parnaiba, Brazil. *Geophysics*, 64, 337-356.

Mooser R., Montiel A., Zúñiga A., 1996, Nuevo mapa geológico de las cuencas de México, Toluca y Puebla. Estratigrafía tectónica regional y aspectos geotérmicos [New gelogical map for the Basins of Mexico, Toluca and Puebla]. Comisión Federal de Electricidad, Mexico.

Morales-Casique E., Escolero O.A., Arce J.L., 2014, Resultados del pozo San Lorenzo Tezonco y sus implicaciones en el entendimiento de la hidrogeología regional de la cuenca de México. *Revista Mexicana de Ciencias Geológicas*, 31, 1, 64-75.

Nabighian M.N., 1979, Quasi-static transient response of a conducting half-space – An approximate representation. *Geophysics*, 44, 10, 1700-1705.

Nabighian M.N., Macnae J.C., 1991, Time Domain Electromagnetic Prospecting Methods. In: Nabighian, M.N. (ed), Electromagnetic Methods in Applied Geophysics - Application, Part A, Vol. 2. Society of Exploration Geophysicists. Tulsa, Oklahoma. 427-479 p.

Ortega G.A., Farvolden R.N., 1989, Computational analysis of regional groundwater flow and boundary conditions in the Basin of Mexico. *Journal of Hydrology*, 110, 271-294.

Pérez-Cruz G.A., 1988, Estudio sismológico de reflexión del Subsuelo de la Ciudad de México. Tesis de maestría. Universidad Nacional Autónoma de México. Ciudad de México, México. 83 p.

Rocha-Guzmán J.D., 2010, Diagnóstico y Sectorización del Sistema de Agua Potable de Ciudad Universitaria de la UNAM. Tesis de Licenciatura. Universidad Nacional Autónoma de México. Ciudad de México, México. 194 p.

Schlaepfer J.C., 1968, Resumen de la Geología de la Hoja de México, Distrito Federal, Estados de México y Morelos. Hoja 14Q - H(5), escala 1:100 000. Instituto de Geología, UNAM. Ciudad de México, México.

Theis C.V., 1935, The relation between the lowering of the Piezometric surface and the rate and duration of discharge of a well using ground-water storage. Trans. Am. Geophys. Union 16:519. doi: 10.1029/TR016i002p00519.

United Nations, 2013, Water Analytical Brief on Water Security and the Global Water Agenda. http://www.unwater.org/topics/water-security/en. Access date: October 15, 2015.

Valadez-Cabrera S.N., 2009, Procesos Magmáticos en el estratovolcán Tláloc, Sierra Nevada: Evidencias geoquímicas e isotópicas en xenolitos. Tesis de Licenciatura. Instituto Politécnico Nacional. Ciudad de México, México. 100 p.

Vázquez-Sánchez E., Jaimes-Palomera R., 1989, Geología de la Cuenca de México. *Geofísica Internacional*, 28, 2, 133-190.